TECHNISCHE UNIVERSITÄT MÜNCHEN
Lehrstuhl für Physik funktionaler Schichtsysteme, E10

Spin Waves in Nanochannels, Created by Individual and Periodic Bi-component Ferromagnetic Devices

Georg Friedrich Dürr

Vollständiger Abdruck der von der Fakultät für Physik der Technischen Universität München zur Erlangung des akademischen Grades eines

Doktors der Naturwissenschaften

genehmigten Dissertation.

Vorsitzender: Univ.-Prof. Dr. M. Zacharias
Prüfer der Dissertation:
1. Univ.-Prof. Dr. D. Grundler
2. Univ.-Prof. Dr. A. Holleitner

Die Dissertation wurde am 27. 9. 2012 bei der Technischen Universität München eingereicht und durch die Fakultät für Physik am 16. 10. 2012 angenommen.

Abstract

Spin waves (SWs) in ferromagnetic nanowires and perdiodically nanostructured bi-component devices have been studied experimentally and theoretically. The samples were structured from approximately 25 nm thick NiFe films by electron beam lithography. GHz SW spectroscopy has been performed with micro and nanostructured wave guides, in order to measure SW propagation. In 360 nm wide nanowires extraordinarily fast SW propagation has been measured in a zigzag magnetization configuration. Bi-component structures consisted of a NiFe matrix with a quadratic lattice of Co disks of 1 m and 600 nm period. In these structures an artificially created band structure with band gaps has been found. In collaboration with a theory group it was proven, that here band gaps are created by Bragg reflection and magnetic contrast of the materials.

Es wurden Spinwellen in ferromagnetischen Nanodrähten sowie periodisch nanostrukturierten Zwei-Komponenten-Strukturen experimentell und theoretisch untersucht. Die Proben wurden mittels Elektronenstrahllithographie aus ca. 25 nm dünnen NiFe-Filmen erzeugt. GHz-Spinwellen-Spektroskopie mit mikro- und nanostrukturierten Wellenleitern wurde durchgeführt, um die Ausbreitung von Spinwellen zu messen. In 360 nm breiten Nanodrähten wurde in einer Zickzack-Magnetisierungs-Konfiguration aussergewöhnlich schnelle Spinwellen-Propagation in einem nanostrukturierten Material gemessen. Zwei-Komponenten-Stukturen bestanden aus einer NiFe-Matrix mit einem quadratischen Gitter aus Co-Scheiben mit 1 μm und 600 nm Periode. In diesen Strukturen wurde eine künstlich erzeugte Bandstruktur mit Bandlücken gefunden. In Zusammenarbeit mit einer Theoriegruppe wurde nachgewiesen, dass hier die Bandlücken durch Bragg-Reflexion und den magnetischen Kontrast der Materialien entstehen.

Contents

Scientific Collaboration

Parts of this thesis have benefited from scientific collaboration. The following parts have been contributed by the respective researchers:

- Plane wave method calculations have been performed by Dr. J. Kłos and Dr. M. Krawczyk at Adam Mickiewicz University in Poznań, Poland. They provided band structures and spin-precessional mode profiles, at, in particular, finite wave vectors.
- Brillouin light scattering (BLS) and micro-focused BLS measurements have been performed by Dr. S. Tacchi, Dr. M. Madami and Dr. G. Gubbiotti at CNISM, Unità di Perugia - Dipartimento di Fisica in Perugia, Italy.
- Magnetic X-ray transmission microscopy (MTXM) measurements have been performed in collaboration with Dr. P. Fischer and Dr. M.Y. Im at the XM-1 at Beamline 6.1.2 of the Advanced Light Source (ALS) at the Lawrence Berkeley National Laboratory in Berkeley, CA, USA.

The author would like to express his gratitude for the very fruitful collaboration and hospitality in Poznań, Perugia and Berkeley.

1 Introduction

Magnonics is an emerging field of research that is concerned with the creation, control and detection of magnons, the quasiparticles of wave-like spin excitations, i.e. spin waves [Blo30, Kru10, Kru06, Neu09, Len11]. While the wave-like character of spin excitations can be compared to e.g. sound and light waves, spin waves exhibit peculiar characteristics as e.g. a strongly anisotropic dispersion relation [Kal86] governed by dipole-dipole interaction of spins for large wavelengths and exchange interaction for short wavelengths. Bose-Einstein condensates of magnons at room temperature have been shown to exist in minima of the dispersion relation [Dem06]. Recent interest has been fueled by the increasing possibilities of nanostructuring magnetic thin films and availability of high-frequency measurement electronics allowing access to GHz frequency and nanometer wavelength spin waves. Numerous applications of spin waves for micro- and nanoscale logic devices integrating microwave electronics have been proposed [Khi08a, Khi10, Khi08b, Khi07, Khi02, Cho06, Lee08]. These devices mostly rely on interference of spin waves. It has been shown that spin waves can propagate in structured and unstructured thin magnetic films by several 10 μm using all-electrical induction and detection of spin waves [Cov02, Bai01, Liu07, Vla08, Vla10, Neu11a, Neu10].

Nanowires

Several recent studies have proposed magnetic micro- and nanowires for waveguides of spin waves [Bai01, Bai03, Her04, Bay04, Cho07, Kos07, Dem08, Vla08, Boo09, Vog09, Koz09, Roy10, Pir11, LB11, Ngu11], suggesting micro- or nanoscale waveguides for GHz signals , directly coupled to electric circuits [Dem10, Mad11]. In previous publications, propagation in center and edge modes in such wires has been studied. [Bay04, Dem08]. In these wires, a finite amplitude at the wires' edges is found [Gus02] so that unwanted scattering of magnons may take place due to always present

imperfections, such as edge roughness, in real samples. Measured attenuation lengths have been smaller than in unstructured plain films made of the same materials [Dem08]. In photonic waveguides such as graded index fibers, modes are squeezed into the center of the waveguide, away from edges, so that edge effects do not influence the mode, resulting in a decreased attenuation of the popagating wave. This cladding-method has significantly advanced optical information transport [Kao09]. In this thesis we report on spin waves traveling through 360 nm-wide Py nanowires where we created the previously reported zig-zag magnetic state first reported by Topp et al. [Top08]. We find increased transmission in these samples. Using micromagnetic simulations, we state that spin waves propagate in two narrow channels squeezed into the interior of the nanowires, away from the edges. Furthermore, as was already demonstrated for electrons [Sak82], we find that by varying external parameters, here the external field H, we can modulate the group velocity of propagating spin waves v_g and thus create a velocity modulation transistor (VMT).

Bi-component lattices

Magnetic devices consisting of periodically patterned ferromagnetic material have also found considerable interest [Vys05, Yu04, Neu08, Neu08, Neu10, Tac12a, Ulr10, Tac10b, Tac10a]. Magnonic crystal behavior, where allowed bands and forbidden band gaps for spin-wave excitations arise [Vas96], and metamaterial behavior, where the material acts as an effective medium has been found [Neu11b, Neu11a, Neu11c, Ziv12]. This is similar to photonic crystals [Joa97], where such bands and metamaterial behavior is found for light. In one dimension, magnonic crystals have been demonstrated, consisting of the alternation of different magnetic materials [Wan10, Zha11], in two dimensions such bi-component lattices have only been studied using theoretical studies [Kra08, Ma11]. In this thesis we have performed a study of bi-component systems which are periodically nanopatterned in two lateral directions. We have found that these structures offer spatial control over spin-wave propagation beyond previous two-dimensional and one-dimensional nanostructures. We have further found a magnonic band gap in these structures.

Overview of the thesis

This work is organized as follows: In Chapter 2 we introduce the relevant theory on ferromagnetism, spin waves and spin-wave propagation, including numerical methods. In Chapter 3 we report on the used experimental techniques, all-electrical spin wave spectroscopy, where we evaluate exemplary data, Brillouin light scattering, and magnetic X-ray transmission microscopy. In Chapter 4 we show the preparation process used for samples studied in this work. In Chapter 5 we report on our study on nanowires. In Chapter 6 we report on our study on bi-component two-dimensional lattices, including a study of static magnetism, spin-wave localization and magnonic crystal behavior. We close with a summary and outlook in Chapter 7.

2 Theory

In this chapter we present basics of ferromagnetism, in order to introduce the subject and provide the necessary framework for the experiments performed in this thesis. We motivate the microscopic origin of ferromagnetism and relevant contributions to the internal field. Furthermore spin precession and resulting spin waves in ferromagnetic materials are introduced, presenting dispersion relations for spin waves used in this thesis. Finally we give an overview of numerical methods used to model experimental data. Comprehensive reviews on the subjects shortly addressed here can be found in [Blu01, Gur96, Sko08, Kit68, Hil02]. We follow these references in the following sections.

2.1 Ferromagnetism

Materials can be classified by the characteristic response of their magnetization $\mathbf{M}$ to an external field $\mathbf{H}$:

$$\mathbf{M} = \hat{\chi}\mathbf{H} \tag{2.1}$$

where $\hat{\chi}$ is the magnetic susceptibility and $\mathbf{M}$ is the volume density of microscopic magnetic moments $\mathbf{m}$ [Sko08]:

$$\mathbf{M} = \frac{\mathrm{d}\mathbf{m}}{\mathrm{d}V}. \tag{2.2}$$

$\hat{\chi}$ is a tensor, $\mathbf{M}$ and $\mathbf{H}$ need not be collinear. For diamagnetic materials, χ simplified to a scalar is $\chi < 0$. Here the induced $\mathbf{M}$ is antiparallel to and thus counteracting $\mathbf{H}$ due to orbital magnetic moments of electrons. For paramagnetic materials $\chi > 0$ holds true; uncompensated spins of electrons in the material align parallel to $\mathbf{H}$ and sum up to a net magnetic moment $\mathbf{M}$. In this work we study ferromagnetic materials, where $\chi >> 0$ in a linear approximation and $\mathbf{M}$ depends on the history of $\mathbf{H}$. Further-

more in a ferromagnet a spontaneous magnetization $\mathbf{M}$ can exist even in the absence of an external magnetic field $\mathbf{H}$. Ferromagnetism cannot be explained classically in quantitative terms, but only in a quantum mechanical framework. Furthermore the ferrimagnetic case, where two lattices of of magnetic moments exist, and the antiferromagnetic case, where both lattices are antiparallel and of equal magnetization, are found.

The underlying mechanism leading to the spontaneous magnetization of ferromagnets is exchange interaction between electrons in the material. The Pauli principle forbids two electrons of identical quantum numbers to occupy the same spatial wave function. Electrons with parallel spin alignment may not occupy the same space and are thus further apart, reducing Coulomb repulsion. This may reduce the total energy of the electron system. The Hamiltonian for exchange interaction is summing up interactions between all spins $\hat{\mathbf{S}}$ for localized, individual magnetic moments:

$$\mathcal{H} = -\sum_{i,j} J_{ij} \hat{\mathbf{S}}_i \cdot \hat{\mathbf{S}}_j, \tag{2.3}$$

with the parameter J_{ij} that quantifies the strength of interaction between spins. In the Stoner model [Blu01] ferromagnetic ordering of itinerant ferromagnets is discussed, where exchange interaction of itinerant electrons causes ferromagnetism. Ferromagnetic ordering is favored when the density of states at the Fermi energy $D(E_\mathrm{F})$ is high enough so that the reduction in Coulomb energy overcompensates the increase in kinetic Energy. This is the case for

$$\mu_0 \mu_\mathrm{B}^2 \lambda_\mathrm{S} D(E_\mathrm{F}) \geq 1, \tag{2.4}$$

where λ_S is a parameter for the average exchange field, μ_0 is the vacuum permittivity and $\mu_\mathrm{B} = \frac{e\hbar}{2m_e}$ is the Bohr magneton, the magnetic moment of an electron. In the materials treated in this thesis, Fe, Co, and Ni, λ_S is such that Eq. 2.4 holds true. Here 3d electrons contribute to ferromagnetism. We elaborate Eq. 2.3, formulating the Exchange energy E_exch with spin vectors in the place of quantum mechanical operators as

$$E_\mathrm{exch} = -J \sum_{i,j} \mathbf{S}_i \cdot \mathbf{S}_j = -2S^2 J \sum_{i,j} (1 - \frac{1}{2S^2} |\mathbf{S}_i - \mathbf{S}_j|^2), \tag{2.5}$$

using $|\mathbf{S}_i - \mathbf{S}_j|^2 = 2S^2(1 - \cos\angle(\mathbf{S}_i, \mathbf{S}_j))$ to solve the scalar product and assuming $J_{ij} = J$. We now substitute the spins by the magnetization $\mathbf{M}$ introduced in Eq. 2.2 as the volume density of magnetic moments. Due to the exchange interaction being nearly a next-neighbor interaction, the magnetization varies only over longer distances, allowing the term $1 - \frac{1}{2S^2}|\mathbf{S}_i - \mathbf{S}_j|^2$ to be treated in a Taylor series to the first order. Further we neglect constant contributions to the energy. We reach

$$E_{\text{exch}} = JS^2 \sum_i \sum_{\mathbf{r}_{ij}} \frac{1}{M^2} |(\mathbf{r}_{ij} \cdot \nabla)\mathbf{M}(\mathbf{r}_{ij})|^2. \tag{2.6}$$

We solve the sums over all spins in the crystal and between next neighbors to a constant factor A, the exchange constant, depending on the crystal lattice:

$$E_{\text{exch}} = \int \mathrm{d}\mathbf{r} \frac{A}{M^2} (\nabla \cdot \mathbf{M})^2. \tag{2.7}$$

As $\mathbf{H} = -\frac{1}{\mu_0} \frac{\partial F}{\partial \mathbf{M}}$, where F is the free energy, we find

$$\mathbf{H}_{\text{exch}} = \frac{2A}{\mu_0 M^2} \nabla^2 \mathbf{M}. \tag{2.8}$$

A further important energy contribution in ferromagnetic materials is the demagnetization energy E_{dem} and the corresponding demagnetization field $\mathbf{H}_{\text{dem}}$. It stems from the long-reaching dipole-dipole interaction between spins, favoring antiparallel alignment, in contrast to exchange interaction. The energy contribution is

$$E_{\text{dem}} = -\frac{1}{2} M_{\text{sat}}^2 \int \mathbf{M}(\mathbf{r}) \mathbf{H}_{\text{dem}}(\mathbf{r}), \tag{2.9}$$

where M_{sat} is the saturation magnetization. In order to derive $\mathbf{H}_{\text{dem}}$, we start with magnetostatic Maxwell equations:

$$\mu_0 \nabla \cdot (\mathbf{M} + \mathbf{H}_{\text{dem}}) = 0 \tag{2.10}$$

$$\nabla \times \mathbf{H}_{\text{dem}} = 0. \tag{2.11}$$

Introducing the concept of magnetic pseudo-charges ρ, or uncompensated dipoles at the sample's surface, analogous to electrostatics we can write

$$\mathbf{H}_{\mathrm{dem}} = -\nabla\Phi_{\mathrm{dem}}, \tag{2.12}$$

with the introduced scalar field Φ_{dem} fulfilling the Poisson equation

$$\Delta\Phi_{\mathrm{dem}} = -\rho, \tag{2.13}$$

that can be solved with Green's function known from electrostatics. This leads for a ferromagnet with uniform magnetization $\mathbf{M}$ to

$$\mathbf{H}_{\mathrm{dem}}(\mathbf{r}) = -\frac{\mathbf{M}}{4\pi}\int \mathrm{d}S\nabla_{\mathbf{r}'}\frac{\mathbf{n}}{|\mathbf{r}-\mathbf{r}'|}, \tag{2.14}$$

where $\mathbf{n}$ is the vector normal to the surface. We can simplify this equation by introducing the demagnetization field tensor $\hat{N}$:

$$\mathbf{H}_{\mathrm{dem}} = \hat{N}\mathbf{M}. \tag{2.15}$$

$\hat{N}$ describes the geometry of the sample and has been calculated for thin magnetic films [Kal86] and ferromagnetic wires [Gus02]. For complex two-dimensional structures as described in this thesis, an analytical solution does not yet exist.

Further energy contributions are the energy of magnetic moments in an external field $\mathbf{H}$

$$E_{\mathrm{ext}} = -\mu_0\int \mathbf{M}\mathbf{H}, \tag{2.16}$$

and crystal anisotropy that is disregarded in this thesis, as all studied materials proved to exhibit only negligible magnetic anisotropy. An equilibrium magnetic configuration of the system is found, when all discussed energy contributions are minimized in sum. In the equilibrium state, magnetic moments may point to different directions locally. Usually magnetic domains of areas exhibiting identical orientation may form as a trade-off between minimizing uncompensated charges at the sample border, and thus $\mathbf{H}_{\mathrm{dem}}$ and minimizing the angle between spins, and thus $\mathbf{H}_{\mathrm{exch}}$. This can lead to complex patterns and a complex response of the magnetization $\mathbf{M}$ on the external field $\mathbf{H}$. Such phenomena will play a role in the dynamic studies performed in this work and will be addressed in more detail in the

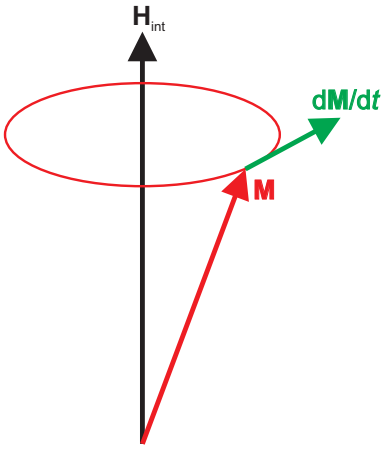

Figure 2.1: Precessional motion of the magnetization $\mathbf{M}$ around the effective internal field $\mathbf{H}_{\mathrm{int}}$. $\frac{\mathrm{d}\mathbf{M}}{\mathrm{d}t}$ is perpendicular to the field and the magnetization and describes the precession. If the motion is damped, the radius of precession is continuously decreased until $\mathbf{M}$ and $\mathbf{H}$ are aligned.

corresponding sections.

2.2 Magnetization Dynamics

After discussing relevant contributions to static magnetism, we now turn to magnetization dynamics. In the macrospin model all magnetic moments are summed up to one single spin representing the material. We will use the magnetization $\mathbf{M}$ as the macrospin, considering equation 2.2. Experimentally we can saturate the ferromagnet using a high external field $\mathbf{H}$ so that the energy in the external field E_{ext} is the dominating energy. We now define τ as the torque acting on the magnetization $\mathbf{M}$ in an external field in order to align it (see Fig. 2.1):

$$\tau = \mu_0 \mathbf{M} \times \mathbf{H}. \tag{2.17}$$

For a single spin in a material one sums up the contribution of exchange and demagnetization fields to the internal net field (sum of all field contri-

butions) $\mathbf{H}_{\mathrm{int}} = \mathbf{H} + \mathbf{H}_{\mathrm{exch}} + \mathbf{H}_{\mathrm{dem}}$. This internal net field is often called effective field, if further terms enter, such as magnetic anisotropy fields.

The magnetic moments are coupled to the angular momentum $\mathbf{J}$ by a fixed ratio γ:

$$\mathbf{m} = \gamma \mathbf{J}. \tag{2.18}$$

Considering the equation of motion

$$\tau = \frac{\mathrm{d}\mathbf{J}}{\mathrm{d}t}\ , \tag{2.19}$$

we equal Eqs. 2.17 and 2.19 and substitute $\mathbf{J}$ using Eg. 2.18 and taking the density into account in order to get the macrospin equation of motion:

$$\frac{\mathrm{d}\mathbf{M}}{\mathrm{d}t} = -|\gamma|\mu_0 \mathbf{M} \times \mathbf{H}. \tag{2.20}$$

This equation does not contain any damping terms. We introduce a phenomenological damping term that was first introduced by Landau and Lifshitz [Lan35]:

$$\tau_{\mathrm{LL}} = -\frac{\lambda}{M_{\mathrm{sat}}} \mathbf{M} \times (\mathbf{M} \times \mathbf{H})\ , \tag{2.21}$$

where λ is a phenomenological damping parameter. The equation fails for large λ, so Gilbert proposed [Gil55] a different damping term:

$$\tau_{\mathrm{G}} = \frac{\alpha}{M_{\mathrm{sat}}} \mathbf{M} \times \frac{\partial \mathbf{M}}{\partial t}. \tag{2.22}$$

This Gilbert damping term can be formulated similar to the Landau-Lifshitz form, using vector multiplication of the equation with $\mathbf{M}$:

$$\frac{\mathrm{d}\mathbf{M}}{\mathrm{d}t} = -\frac{\gamma}{1+\alpha^2} \mathbf{M} \times \mathbf{H} - \frac{\gamma\alpha}{(1+\alpha^2) M_{\mathrm{sat}}} \mathbf{M} \times (\mathbf{M} \times \mathbf{H}). \tag{2.23}$$

For small α both equations are equivalent with $\lambda = \alpha\gamma\mu_0 M_{\mathrm{sat}}$ [Mal87]. For materials in this thesis typically $\alpha \approx 10^{-2}$ so that we can simplify to:

$$\frac{\mathrm{d}\mathbf{M}}{\mathrm{d}t} = -\gamma \mathbf{M} \times \mathbf{H} - \frac{\gamma\alpha}{M_S} \mathbf{M} \times (\mathbf{M} \times \mathbf{H}). \tag{2.24}$$

In this thesis we study spin excitations in ferromagnetic thin films, so it is interesting to solve equation 2.24 for this special case. We assume several simplifications to achieve this. As we treat a thin film, only the z-component $N_z = 1$ of the demagnetization tensor $\hat{N}$ is non-zero. Further we assume that $\mathbf{M} \parallel \mathbf{H} \parallel \hat{\mathbf{x}}$ while the excitation field is perpendicular: $\mathbf{h}_{\mathrm{exc}} = h_{\mathrm{exc}} \exp(\mathrm{i}\omega t)\hat{\mathbf{y}}$. Further we only take into account small opening angles of the precession and we consider uniform excitation, i.e. a wavevector $k = 0$. Solving under these conditions we receive following Ref. [Cou04] the susceptibility $\chi(\omega)$:

$$\chi(\omega) = \frac{\omega_M(\omega_H + \omega_M - \mathrm{i}\alpha\omega)}{\omega_r^2 - \omega^2 - \mathrm{i}\alpha\omega(2\omega_H + \omega_M)}, \tag{2.25}$$

where $\omega_M = \gamma\mu_0(1+\alpha^2)M_{\mathrm{sat}}$, $\omega_H = \gamma\mu_0(1+\alpha^2)H$, and $\omega_r = (\omega_H^2 + \omega_M\omega_H)^{\frac{1}{2}}$. This uniform excitation is called ferromagnetic resonance (FMR). We can obtain the resonance frequency in FMR:

$$f_{\mathrm{res}} = \frac{\gamma\mu_0}{2\pi}(H^2 + M_{\mathrm{sat}}H)^{\frac{1}{2}}. \tag{2.26}$$

This equation can be used for determining M_{sat} from H-dependent FMR resonance measurements [Kit68]. One gets the effective magnetization if surface anisotropy terms are present in a real sample.

We further evaluate the imaginary part of Eq. 2.25:

$$\Im(\chi(\omega)) = \frac{\alpha\omega\omega_M(\omega^2 + (\omega_H + \omega_M^2))}{(\omega_r^2 - \omega^2)^2 + \alpha^2\omega^2(2\omega_H + \omega_M)^2}. \tag{2.27}$$

The imaginary part of χ can be approximated by a Lorentz function. The full width at half maximum (FWHM) is then defined as the linewidth of the susceptibility. For resonance frequencies larger than the linewidth $\Delta\omega$ one can approximate by [Neu11a, Bil07a]:

$$\Delta\omega = \alpha\gamma\mu_0 M_{\mathrm{sat}}. \tag{2.28}$$

Here in α and $\Delta\omega$ the microscopic origin of damping processes is not considered, but rather considered as effective values. Following [Kam75, Kua05, Kal06] the frequency linewidth Δf as it is accessible to measure-

ments performed in this thesis is formulated as follows:

$$\Delta f = \left(\frac{\gamma \Delta H_0}{2\pi} + 2\alpha_i f_{\mathrm{res}}\right)\left(1 + \left(\frac{\gamma \mu_0 M_{\mathrm{sat}}}{4\pi f_{\mathrm{res}}}\right)^2\right)^{\frac{1}{2}}, \tag{2.29}$$

where ΔH_0 quantifies the extrinsic field-swept linewidth contributions and α_i only intrinsic contributions to α.

2.3 Spin Waves

FMR resonance as described in the previous chapter applies to $k = 0$. It is further possible to solve the equation of motion for $k \neq 0$ and thus solve the equation for propagating spin waves. For this section we study spin waves in an infinite film of thickness t in the xy-plane. $\mathbf{H}_{\mathrm{int}}$ and $\mathbf{M}$ are parallel and in the film plane. The wave vector $\mathbf{k}$ consists of an in-plane component $\mathbf{k}_{\mathrm{in}}$ and an out-of-plane component $\mathbf{k}_{\mathrm{out}}$. The out-of-plane component $\mathbf{k}_{\mathrm{out}}$ is quantized due to the finite thickness of the film [Gur96]:

$$\mathbf{k}_{\mathrm{out}} = n\frac{\pi}{t}, n \in \mathbb{N}_0. \tag{2.30}$$

In this thesis, only excitations with $n = 0$ are considered. The amplitude resembles an evanescent wave as the amplitude decreases exponentially from one surface to the other [Dam61]. We further separate $\mathbf{k}_{\mathrm{in}}$ into contributions parallel to the magnetic field and magnetization ($\mathbf{H}_{\mathrm{int}}$ and $\mathbf{M}$) $k_\parallel$ and a perpendicular contribution $k_\perp$, so that

$$\mathbf{k}_{\mathrm{in}} \cdot \mathbf{k}_{\mathrm{in}} = k_\parallel^2 + k_\perp^2 \tag{2.31}$$

holds true. Following [Kal86] we state that the dispersion of spin waves with out-of-plane quantization number n is

$$\omega_n^2 = (\omega_H + \alpha\omega_M k^2)[\omega_H + \omega_M(\alpha k^2 + F_{nn}(k_{\mathrm{out}}))], \tag{2.32}$$

where

$$F_{nn}(k_{\mathrm{out}}) = 1 - P_{nn}\cos^2\varphi + \omega_M \frac{P_{nn}(1 - P_{nn})\sin^2\varphi}{\omega_H + \alpha\omega_M k_{\mathrm{out}}^2} \tag{2.33}$$

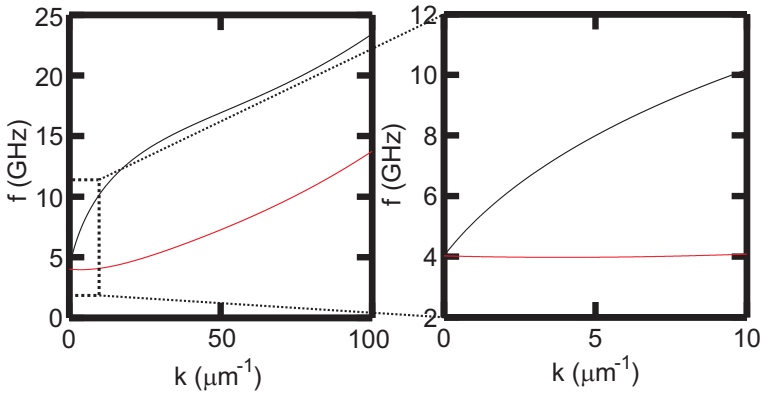

Figure 2.2: Calculated spin-wave dispersion $f(k)$ for $\mu_0 H = 20$ mT. The black (red) line shows the case $\eta = 0°$ ($\eta = 90°$), i.e. the MSSW (MSBVW) mode. The dispersions have been calculated using Eq. 2.32. Further parameters were $t = 25$ nm, $M_{\mathrm{sat}} = 806$ kA/m.

and

$$P_{nn} = \frac{k_{\mathrm{in}}^2}{k_{\mathrm{out}}^2} + \frac{2}{d}\frac{k_{in}^3}{k_{\mathrm{out}}^3}\frac{1}{1+\delta_{0n}}[1-(-1)^n \exp(-k_{\mathrm{in}}t)]. \tag{2.34}$$

F_{nn} quantifies the dipolar interaction and strongly modifies the dispersion for small k, where it deviates from a quadratic exchange-interaction dominated dispersion. This is the case for wave vectors $\mathbf{k}$ smaller than ≈ 100 μm^{-1}.[1]

In Fig. 2.2 we show the calculated spin-wave dispersion using these formulas using $\mu_0 H$ =20 mT, $M_{\mathrm{sat}} = 806$ kAm^{-1}, $t = 25$ nm. These values are similar to experimental sample parameters relevant in this thesis. The black (red) curve denotes the extreme case of $\mathbf{k} \perp \mathbf{M}$ ($\mathbf{k} \| \mathbf{M}$) that is also called Damon-Eshbach or magnetostatic surface wave (MSSW) mode (backward volume or magnetostatic backward volume wave (MSBVW) mode). The strong anisotropy of spin-wave propagation is clearly seen. Furthermore the quadratic dispersion for the exchange-dominated high-k regime can be distinguished from the dipole-dipole interaction dominated

[1] The unit of $\mathbf{k}$ can also be stated as rad/μm. Here we use 1/μm, which should not be confused with the unit for wave numbers, also 1/μm.

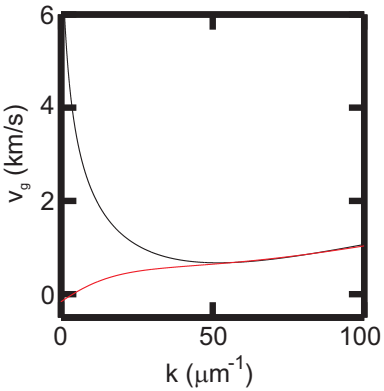

Figure 2.3: Calculated group velocity $v_g(k)$ obtained from differentiation of Eq. 2.32 for $\mu_0 H = 20$ mT. The black (red) line shows the case $\eta = 0°$ ($\eta = 90°$), i.e. the MSSW (MSBVW) mode. Further parameters were $t = 25$ nm, $M_{\mathrm{sat}} = 806$ kA/m.

low-k regime.

We now calculate the group velocity v_g from the dispersion relation using

$$v_g = \frac{\partial \omega}{\partial k} = 2\pi \frac{\partial f}{\partial k}. \tag{2.35}$$

In Fig. 2.3 we show v_g calculated from the dispersion relation shown in Fig. 2.2. Again the black (red) curve denotes the MSSW (MSBVW) mode. The negative v_g for the MSBVW mode for small k is clearly resolved. Further we find that v_g decreases with increasing k for small k until increasing linearly in the exchange-dominated high-k-regime.

For propagating spin waves we also take into account damping. For each individual spin one can assume, following [Sil99], an exponentionally damped magnetization angle φ, where $\varphi = 0$ is the equilibrium position:

$$\varphi(t) = \varphi_0 \sin(\omega + \zeta) \exp(-\frac{t}{\tau}), \tag{2.36}$$

where φ_0 is the maximum angle, ζ is an arbitrary phase shift, and τ is a

relaxation parameter connected to α by

$$\alpha = \frac{2}{\gamma \mu_0 M_{\mathrm{sat}} \tau}. \tag{2.37}$$

Thus the relaxation time τ is connected to the frequency linewidth $\Delta\omega$ in Eq. 2.28. For propagating spin waves we can further define the reciprocal spatial decay length λ

$$\lambda = \frac{1}{v_g \tau}, \tag{2.38}$$

where λ quantifies decay in space.

2.4 Numerical Methods

2.4.1 Micromagnetic Simulations

In this thesis we have performed micromagnetic simulations using the MicroMagus software package [Ber08] in versions 6 and 7. Micromagnetic simulations calculate the static magnetic configuration of a given system numerically by minimizing the total energy, taking into account all magnetic field contributions as discussed above. By solving the equation of motion (e.g. Eq. 2.24) numerically, the response of the magnetic system to a dynamic perturbation can further be found. We use simulations in order to advance the understanding of experimental data.

In general two methods are possible for discretizing the simulated sample: the finite element approach, where a simulation mesh is formed to reproduce the sample, and the relevant equations are solved for mesh nodes, and the finite difference approach, where the structure is divided into pixels or voxels of nonzero volume. Micromagus is a finite difference simulation software, so the ferromagnetic sample is divided into layers of nonzero volume, and each layer is discretized into N pixels of volume V_i and magnetization $\mathbf{M}_i$ for $i = 1...N$. The energy of each pixel considering the energy in the external field $\mathbf{H}$, in the exchange field $\mathbf{H}_{\mathrm{exch}}$, and in the demagnetization field $\mathbf{H}_{\mathrm{dem}}$ is summed up to form the total energy of the system. For every iteration step the internal field $\mathbf{H}_{\mathrm{int},i}$ is calculated for each pixel i from $\mathbf{H}_{\mathrm{int},i} = -\frac{\delta E}{\delta \mathbf{M}_i}$. Then it is tested if $\mathbf{H}_{\mathrm{int},i}$ and $\mathbf{M}_i$ align within a given threshold, i.e. if a minimum remaining torque is reached. If

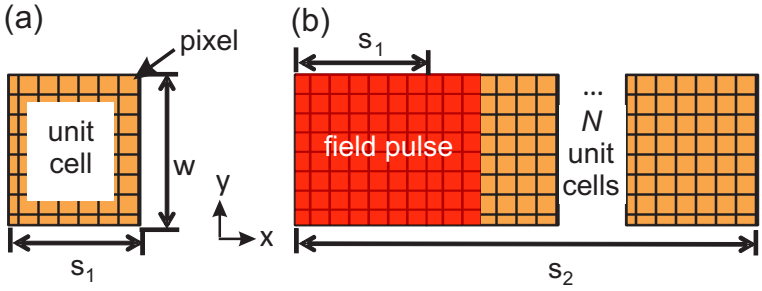

Figure 2.4: Schematic illustration of micromagnetic simulation layouts. (a) Layout used for $k = 0$ simulations. One unit cell is used with 2D periodic boundary conditions in the xy plane. In z direction, i.e. out-of-plane, the structure consists of several layers. The unit cell ins subdivided into quadratic pixels. The whole unit cell is excited homogeneously by the excitation field pulse. (b) Layout used for $k > 0$ simulations. The unit cell of length s_1 is repeated N times. 2D boundary conditions are used. The field pulse is applied over the red area. Spin waves with $k > 0$ traveling along x are resolved.

not, a new magnetization configuration is calculated by Eq. 2.24, neglecting precession, thus finding the equilibrium state (see also Ref. [Hil02]). For dynamic simulations, Eq. 2.24 is solved numerically, using static simulations for the ground state.

In this thesis two different generalized simulation geometries have been used, illustrated in Fig. 2.4. In Fig. 2.4 (a) we show the simulation geometry for $k = 0$ simulations. Here one unit cell of the structure is discretized into pixels as described above. 2D periodic boundary conditions are used, resulting in an effective infinitely large structure in the xy plane. In a first step the equilibrium static magnetization at a given field after previous saturation is calculated for the structure, delivering $\mathbf{M}(\mathbf{r})$ and $\mathbf{H}_{\mathrm{dem}}(\mathbf{r})$. Then in dynamic simulations, a field pulse is applied spatially uniform all over the unit cell. This leads to $k = 0$ excitation, i.e. FMR simulation. The field pulse is typically of Gaussian shape while the FWHM of the pulse is typically 3 ps, so that frequencies up to 26.5 GHz, that can be detected by the experimental setup, can be generated in simulations. The field pulse is applied at the beginning of a 6 ns long time-domain dynamic simulation that yields $\mathbf{M}(\mathbf{r}, t)$ data. Due to the uneven temporal spacing of the data a least-squares spectral analysis (also known as Lomb method) is performed

to calculate the frequency spectrum: $P(f, \mathbf{r})$. To judge the contribution of each frequency f a power spectrum of the out-of-plane (z-axis) magnetization of the average over all pixels i is formed. Then spatial power plots $P(f', \mathbf{r})$ for a given frequency f' of significantly high spectral power can be produced, showing localization of spin precession for a mode at f' [Neu06a].

In order to simulate the dispersion for spin waves, i.e. perform simulations at $k \neq 0$, we have used the geometry shown in Fig. 2.4 (b). Here spin wave propagation along the x-axis with the corresponding wave vector k_x is analyzed. Along the x-axis a number of unit cells of the structure as used for $k = 0$ simulations is repeated until the structure is approx. 20 µm long, consistent with propagation lengths studied in experiments. An area that covers 2.4 by 1 unit cells in x and y directions is excited by a field pulse. It is vital to not cover an integer multiple of unit cells in propagation direction, as this will lead to zero signal in the k space power spectrum at the Brillouin zone boundaries. Simulations are performed for 10 ns again, yielding $\mathbf{M}(\mathbf{r}, t)$. A spatio-temporal, i.e. double, fast Fourier Transformation is performed after interpolating the data to equal time steps. The result is a $P(f, k)$ power spectrum that produces the dispersion relation $f(k)$ of the system [Kru06].

2.4.2 Plane Wave Method

In this thesis we use calculations obtained from the plane wave method (PWM) performed by Dr. J. Kłos and Dr. M. Krawczyk at Adam Mickiewicz University in Poznań, Poland [Kra08]. For this method firstly the demagnetization field $\mathbf{H}_{\mathrm{dem}}$ is calculated using methods that are described in [Klo12, Kac74]. Note that only the field contribution to $\mathbf{H}_{\mathrm{dem}}$ in x-direction is calculated. Then Eq. 2.24 is solved numerically for zero damping, i.e. $\alpha = 0$, taking into account external, exchange and demagnetization fields. Then Bloch waves are used as an ansatz for the solution:

$$\mathbf{M}(\mathbf{r}, t) = \sum_{\mathbf{G}} \mathbf{M}_{\mathbf{k}}(\mathbf{G}) \exp(\mathrm{i}(\mathbf{k} + \mathbf{G}) \cdot \mathbf{r}) \exp(\mathrm{i}\omega t), \tag{2.39}$$

where $\mathbf{G}$ is a reciprocal lattice vector. By solving Eq. 2.24 in reciprocal space, an eigenvalue and eigenvector problem for f and $\mathbf{M}_{\mathbf{k}}(\mathbf{G})$ is obtained and solved numerically. The intensity of a mode is judged by the

squared amplitude of the Fourier component $I \propto |\mathbf{M}_{y,\mathbf{q}}(0)|^2$. An important assumption of the PWM is the uniformity of the sample in z, i.e. out-of-plane, direction. For nonhomogeneous samples an effective thickness is introduced and fit to experimental data.

3 Experimental Techniques

In the course of this thesis several experimental techniques have been employed either in the own laboratory or in cooperation with further experimental groups. All techniques are complementary as they allow access to different properties of the sample. We will describe the methods all electrical spin-wave spectroscopy, conventional and microfocused Brillouin light scattering, and magnetic X-ray transmission microscopy.

3.1 All-electrical Spin Wave Spectroscopy

3.1.1 Experimental Setup

The experimental setup for all-electrical spin wave spectroscopy (AESWS) provides an integration of broadband microwave electronics, magnetic field supply and automated data acquisition. We have used a probe station at TUM that allows an all-electrical study of spin-waves.

In Fig. 3.1 we show a close-up photograph of the experimental setup. This setup consists of the following parts:

- The sample, comprising the magnetic film and coplanar waveguides (CPWs), see below and [Wen69]. The sample is fixed by suction. The sample stage comprises small holes connected to a vacuum pump. The sample is only sucked to the sample stage during initial contact to microwave probes. During measurement, the vacuum pump is switched off to reduce vibrations.

- Microwave probes FPC-GSG[1] that consist of one signal and two ground lines of 100 µm or 250 µm pitch and provide 50 Ω impedance. The probe contacts provide direct mechanical and electrical contact to the CPW pads on the sample.

[1] Cascade Microtech, Inc., Beaverton, OR, USA

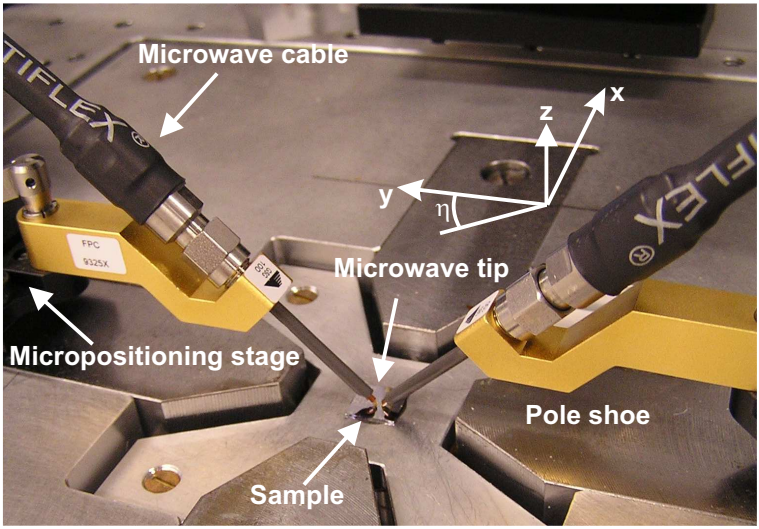

Figure 3.1: Photograph of the experimental AESWS setup. Here the sample and its immediate surrounding is seen. Two micropositioning stages allow exact control over the contact between microwave probe tips and CPW contact pads on the sample. Iron pole shoes guide the magnetic field from two field coil pairs to the sample. Microwave cables provide impedance matched waveguides from the VNA (not shown) to the microwave probe tips. The whole setup is placed on a vibration damping table.

- A mechanical micropositioning system, allowing exact contact of the probes and the CPW pads. The microwave probes are fixed to the micropositioning system.

- Semi-rigid cables UFA-210A[1], providing impedance matched micowave transmission between the measurement apparatus and the microwave probes.

- A vector network analyzer (VNA) PNA-X N-5242A[2] providing broadband microwave measuremens from 10 MHz to 26.5 GHz. The

[1] Rosenberger Hochfrequenztechnik GmbH & Co. KG
[2] Agilent Technologies, Inc., Santa Clara, CA, USA

VNA provides two ports. It outputs a sinusoidal microwave signal at one port, and measures amplitude and phase of the received microwave signal at both ports, providing vector signals as output. The output power is typically 1 mW or less.

- Two pairs of coils, each connected to ferromagnetic Fe pole shoes provide a near uniform in-plane magnetic field $\mathbf{H}$ throughout the sample. Up to $\mu_0|\mathbf{H}| = 120$ mT are generated. The two coils and pole shoes are arranged perpendicularly and controlled independently in order to allow application of $\mathbf{H}$ at an arbitrary in-plane angle η by superposition of the fields of both coil pairs.

- A magnetic field control system including feedback. Current to the field coils is supplied by a bipolar operation power supply / amplifier BOP 20-10M[1]. The supplied field is measured constantly by a three-axis Hall sensor beneath the sample. Hall sensor data is amplified by a lock-in amplifier. The BOP is configured in a manner that it changes the output voltage until the voltage input and the Hall sensor output agree. For this, an initial calibration curve of the Hall sensor signal was performed, using a pre-calibrated external Hall sensor. The voltage input to the BOP is supplied by a DC-calibrator J152[2]. For each field coil pair, one Hall sensor axis, BOP and DC-calibrator is used, each. Due to the feedback of the Hall sensors, any fluctuations as well as hysteresis of the pole shoes, are compensated actively.

- An automatic data acquisition and control software run on a Windows XP[3] computer system. The measurement software controls the VNA and DC-calibrator and reads out and stores data acquired by the VNA and the Hall sensors. The software allows running predefined measurement and magnetic field supply routines independently from user input, allowing fully automated measurements.

- A shock-absorbing table that reduces vibrations from external sources. The whole setup is shielded by PVC curtains providing protection

[1] Kepco, Inc., Flushing, NY, USA
[2] Knick Elektronische Messgeräte GmbH & Co. KG, Berlin
[3] Microsoft Corp., Redmond, WA, USA

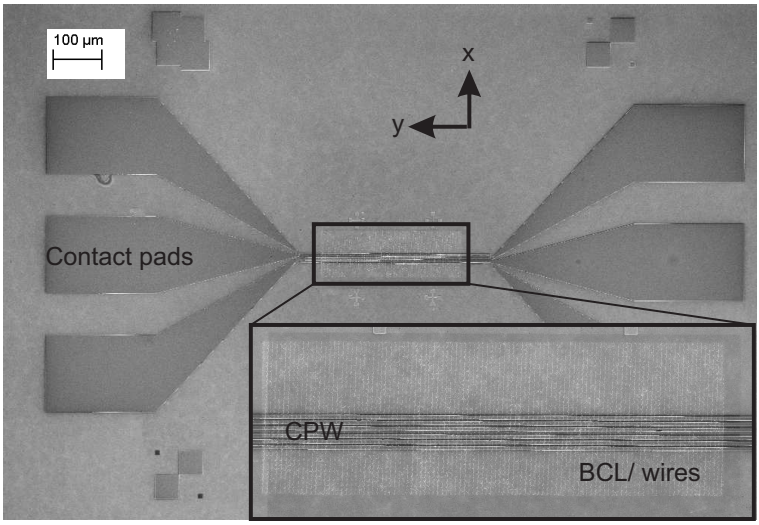

Figure 3.2: Scanning electron micrograph of a typical sample. Visible is a $w_{\mathrm{IC}} = 2$ µm CPW covering a Py mesa (gray square) structured as BCL (the borders of Co dots are seen as white rings). Contact pads allow a large contacting surface for microwave probe tips. Furthermore alignment markers are shown. These markers are used for EBL alignment and alignment of the CPW with respect to the mesa. Here the coordinate system used throughout this thesis is defined with respect to the sample.

from dust and air draft. The setup is placed in an air conditioned room.

3.1.2 Sample Design

In Fig. 3.2 we show a scanning electron micrograph of a typical sample. On top of an insulating substrate, the magnetic sample, a nanostructured thin film is prepared. The magnetic film is covered by an electrical insulator. On top of the insulator CPWs are prepared, consisting of electrically conducting metals. See chapter 4 for details on preparation and materials. In Fig. 3.2 the coordinate system is defined, with the x axis perpendicular to the CPW and the y axis parallel to the CPW. On each end, the CPW provides three contact pads, where mechanical and electrical contact

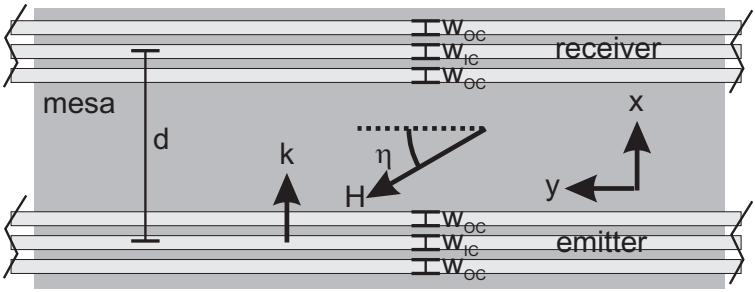

Figure 3.3: Sketch of the sample geometry. The coordinate system with x and y axis in plane is defined. The z axis is pointing perpendicular to xy out of plane. The angle η defines the angle of the external field $\mathbf{H}$ with respect to the y axis, i.e. the CPW. The wavevector $\mathbf{k}$ is always parallel to the x axis and perpendicular to the CPW. We further define the propagation distance d between the center of the emitter part of the CPW and the receiver part of the CPW, and the conductor widths $w_{\mathrm{IC}} = w_{\mathrm{OC}}$.

between CPW and microprobes takes place. The contact pads taper into smaller lines that feed the microwave to the magnetic sample (see inset of Fig. 3.2). In this thesis we use CPWs where all lines of a given CPW have identical width [Pon97, Pon98].

In Fig. 3.3 we show a schematic sketch of the sample region. Here we depict SW-transmission CPWs. Each triple of contact pads is connected to three electrical contact lines that end open on the other end of the mesa. This is in contrast to conventional CPWs, where one triple of lines connects both contact pad areas. Here the two contact pad regions are electrically isolated. Each part of the CPW consists of one central inner conductor line of width w_{IC} and two outer conductor lines of width w_{OC}. The inner conductor line is connected to the VNA via the microwave probes and the signal line of the coaxial microwave cable, while the outer conductor lines are connected to the VNA via the ground of the cable. SW-transmission CPWs are characterized by the conductor line widths $w_{\mathrm{IC}} = w_{\mathrm{OC}}$, conductor line distances d_{C} and the distance between the signal line centers d. We call one half of the CPW emitter, the other half receiver.

3.1.3 Signal Generation and Detection

For AESWS spin-waves of nonzero wave vector k are excited by the emitter part of the CPW, propagate over the distance d between emitter and receiver and are received by the receiver part of the CPW. This technique is also known as propagating spin-wave spectroscopy [Mel01, Bai01, Bai03, Bao08] if a VNA is used as measurement apparatus. Time-domain measurements have also been performed [Cov02, Liu07, Sek10]. The VNA generates and detects sinusoidal voltage signals

$$V(r,t) = \bar{V}(x)\exp(i\omega t) \tag{3.1}$$

that propagate as waves through microwave cables and the CPW. The local voltage V and current I depend on the coordinate r in the propagation path, depending on local resistance R, inductance L, and respectively conductance G and capacitance C. Elaborating on Ohm's law, we can state for V following from now on [Bil07a]:

$$-\frac{\partial V}{\partial r} = RI + L\frac{\partial I}{\partial t}, \tag{3.2}$$

and we can state for I

$$-\frac{\partial I}{\partial r} = GV + C\frac{\partial V}{\partial t}. \tag{3.3}$$

Using Eq. 3.1 we can solve the partial differentiation for t. This system can be solved with backward and forward travelling waves

$$\begin{aligned}\bar{V}(r) &= \bar{V}^{+}\exp(-\kappa r) + \bar{V}^{-}\exp(\kappa r)\\ \bar{I}(r) &= \bar{I}^{+}\exp(-\kappa r) + \bar{I}^{-}\exp(\kappa r).\end{aligned} \tag{3.4}$$

with

$$\kappa = (R + i\omega L)^{\frac{1}{2}}(G + i\omega C)^{\frac{1}{2}}, \tag{3.5}$$

and $\bar{V}^{+}$, $\bar{V}^{-}$, $\bar{I}^{+}$, and $\bar{I}^{-}$ are integration constants. We can further define the impedance Z of the system

$$Z = \frac{\bar{V}^{+}}{\bar{I}^{+}} = \frac{\bar{V}^{-}}{\bar{I}^{-}}. \tag{3.6}$$

The canonical way of treating propagating voltage and current waves in a two port network, i.e. any device under test connected to a VNA with two ports is using the scattering parameters (S-parameters). For this, complex and normalized waves a_i and b_i for each port i are defined as follows:

$$\begin{aligned} a_i &= \frac{V_i + Z_i I_i}{2 Z_i^{\frac{1}{2}}} \\ b_i &= \frac{V_i - Z_i I_i}{2 Z_i^{\frac{1}{2}}}. \end{aligned} \tag{3.7}$$

The voltages V_i and currents I_i can be calculated using the relations

$$\begin{aligned} V_i &= Z_i^{\frac{1}{2}} (a_i + b_i) \\ I_i &= \frac{a_i - b_i}{Z_i^{\frac{1}{2}}}. \end{aligned} \tag{3.8}$$

The formulation using a_i and b_i is motivated by introducing $\bar{V}(r)$ and $\bar{I}(r)$ from Eqs. 3.4 into Eqs. 3.7. It is clear that a_i is the incident and b_i the outgoing voltage wave at port i:

$$\begin{aligned} a_i &= V_i^+ Z_i^{-\frac{1}{2}} \exp(-\kappa r) \\ b_i &= V_i^- Z_i^{-\frac{1}{2}} \exp(\kappa r). \end{aligned} \tag{3.9}$$

This allows definition of scattering parameters (or S-parameters) S_{ij} for a two-port network:

$$\begin{pmatrix} b_1 \\ b_2 \end{pmatrix} = \begin{pmatrix} S_{11} & S_{12} \\ S_{21} & S_{22} \end{pmatrix} \begin{pmatrix} a_1 \\ a_2 \end{pmatrix}. \tag{3.10}$$

Note that $S_{ij}(\omega)$ is depending on the excitation frequency $\omega = 2\pi f$ of the VNA.

The propagating voltage/current waves in the CPW produce a magnetic field oscillating as well with frequency ω, according to Biot-Savart's law. This oscillating excitation field $\mathbf{h}_{\mathrm{exc}}$ excites spin precession in the vicinity of the CPW. h_{exc} encircles the rectangularly shaped inner and outer conductor lines of the CPW. Beneath the CPW we receive in the material

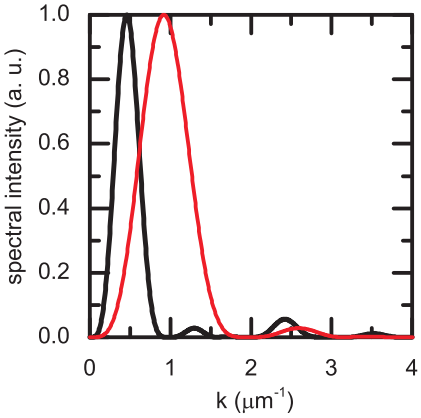

Figure 3.4: Spectral intensity $\xi(k)$ of a $w_{\mathrm{IC}} = 4$ µm, $d_{\mathrm{C}} = 2.4$ µm ($w_{\mathrm{IC}} = 2$ µm, $d_{\mathrm{C}} = 1.2$ µm) CPW shown by the black (red) curve. Data has been obtained by a Fourier transform of the spatial current density of the CPW.

contributions $h_{\mathrm{exc},x}$ along the x axis, perpendicular to the current along the CPW (y-axis, see Fig. 3.3). At the edges of the conductor lines we also receive out-of-plane components $h_{\mathrm{exc},z}$. As currents in the outer conductors have opposite direction to the current in the inner conductor, $h_{\mathrm{exc},x}$ varies strongly spatially in the magnetic film. While the spatial magnetic field of the CPW can be simulated using finite element electromagnetic field solvers, we can use valid approximations of the spatial field as introduced in [Cou04, Ken07, Neu11a]. Firstly, we can neglect $h_{\mathrm{exc},z}$ as due to the flatness and width of the used conducting lines, the contribution of $h_{\mathrm{exc},x}$ is much higher [Neu11a]. Furthermore we can assume normalized $h_{\mathrm{exc},x}/h_0 = 1$ exactly beneath the inner conductor line, $h_{\mathrm{exc},x}/h_0 = 0$ between lines, and $h_{\mathrm{exc},x}/h_0 = -0.5$ beneath outer conductor lines. While this neglects the far field of the conductor lines it compared within a margin of 10-15% with rigourous simulations. This significant spatial inhomogenity is used in AESWS to excite spin waves of nonzero wave vector k. A Fourier transformation of $h_{\mathrm{exc},x}$ yields an approximation the excitation intensity $\xi(k)$ in k-space.

In Fig. 3.4 we show $\xi(k)$ as obtained from the Fourier transformation of the approximated $h_{\mathrm{exc},x}$ for two different CPWs used in this thesis;

$w_{\mathrm{IC}} = 4$ µm, $d_{\mathrm{C}} = 2.4$ µm ($w_{\mathrm{IC}} = 2$ µm, $d_{\mathrm{C}} = 1.2$ µm) CPW represented by the black (red) curve. The used geometrical values are nominal values defined by the lithography mask. We found that in the experiment, CPW geometries deviated from the nominal values due to imperfections in the lithographical process by up to several µm. We recognize several maxima, while secondary maxima are smaller in intensity by more than 90%. This is in accordance with rigorous simulations as performed in [Neu11a]. The nonzero width of $\xi(k)$ peaks leads due to the dispersion $f(k)$ of spin waves to a nonzero width Δf in excitation of a given mode. This is used in data interpretation in AESWS to gain insight on the slope of $f(k)$, and also leads to inhomogeneous line broadening of the resonances.

As the excited spin waves are of nonzero wavevector k, they propagate from the emitter part of the CPW to the receiver part of the CPW, where due to precessing spins and a resulting dynamic magnetic field $\mathbf{h}_{\mathrm{rec}}$ a voltage is induced in the CPW. Following [Gie05b, Sil99] in the case of a continuous conventional CPW, the flux in a CPW Φ_{CPW} caused by a magnetic sample of magnetization $\mathbf{M}$ is

$$\Phi_{\mathrm{CPW}} = \mu_0 \int_{V'} \frac{\mathbf{h}_{\mathrm{CPW}}}{I} \cdot \mathbf{M} \mathrm{d}V, \tag{3.11}$$

where V' is the sample volume and $\mathbf{h}_{\mathrm{CPW}}$ is the field created by the CPW and is equivalent to the field by the exciting CPW part $\mathbf{h}_{\mathrm{exc}}$ as defined above, and I is the current in the CPW. Here, as we use spin-wave transmission CPWs, we replace $\mathbf{h}_{\mathrm{CPW}}$ with the dynamic magnetic field beneath the receiving CPW as caused by propagating spin waves $\mathbf{h}_{\mathrm{rec}}$:

$$\Phi_{\mathrm{rec}} = \mu_0 \int_{V'} \frac{\mathbf{h}_{\mathrm{rec}}}{I_2} \cdot \mathbf{M} \mathrm{d}V. \tag{3.12}$$

As introduced above for $\mathbf{h}_{\mathrm{CPW}}$ we simplify $\mathbf{h}_{\mathrm{rec}}$ to include only in-plane contributions and define it by the current I_2 in the receiver CPW part and the width of the conducting line w:

$$\mathbf{h}_{\mathrm{rec}} = f(x) \frac{I_2}{w} \hat{\mathbf{x}}, \tag{3.13}$$

where $f(x)$ is a normalized spatial distribution function of $\mathbf{h}_{\mathrm{rec},x}$. Thus we can formulate

$$\Phi_{\mathrm{rec}} = \frac{\mu_0 t l \sin(\beta)}{w} \int \mathrm{d}x (f(x) M_x(x,t)), \tag{3.14}$$

where l is the conductor length, t the thickness of magnetic material, β the angle between $\mathbf{M}$ and the x-axis. We can finally determine the induced voltage V_{rec} by

$$V_{\mathrm{rec}} = -\frac{\mathrm{d}\Phi_{\mathrm{rec}}}{\mathrm{d}t} = -\frac{\mu_0 t l \sin(\beta)}{w} \int \mathrm{d}x f(x) \frac{\mathrm{d}M_x(x,t)}{\mathrm{d}t} = \tag{3.15}$$

$$= -\frac{\chi(\omega) \mu_0 t l \sin(\beta)}{w} \int \mathrm{d}x f(x) \frac{\mathrm{d}h_{\mathrm{exc},x}(x,t)}{\mathrm{d}t}, \tag{3.16}$$

where χ is the susceptibility of all contributing spin waves [Vla10]:

$$\chi(\omega) = \int \mathrm{d}k \chi'(\omega, k) \xi(k) \exp(-ikd). \tag{3.17}$$

$\xi(r)$ is, as introduced above the excitation efficiency for a given wavevector k, d is the propagation distance, thus we take into account attenuation of spin waves over d.

The overlap of $f(x)$ and $h_{\mathrm{exc},x}(x,t)$ quantifies excitation by the CPW emitter directly beneath the receiver. This is an unwanted effect in AESWS, as the signal is caused by crosstalk and not by propagating spin waves. It is out of the scope of this thesis to discuss χ in more detail. The reader is referred to [Kua05, Kal06, Bil07a, Vla10] where complete calculations of the induced voltage are presented and compared to experiments.

3.1.4 Data Analysis

In our experiments we have acquired S-parameters $S_{ij}(f, \mathbf{H})$. For a given external field $\mathbf{H}$ the excitation and detection frequency of the VNA f was swept in order to obtain $S_{ij}(f)|_{H,\eta}$ for a given amplitude H and angle η of the external field. In Fig. 3.5 we show exemplary $S_{12}(f)$ and $S_{21}(f)$ parameters obtained on a $t = 26$ nm Py plain film with $w_{\mathrm{IC}} = 2$ µm and

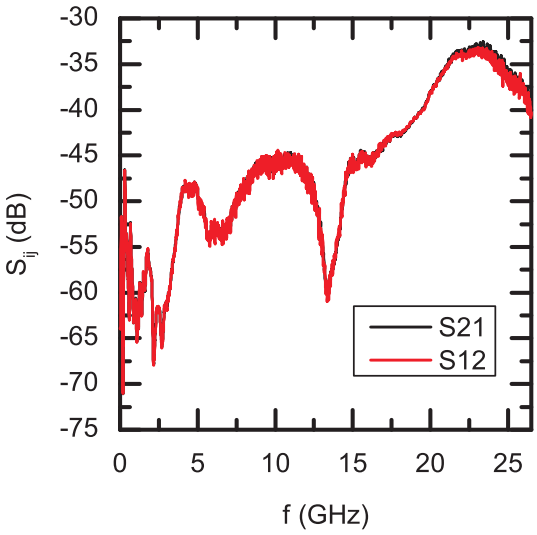

Figure 3.5: Raw data of the amplitude of S_{12} and S_{12} obtained on a $t = 26$ nm thick Py plain film with $w_{\mathrm{IC}} = 2$ µm and $d = 12$ µm wide spin-wave transmission CPW. The magnetic contribution to the signal is not seen here due to the small signal-to-noise ratio.

$d = 12$ µm CPW. Data is shown in dB where by definition

$$S_{ij}[dB] = 20\log(S_{21}) = 20\log\left(\frac{b_2}{a_1}\right). \tag{3.18}$$

These data reflect the frequency-dependent electromagnetic response of the CPW. The small values between -70 and -35 dB show good microwave isolation between emitter and receiver parts of the CPW. The frequency-dependent response can be in part remodelled and explained using finite-element simulations [Neu11a]. In order to increase the signal-to-noise ratio for the response of the magnetic system, we apply a difference technique. As $\eta = 90° - \beta$, we can see from Eq. 3.15 that for $\eta = 90°$ we expect minimum excitation. Thus we subtract from every acquired dataset an additional reference dataset acquied at $\eta = 90°$:

$$a_{ij}|_{H,\eta} = S_{ij}(f)|_{H,\eta} - S_{ij}(f)|_{100\ \mathrm{mT},90°}. \tag{3.19}$$

In the following we only consider a_{ij} data as a measure for χ.

In Fig. 3.6 we show AESWS data obtained on a Py plain film using a $w_{\mathrm{IC}} = 2$ µm, and $d = 12$ µm CPW, at $H = 10$ mT and $\eta = 0°$. In Fig. 3.6 (a) we show a_{22} data, namely $|a_{22}|$ (red), $\Re(a_{22})$ (blue), and $\Im(a_{22})$. These data are different from conventional VNA-FMR data [Gie05a, Neu06a, Bil07b, Bil07a] in that the sample is larger than w_{IC} and propagating spin waves are probed. The line shapes deviate from the shape of a classical harmonic oscillator. We attribute this to a deviation of the phase $\phi(a_{22})$ that causes distortions in line shape. These distortions are described in [Bil07b, Kal06] and stem from numerous microwave reflections throughout the setup, especially in the CPW. Contributions outside the CPW are reduced by calibration of the VNA using a calibration substrate. The contribution of each CPW is, however, individual and cannot be calibrated using a standard CPW. The authors of [Bil07b] propose for conventional CPWs an evaluation model that corrects these phase distortions by combining all four S-parameters. For conventional CPWs, errors due to phase distortions are below 1% for the resonance frequency f and below 10% for the resonance frequency linewidth Δf. The resonance frequency is clearly seen as the main peak in $|a_{22}|$. At 9 GHz one further resonance is seen that is attributed to the $H = 100$ mT, $\eta = 90°$ reference dataset that has been subtracted.

In Fig. 3.6 (b) we show phase data of a_{22} and a_{12}. The phase $\phi(f)$ of a_{22} (red curve) exhibits a change by approximately 180° at the resonance, as is expected from a harmonic oscillator. Outside of the resonant regime the base line of the phase varies significantly due to the aforementioned distortions. The black curve shows the phase of a_{12}, i.e. in transmission. The signal-to-noise ratio is significantly smaller compared to a_{22} data. In the frequency regime of the resonance the phase slope $\frac{\partial \phi}{\partial f}$ is significantly higher: At the resonance frequency $f_{\mathrm{res}} = 3.375$ GHz, $\frac{\partial \phi(a_{12})}{\partial f}(f_{\mathrm{res}}) = 9.4$ 1/GHz and $\frac{\partial \phi(a_{22})}{\partial f}(f_{\mathrm{res}}) = 1.6$ 1/GHz.

The phase shift in $\phi(a_{12})$ is caused by the nonzero width Δk of wave vector excitation [Mel01, Bai01, Bai03, Bao08]. All excited wavevectors, characterized by the distribution $\xi(k)$, see Fig. 3.4, contribute to the signal. All wavevectors k acquire a phase shift

$$\tilde{\Phi}(k) = kd, \tag{3.20}$$

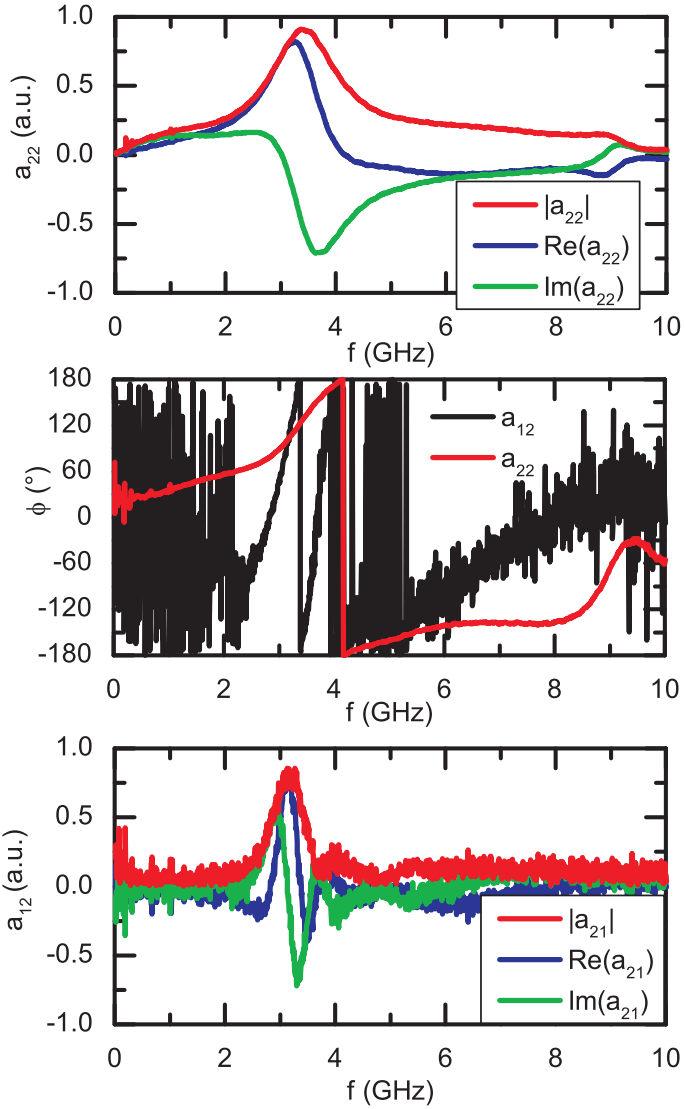

Figure 3.6: AESWS data obtained on a $t = 26$ nm Py plain film with $w_{\mathrm{IC}} = 2$ µm and $d = 12$ µm spin-wave transmission CPW at $\mu_0 H = 10$ mT and $\eta = 0°$. Data acquired in (a) reflection and (c) transmission is shown. In (b), phase in reflection and transmission is shown.

where d is the propagation distance. Measuring $\Phi(f)$ now allows probing the phase shift for all available k. This is a measure for the group velocity v_g, because

$$v_g = \frac{\partial \omega}{\partial k} = 2\pi \frac{\partial f}{\partial \tilde{\Phi}} s. \tag{3.21}$$

As here $s = 12$ µm, the resonance presented in Fig. 3.6 provides $v_g = 8$ km/s at the resonance frequency.

In Fig. 3.6 (c) we show the respective a_{12}, i.e. transmission data, namely $|a_{12}|$ (red), $\Re(a_{12})$ (blue), and $\Im(a_{12})$. Compared to a_{11} in Fig. 3.6 (c) we note the smaller signal-to-noise ratio: due to spatial decay as described in Eq. 2.38, $|a_{12}|/|a_{22}|(f_{\mathrm{res}}) = 0.018$, so the amplitude of a_{12} is notably smaller. Furthermore $\Re(a_{12})$ and $\Im(a_{12})$ exhibit oscillations not seen in $\Re(a_{22})$ and $\Im(a_{22})$. These oscillations are caused by the phase shift $\tilde{\Phi}$. Evaluation of v_g is strongly facilitated by considering e.g. two maxima of these oscillations, that are $\Delta\tilde{\Phi} = 2\pi$ apart and evaluate their frequency difference Δf. Then

$$v_g = 2\pi \frac{\Delta f}{\Delta \tilde{\Phi}} s = \Delta f s \tag{3.22}$$

holds true. For this dataset we obtain $v_g = 8.4$ km/s using this method. In contrast to the evaluation at a fixed frequency as introduced above, this method evaluates a mean v_g over a phase shift of 2π.

3.2 Brillouin Light Scattering

Brillouin light scattering (BLS) is an optical technique for mapping spin-waves in f and k space. The quasi-particles of spin waves, magnons, interact with coherent photons in an inelastic scattering process. The photon either loses energy by creating a magnon (so-called Stokes process) or gains energy from an annihilated magnon (anti-Stokes process). The frequency shift of the scattered photon, the so-called Brillouin shift is a measure of the frequency of the created or destroyed magnon. Measurements in this thesis have been performed at room temperature and are concerned with thermal magnons. Brillouin light scattering further allows measuring the wave vector of the magnon by varying the angle of the incident light with respect to the sample surface, thus varying the in-plane momentum transmitted in the scattering process. For a given wave length λ_L the transferred

wave vector k is

$$k = \frac{4\pi}{\lambda_L} \sin\theta, \tag{3.23}$$

where θ is the angle of the incident light. For further information on Brillouin light scattering of magnons, the reader is referred to [Dem01].

In this thesis, samples have been prepared for BLS experiments. Experiments have been performed by Dr. S. Tacchi and Dr. G. Gubbiotti at CNISM in Perugia, Italy in close collaboration with the author. The experimental setup used laser light of wave length $\lambda = 532$ nm and $P = 220$ mW power. The laser light was focused on the sample with an objective of focal ratio 2 and focal distance of 50 mm, resulting in a laser spot diameter of 30 μm. The scattered light is measured in a (3+3) tandem Fabry-Pérot interferometer to measure the Brillouin shift. The interferometer filters light of a given frequency, that is detected by a photomultiplier. By varying the pass frequency of the filter, scattered magnons of different frequency are detected. An external magnetic field $\mathbf{H}$ is applied in the sample plane. The incident angle of the laser beam is varied, in order to measure different wave vectors, so that the spin wave dispersion $f(k)$ can be measured for a given field $\mathbf{H}$. See [Erc97, Jor99, Gub02, Jor02, Wan02, Dem04, Bay05, Tse09, Tac10a, Tac10b] for examples of Brillouin light scattering studies on magnons.

3.3 Microfocused Brillouin Light Scattering

Microfocused BLS (μBLS) is a variation of BLS, first reported in [Dem04]. Here the the laser is focused on an as-small-as-possible spot on the sample. As in conventional BLS, Brillouin light scattering on magnons takes place, and the Brillouin shift is measured by an interferometer. The beam is moved on the sample, in order to measure the spatially dependent amplitude of scattered light for a given-frequency. In order to increase the signal-to-noise ratio, a CPW is integrated to the samples to apply microwaves at the desired frequency, in order to generate magnons. It is intended to selectively populate a magnon state more than thermal excitation would do. This enhances the BLS signal.

Samples also used for AESWS were studied using μBLS. The contact pads of CPWs were bonded to CPWs on printed circuit boards the connected to microwave cables and a microwave signal generator. Wire bond-

ing and experiments took place at CNISM in Perugia, Italy and were performed by Dr. M. Madami and Dr. G. Gubbiotti in close collaboration with the author. The experimental setup is described in [Gub09]. Here laser light with $\lambda = 532$ nm of power $P = 150$ mW was used, focused down to a spot of 235 nm diameter using a 100× dark field objective of numerical aperture 0.75. The setup was also used in combination with a CCD camera to visualize the sample and determine the position of relevant features. Note that in μBLS, the k sensitivity is lost in contrast to conventional BLS.

3.4 Magnetic X-ray Transmission Microscopy

Magnetic X-ray transmission microscopy (MTXM) is a microscopy technique that images magnetic states using the x-ray magnetic circular dichroism (XMCD) effect [Sch87]. The magnetic sample is irradiated with a circularly polarized X-ray beam. Electrons from core levels ($2p_{3/2}$) are excited to unoccupied d states above the Fermi level (L_3 edge) as partially polarized photoelectrons. Spin and orbital polarization can be calculated using Clebsch-Gordan coefficients [Fis98], considering the dipole selection rules for the transition. The transition probability depends on the magnetization of the atom, resulting in absorption coefficients varying with the magnetization. The resulting magnetic contrast of absorption is as follows[Fis96, Fis98]:

$$\frac{\Delta\mu}{\mu_i}(E) = \frac{\sigma_c}{\sigma_i}(E)(\hat{m}\cdot z)P_c, \tag{3.24}$$

where $\Delta\mu$ is the deviation from the polarization averaged absorption of the initial state μ_i, $\hat{m}$ is the normalized magnetic moment, $\hat{z}$ is the propagation direction of the X-ray photons with degree of polarization P_c. $\frac{\sigma_c}{\sigma_i}$ is the normalized magnetic absorption cross section. As the initial core level state is well defined, the method is element sensitive, i.e. the magnetization of e.g. Co and Fe can be studied separately.

We have performed MTXM measurements at the XM-1 microscope at the Lawrence Berkeley National Lab, Berkeley, CA, USA with support by Dr. P. Fischer and Dr. M.Y. Im. X-ray light is produced by the Advanced Light Source (ALS) synchrotron. The X-ray light is monochromatized and

focused by zone plate X-ray optics. 1000 pixel by 1000 pixel large images are recorded by a CCD camera, yielding a sample resolution of typically 25 nm. Samples with in-plane magnetization are tilted by 30° with respect to the beam so that $\hat{m} \cdot z$ is nonzero. Samples are prepared on 100 nm thick Si_3Ni_4 membrane substrates that provide low X-ray absorption with respect to the sample. External magnetic fields up to 100 mT are applied in the sample plane. Experiments are performed at room temperature. Recent results obtained on the XM-1 microscope with further details on the technique can be found in Refs. [Kas08, Mei07, Kim06, Im03, Hey07, Fis07].

4 Preparation

For the preparation of samples, two lithography methods have been employed, optical and electron beam lithography (EBL). Both methods are complementary, while optical lithography is fast and covers large areas, EBL provides much higher resolution. CPWs with $w_{\mathrm{IC}} \geq 2$ µm and Py mesas have been prepared using optical lithography, while smaller CPWs, nanowires, shallow-etched ADLs, and BCLs have been prepared using EBL.

4.1 Optical Lithography

CPWs with $w_{\mathrm{IC}} \geq 2$ µm and Py mesas that served as base for shallow-etched ADLs and BCLs have been prepared following these steps:

- Semi-insulating GaAs is used as a substrate[1]. We used undoped 2" wafers in [100] orientation. The specific resistance is $> 5 \cdot 10^7$ Ωcm at 22 °C. The thickness of the substrate is 350 µm. The substrate is cut into pieces usually 5 mm × 5 mm or 8 mm × 8 mm large using a diamond cutter. During cutting the substrate is covered by a protective resist layer. The substrate is cleaned using propan-2-ol and 2-propanone and dried using dry and clean Nitrogen.

- For MTXM measurements, Si_3N_4 membrane substrates[2] were used instead of GaAs. The membrane size was 3 mm × 3 mm × 100 nm. The frame size was 5 mm × 5 mm × 200 µm.

- A two-layer resist combination is spun onto the sample using spin coaters. First LOR-3A resist[3] is spun onto the substrate for 60 s at 4500 rpm. It is then baked for 60 s at 180 °C. Then S1813 G2

[1] Freiberger Compound Materials GmbH, Freiberg, Germany
[2] Silson Ltd, Blisworth, Northampton, United Kingdom
[3] MicroChem Corp., Newton, MA, USA

resist[1] is deposited on top by spin coating for 40 s at 6000 rpm. The sample is then baked out for 60 s at 115 °C. The two-layer resist combination is used to achieve an undercut that facilitates lift-off.

- Exposure is performed by an MJB-3[2] mask aligner. A chrome mask containing the desired structure is put in physical contact with the sample, and the sample is exposed for 4 s through the mask by ultraviolet light produced by a 350 W Hg lamp. The mask was written using a laser writer operated by the Walter-Schottky-Institut of TUM.
- The sample is developed using MF-26A developer[3] for 35 s. Exposed areas of the resist are solved.
- Metal is deposited onto sample. For Py mesas, Py is deposited using physical vapor deposition (PVD) by electron beam heating. For CPWs, 4.5 nm of Cr, 100 nm of Ag, and 22 nm of Au are deposited. Cr is used as adhesion layer, Au as oxidation preventing coating of Ag. The deposition is performed in high vacuum (10^{-7} mbar). A liquid nitrogen filled cooling trap is used to capture contanimation in the vacuum chamber.
- Lift-off processing of the metallic film on top of the resist is performed using remover 1165[4] containing N-Methyl-2-pyrrolidone as solving agent. The sample is left in remover 1165 for 60 min at 55 °C.

4.2 Electron Beam Lithography

EBL was performed for $w_{\mathrm{IC}} = 0.8$ µm CPWs, nanowires, BCLs and shallow-etched ADLs. The following steps were performed:

- GaAs substrate was cut and cleaned, as discussed above.
- Using optical lithography, Au markers were prepared for defining a coordinate system during EBL.

[1] Rohm and Haas Company, Philadelphia, PA, USA
[2] Süss MicroTec AG, Garching b. München, Germany
[3] Rohm and Haas Company, Philadelphia, PA, USA
[4] Rohm and Haas Company, Philadelphia, PA, USA

- For Py nanowires the substrate was spin-coated with a two-layer resist system for undercut: Poly(methyl 2-methylpropenoate) (PMMA) 50K[1] resist spun for 60 s at 6000 rpm, PMMA 950K for 60 s at 6000 rpm. Each layer was baked separately for 2 min at 160 °C.

- For CPWs a three-layer system allowing thicker deposition was used: Two layers PMMA 200K for 60 s at 4500 rpm and one layer PMMA 950K for 60 s at 4500 rpm. Each layer was baked separately for 5 min at 160 °C.

- For shallow-etched ADLs and BCLs, one layer of PMMA 600K was spun for 60 s at 6000 pm and baked for 4 min at 160 °C.

- Exposure was performed using an e_Line[2] EBL system.

- Py nanowires were defined by 200 nm wide exposure rectangles separated by 700 nm. Exposure was done using a 10 μm aperture and 30 kV voltage. The dose was 200 μC/cm^2. To compensate the proximity effect that causes lower effective doses at the edges of exposed areas, a 16 nm wide edge around each wire was exposed with 800 μC/cm^2.

- CPWs were exposed with 200 μC/cm^2. The aperture was 20 μm for conducting lines and 120 μm for contact pads.

- Shallow-etched ADLs and BCLs were exposed with 500-550 μC/cm^2 using the 20 μm aperture at 20 kV. Exposed dots had nominal diameter 100 nm to 150 nm.

- Development was performed using AR 600-56 developer[3] for 60 s followed by stopping using propan-2-ol for 30 s.

- For shallow-etched ADLs and BCLs, ion beam etching was used to etch 8 nm deep troughs into the developed areas. We used an ion beam extracted from inductively coupled Ar plasma. Typical process parameters for ion beam etching were: Ar gas flow was 10 sccm at the source and 5 sccm at the filamentless beam neturalizer (FBN)

[1] ALLRESIST GmbH, Strausberg, Deutschland
[2] Raith GmbH, Dortmund, Deutschland
[3] ALLRESIST GmbH, Strausberg, Deutschland

resulting in a $2{\cdot}10^{-4}$ mbar pressure during the etching process in the chamber. The applied RF power for the inductively coupled plasma was 109 W. The beam current was 55 mA with a grid voltage of 440 V. The accelerating current was 3.5 mA with a grid voltage of 188 V. The FBN discharge current was 55 mA at a voltage of 440 V. The resulting etching rate was 8 nm per 5 min. The beam was normal to the surface.

- For Py wires, 22 nm of Py was deposited using electron gun heated PVD. For CPWs, 5 nm Cr, 40 nm Ag, and 30 nm Au were deposited. For BCLs, 15 nm of Co was deposited in the same vacuum chamber as the ion beam.
- Lift-off is performed using remover 1165. In order to remove resputtered resist, shallow-etched ADLs and BCLs were put in an ultrasonic cleaning bath for up to 10 min.
- A 4 nm thick SiO_2-film was deposited using magnetron sputtering to provide electrical isolation between the magnetic film and the CPW. Alternatively 4 to 8 nm thick Al_2O_3 was deposited using atomic layer deposition.

4.3 Microscopic Composition of Nanowires, BCLs and Shallow-etched ADLs

In Fig. 4.1 we show a scanning electron micrograph of 360 nm wide nanowires with a $w_{\mathrm{IC}} = 0.8$ µm CPW prepared by EBL on top, resulting from the processing steps described above. The sample consists of about 360 nm wide Py wires with 890 nm period. The mesa consists of about 350 nominally identical wires. The shorted transmission CPW is shown in the upper micrograph. The propagation distance d amounts to 7.6 µm. Between the wires and the CPW an isolating SiO_2 layer is sandwiched (not resolved due to its transparency). This sample is discussed in detail in Chapter 5.

In Fig. 4.2 the preparation steps leading to a BCL sample are shown schematically (not to scale):

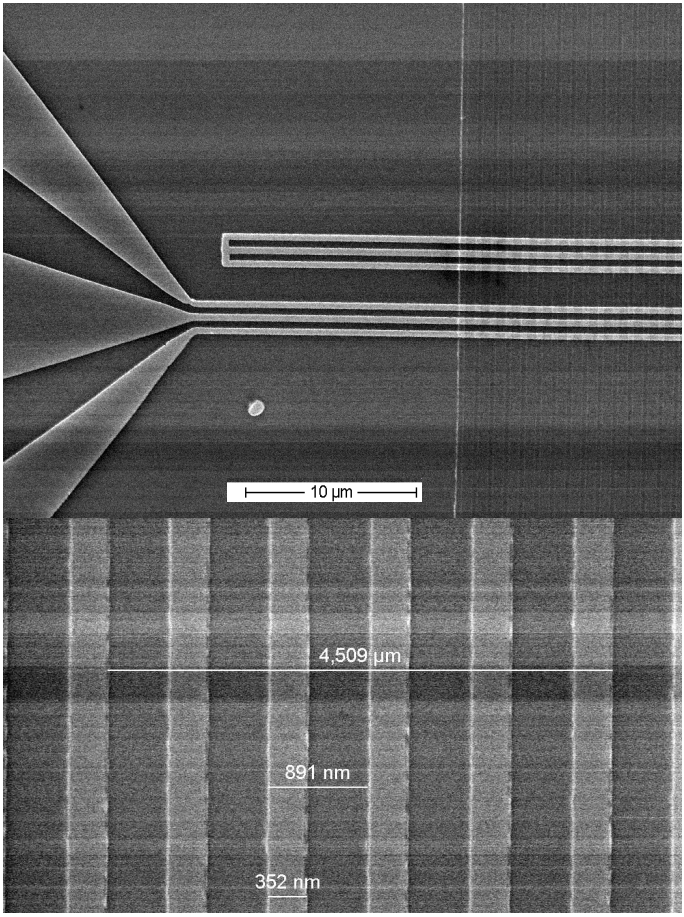

Figure 4.1: Scanning electron micrograph of nanowires with a width of about 360 nm. The period is 890 nm. The $w_{\mathrm{IC}} = 0.8$ µm wide CPW is prepared by EBL on top.

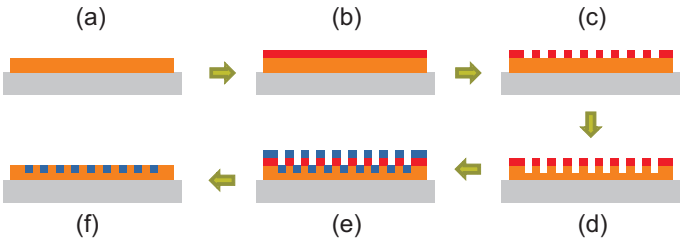

Figure 4.2: Schematic drawing (cross sections) of the BCL preparation process. (a) Py (orange) deposition on GaAs (gray), (b) PMMA (red) deposition, (c) EBL exposure and resist development, (d) Ar milling, (e) Co deposition, and (f) sample after lift off processing are shown.

- (a) Py (orange) is deposited onto the GaAs or SiN (gray) substrate.
- (b) PMMA resist (red) is spun onto the Py.
- (c) Using EBL a hole lattice is exposed and developed in the PMMA.
- (d) Using Ar milling, nanotroughs are etched into the Py.
- (e) Co is deposited onto the sample.
- (f) Lift-off processing is performed, i.e. the remaining PMMA and the Co on top of PMMA is removed.

Note that, apart from sample ALS-1 (see discussion in Chapter 6.3), steps (d) and (e) are performed in situ, i.e. without breaking the vacuum. Note also, that for shallow-etched ADLs, step (e) is left out. After the preparation of the BCL or shallow-etched ADL, SiO_2 or Al_2O_3 is deposited on top of the sample as an isolating layer. On top of this, the CPW is prepared.

In Fig. 4.3 we show a scanning electron microscopy image of a BCL acuired with an angle of 60° with respect to the sample plane. Here the application of ultrasonic vibration was not performed prior to the image acquisition. Tubular structures perpendicular to the sample surface arise during Ar milling of the sample. These tubes might consist of redeposited material and hardened resist. Ultrasonic agitation during lift-off processing allowed to remove the tubes after optimization of process parameters such as ion beam accelerator voltage, etching depth, molecular weight of

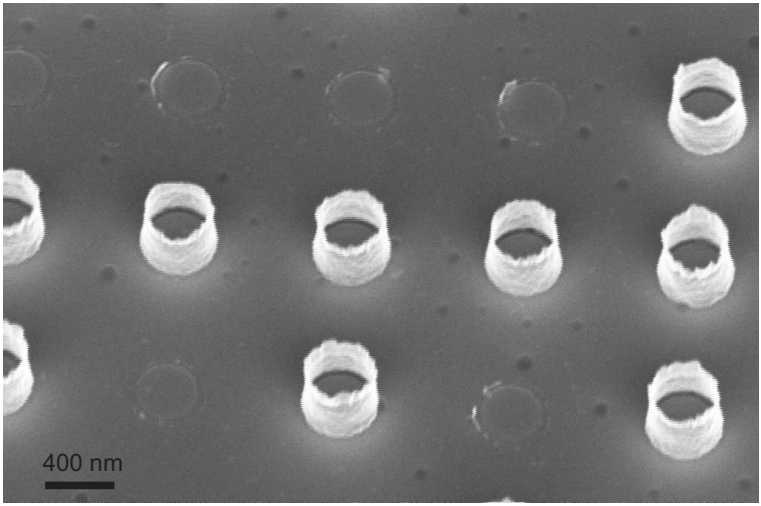

Figure 4.3: Scanning electron micrograph of a BCL acquired under an angle of 60° with respect to the sample plane after lift-off processing. The image was acquired prior to application of ultrasound. Remaining tubes of resist are seen.

resist, resist thickness, etching time, etching angle, and lift-off temperature. For samples used for MTXM measurements, the optimized process parameters were used to create BCLs. However, the tubes were not removed using ultrasound due to the fragility of the SiN membrane.

In Fig. 4.4 a schematical cross cut of a unit cell of a BCL is shown. This unit cell is repeated in-plane periodically in a square lattice with period p of 600 nm or 1000 nm. The thickness of the Py mesa t_{mesa} varies from 24 nm to 26 nm, the etching depth t_{etch} from 5 nm to 8 nm, the thickness of deposited Co from t_{dep} from 9 nm to 15 nm, and the diameter of the nanodisk from 310 nm to 370 nm. The specific parameters of BCLs and shallow-etched ADLs studied in this thesis are summarized in Table 6.1 in Chapter 6.2. Except t_{dep} all parameters also apply for shallow-etched ADLs. Further samples where Co nanodisks are deposited on top of unstructured Py and on GaAs without Py, as well as samples with further periods p and diameters d have also been produced but are not discussed in this thesis.

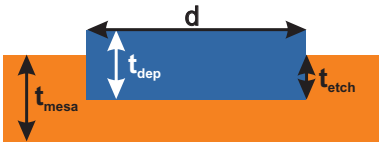

Figure 4.4: Cross cut (not to scale) of a single unit cell of a BCL. Py (orange) and Co (blue) are shown. Relevant geometrical parameters are defined in the text.

In Fig. 4.5 BCLs and shallow-etched ADLs are shown. White rings are attributed to remaining resist. In Fig. 4.5 (b) two CPW conductor lines in the left and the right part of the picture are resolved. Figure 3.2 in Chapter 3 shows a scanning-electron micrograph of a sample including the CPW on top. In Chapter 6 the dynamics of the BCLs and shallow-etched ADLs are discussed in detail.

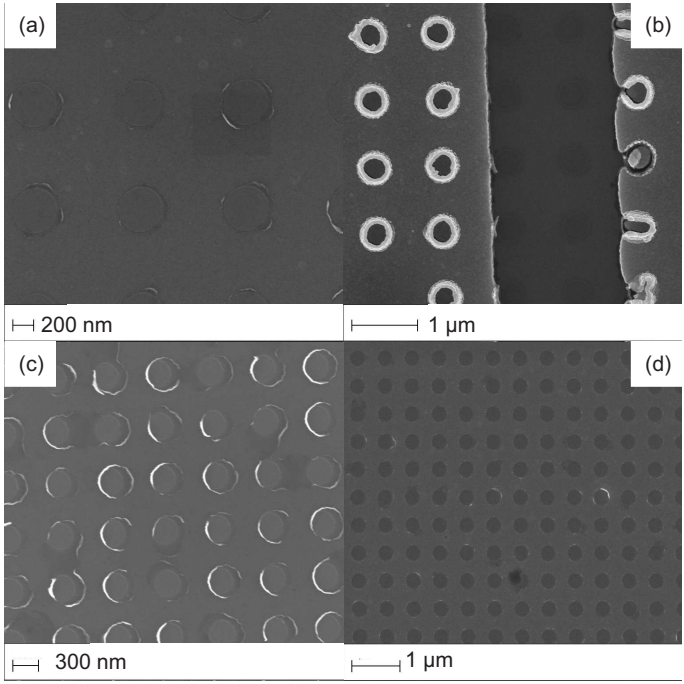

Figure 4.5: Scanning electron micrographs of (a) and (c) BCLs and (b) and (d) shallow-etched ADLs. The period in (a) and (b) [(c) and (d)] amounts to $p = 1000$ nm [$p = 600$ nm]. The light-gray areas in (b) are from the CPW integrated on top of this ADL. The metal of the CPW enhances the contrast for residual tube-like resist structures around etched nanotroughs.

5 Enhanced Transmission through Squeezed Modes in a Self-cladding Magnonic Waveguide

In this chapter we investigate spin-wave propagation in nanowires. Propagation of spin waves in microwires has found interest in resent studies due to the possible use as spin-wave bus or filter [Bay04, Dem08]. A finite amplitude at the wires' edges was found [Gus02] leading to increased magnon scattering due to imperfections in real samples. Consequently attenuation lengths are smaller than in comparable unstructured films [Dem08]. Here we report on spin waves propagating in 360 nm-wide Py nanowires configured in the zig-zag magnetic state by the application of a well-defined magnetic field history. The zig-zag state was recently reported by Topp et al. [Top08]. Here we present the first study on propagation in the zig-zag state, and find increased transmission of spin waves. In a combined study with micromagnetic simulations, we state that these spin waves propagate in two narrow channels defined by he zigzag-state. By varying the external field $\mathbf{H}$, we can furthermore change the group velocity v_g and thus create a velocity modulation transistor (VMT).

This chapter contains previously published work [Due12a, Due12b].

5.1 Experimental Results

In our study, arrays of permalloy wires were prepared as described in chapter 4. In this section we present data obtained on wires of width $w = 360$ nm and thickness $t = 25 \pm 2$ nm. The edge roughness was found to be $\rho = 10$ nm [root-mean-square (rms) value]. ρ was measured using scanning electron microscopy images of prepared samples, where ρ was

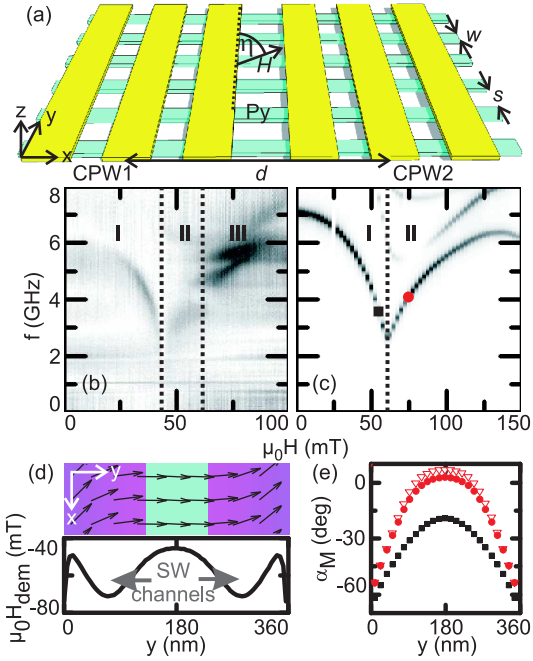

Figure 5.1: (a) Sketch of nanowires underneath two collinear CPWs introducing the relevant parameters. (b) Spectroscopy data $|a_{11}|$ taken at $\eta = 2^\circ$. The field-dependent black contrast displays spin wave resonances. (c) Eigenfrequencies extracted from micromagnetic simulations at $\eta = 2^\circ$ performed on ideal nanowires. Symbols mark where we evaluate α_M in (e). (d) Simulated zig-zag magnetic configuration (top) and demagnetization field H_dem (bottom) in the wire along the y direction for $\eta = 2^\circ$ at 75 mT. Fine arrows illustrate $M(x, y)$. Bright (dark) background color marks where $\alpha_\mathrm{M} > 0$ (< 0). (e) Angle α_M for $\eta = 2^\circ$ at 50 mT (black squares) and 75 mT (red circles) as well as $\eta = 3.5^\circ$ at 75 mT (red triangles) for comparison. Copyright (2012) American Physical Society [Due12b].

estimated from the observed roughness. In order to enhance the signal-to-noise ratio in our measurements, the mesa consisted of approx. 350 nominally identical wires that were prepared in parallel (Fig. 5.1). The total signal is thus the sum over all nominally identical wires. Wires were separated by $s = 540$ nm. We assume s to be sufficiently large in order to avoid direct dipolar magnetostatic and dynamic coupling between wires, following earlier studies, where similar values of s were sufficient to decouple wires, see [Top09]. For these samples a 4 nm thick SiO_2 sputtered isolation layer was used to isolate CPWs from the magnetic sample. CPWs with a $d = 7.6$ µm propagation distance between the signal lines and $w_{\mathrm{IC}} = 0.8$ µm signal line and gound line widths were used. The maximum excitation strength of the used CPWs was found to be $k_{\mathrm{CPW}} = 1.9$ 1/µm using a FFT of the current distribution (see chapter 3). The coordinate system was defined as follows [Fig. 5.1(a)]: The x-axis is parallel to the long axis of the wires (magnetic easy axis), the y-axis is perpendicular to the x-axis in the sample plain (hard axis), and the z-axis is perpendicular to the sample plane. The angle η of the external field $\mathbf{H}$ is defined with respect to the y-axis: $\eta = 0°$ for $\mathbf{H} \| y$. In simulations w and s were identical, however due to technical constrains, such as periodic boundary conditions and resolution of the simulation structure, wires were of infinite length, infinite number, and $\rho = 0$ was used in simulations.The saturation magnetization was $M_{sat} = 775 \ \frac{\mathrm{kA}}{\mathrm{m}}$. We have used one simulation layer. For $k = 0$ simulations, 8 by 192 square pixels in the $x-$ and y-directions were used with an edge length of 4.6875 nm per pixel. Along the x-axis (y-axis) the simulated structure was 37.5 nm (900 nm) long. In the y-direction we simulated the nanowires including the vaccum gap. For $k \neq 0$ simulations, we chose a length of 9.6 μm in x-direction in contrast to $k = 0$ simulations. See chapter 2.4.1 for further details on simulations. We introduce α_{M} as the angle between a microscopic magnetic moment in the nanowire and the $y-$axis.

In Fig. 5.1 (b) we show $|a_{11}|$ data obtained on the sample. Here the wires were presaturated at a field of $\mu_0 H = 100$ mT applied at $\eta = -90$ °, i.e. in negative x-direction. This means that $\mathbf{M}$ is aligned along the easy axis throughout the sample. Then the magnetic field was ramped down to zero and then up to a positive field value at $\eta = 2$ °, i.e. the x-component of the applied field H_{x} is now antiparallel to the previous saturation. Here dark color represents high absorption and thus high spin-precession amplitudes

in the sample. We compare eigenfrequencies in Fig. 5.1 (b) with a previous study in Ref. [Top08] and find similar phenomenological behavior concerning different regimes of eigenmode behavior. Further we remodel the behavior using micromagnetic simulations as shown in Fig. 5.1 (c). We note that in simulations significantly higher external fields H are needed in order to access the phenomenological behavior seen in measurements in Fig. 5.1 (b). Especially the boundary between regimes II and III as marked in the figure is shifted from approx. 60 mT to beyond 150 mT in the simulation. This is attributed to the edge roughness ρ, varying between simulations and experiment as described above. This behavior was already described by Topp et al. [Top08]. Reduced field values in the experiment were attributed to magnetization switching requiring much lower external field due to domain wall nucleation at the rough edges.

Following Ref. [Top08] we can subdivide the spectra into three distinct regimes, named regime I, II, and III: In regime I we find that the eigenfrequency $f(H)$ of the main mode decreases with H. This happens because the external field H counteracts the demagnetization field. At the switching point, the boundary between regimes I and II for an angle $\eta = 0°$ we would find a frequency minimum in an ideal sample. The boundary between regimes I and II is found at about 45 mT. The switching to regime III is found at the frequency gap of the experimental data, following [Top08]. At the boundary from regime I to regime II, magnetic moments in the center of the wire change their x-projection in order to align with H. The magnetic moments at the edges, however, still point in the negative x-direction. This is illustrated in Fig. 5.1 (d). We show values of α_{M} as calculated in micromagnetic simulations in Fig. 5.1 (e). In the wire's center, α_{M} is $2.7°$ $(6.7°)$ for $\eta = 2.0°$ $(3.5°)$ at 75 mT. Note that α_{M} is larger than η. This is the so-called zig-zag magnetic configuration state that was previously found in the study by Topp et al., Ref. [Top08]. However, propagation was not investigated there. Increasing the field further beyond the boundary between regime II and regime III, we find in micromagnetic simulations, that magnetic moments at the edges of the wires also switch directions, so that the x-projection of all magnetic moments is now along the external field. For high fields, all magnetic moments are aligned along $\mathbf{H}$.

It is now instructive to consider a_{21} data, i.e. data that was obtained

using the transmission characteristics of the CPWs. This will allow us to draw conclusions on the propagating behavior of spin waves in the sample. In Fig. 5.2 (a) we show the complementary $\Re(a_{21})$ to Fig. 5.1 (b). We now resolve the phase shift of the propagating spin wave for the case that the attenuation length

$$l_{\mathrm{a}} = v_{\mathrm{g}}\tau \tag{5.1}$$

is large enough to not damp the spin-wave too much over the propagation distance d (τ is the relaxation time). For large l_{a} if compared to d, we can resolve oscillating contrast at spin-wave resonance [Vla10], see chapter 3. In Fig. 5.2 (a), oscillations of $\Re(a_{21})$ (inset) are resolved in regime II. Note that this is the regime, where the zig-zag state is present. Oscillations are found between about 2.5 and 4 GHz (highlighted by the dashed circle). We define Δf in the inset of Fig. 5.2 (a), see chapter 3. In regimes I and III no oscillation contrast in $\Re(a_{21})$ and $\Im(a_{21})$ is resolved. We attribute this to a too high mode-specific damping of the spin-waves during the propagation path. Considering relative intensities $|\mathrm{a}_{21}|/|\mathrm{a}_{11}|$ measured at the same frequency of, e.g., 3.5 GHz, we find a signal in regime II which is increased by a factor of 2.5 relative to regime I, see marked data points in Fig. 5.3.

We have performed experiments for $\eta = 2°$, 3.5°, and 5° and found regime II for all three η. Note that in all experiments spin-wave propagation, i.e. oscillations in the real or imaginary part of transmission data, was found only in the zig-zag state, i.e. in regime II. As described in chapter 3, we extracted v_g from these contrast oscillations. In Fig. 5.2 (b) we show our findings for v_g. Error bars indicate the variation of v_{g} over evaluating different available datasets of nominally identical parameters. At $\eta = 2$ and 3.5 °, v_g decreases with increasing H. In a field regime of 6 mT, v_{g} varies from about 2.6 to 2.0 km/s at $\eta = 2$ °. For specific field values smaller than 45 mT at angles $\eta = 3.5$ and 5 ° regime II is found to exist for two angles, marked by the black arrow. In simulations, that as previously mentioned disregard the edge roughness ρ an even wider overlap of regime II for different angles is found. This is scaling with the width of regime II, that notably varies between experiment and simulation. We find that v_{g} varies with η by about 25 % for identical H in Fig. 5.2 (b). Considering Py plain films, we expect v_{g} to decrease with increasing H, see the calculated dispersion relation for this case in chapter 2 (notably Fig. 2.3). Between 40 mT and 55 mT, v_{g} decreases from about 3.5±0.5 $\frac{\mathrm{km}}{\mathrm{s}}$ to 3±0.5 $\frac{\mathrm{km}}{\mathrm{s}}$ at

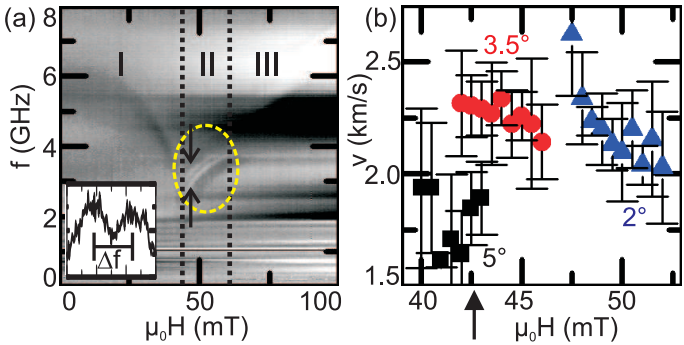

Figure 5.2: (a) Real part of signal S_{21} measured at $\eta = 2°$ between emitter and detector CPW. The alternating black-white-black-white contrast in the dashed circle is attributed to phase shifts provoked by spin-wave propagation in regime II. Horizontal black and white stripes are artifacts from the CPWs. Inset: Spectrum at 47.5 mT in the range from 2.8 to 3.4 GHz (indicated by arrows) showing an oscillating signal. Δf corresponds to a phase shift of 2π. (b) Propagation velocities at $\eta = 5°$ (squares), $\eta = 3.5°$ (circles), and $\eta = 2°$ (triangles). The arrow marks overlapping field regions (see text). Copyright (2012) American Physical Society [Due12b].

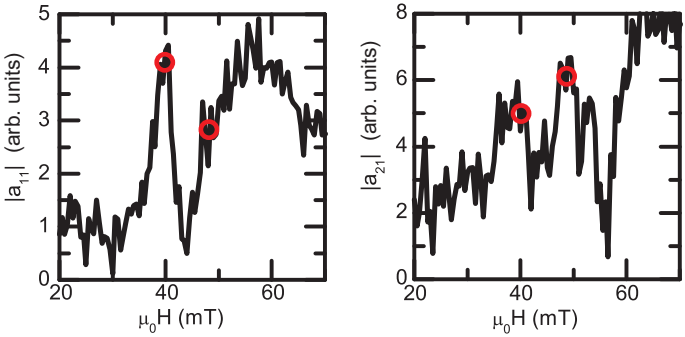

Figure 5.3: Comparison of reflection $|a_{11}|$ and transmission $|a_{21}|$ AESWS data obtained at a fixed frequency of $f = 3.5$ GHz.

$\eta = 0°$ in a plain film. This is a smaller relative change than in the studied nanowires. We state that v_g in the studied nanowires are similar to v_g in unstructured Py films.

5.2 Discussion

Finally we discuss the obtained results, considering simulated dispersion relations $f(k)$ obtained from micromagnetic simulations for $k \neq 0$ as described above. Notably we discuss the differences in spin-wave propagation between regimes I and II. We performed these simulations for 50 and 75 mT at $\eta = 2°$ in order to study magnetic states exhibiting similar eigenfrequencies, in regimes I and II, respectively. At 50 mT, i.e., in regime I, $v_g = 2\pi\partial f/\partial k$ is nearly zero in Fig. 5.4 (a). If we take into account Eq. 5.1, the attenuation length is expected to be very small as well. This motivates missing oscillating contrast in Fig. 5.2 (a) for regime I. For smaller H we find dispersion relations $f(k)$ (not shown) with small negative slopes, similar to the MSBVW mode (see chapter 2). In Fig. 5.4 (b) at 75 mT, i.e., in regime II, we find a positive slope $f(k)$ that exhibits $v_g = 2.1$ km/s. We further show time-resolved spatial out-of-plane magnetization plots in Fig. 5.4 (c) for 50 and 75 mT. Here we see that spin precession has propagated farther in regime II (75 mT) than in regime I for snapshots at identical time steps. Due to the extremely large phase velocity of spin waves exhibiting $f > 0$ at $k = 0$, we always find excitations throughout the wire even immediately after the beginning of the excitation pulse. Spin precession has propagated more than 2 μm in regime II after 1 ns (bottom-most graph). Areas of highest precession are squeezed into two channels that exhibit widths smaller than 100 nm while amplitudes are vanishingly small at the edges. In Ref. [Top08] it has been shown that the zig-zag state shows an inhomogeneous H_{dem}, with two local minima of the internal field. We show H_{dem} for $\eta = 2°$ and 75 mT in Fig. 5.1 (d). In each of these minima we find narrow nanochannels with spins nearly perpendicular to, both, the exciting field pulse and to the wires' edges. In these nanochannels, MSSW-like modes are excited. These spin waves have high v_g as we have found in $f(k)$ of Fig. 5.4 (b). Note that a nanowire of *geometrical* width of 70 nm would only show very slow MSSW-like spin waves of $v_g = 0.2$ km/s at 200 mT which is needed to overcome the demagnetization field. Here the

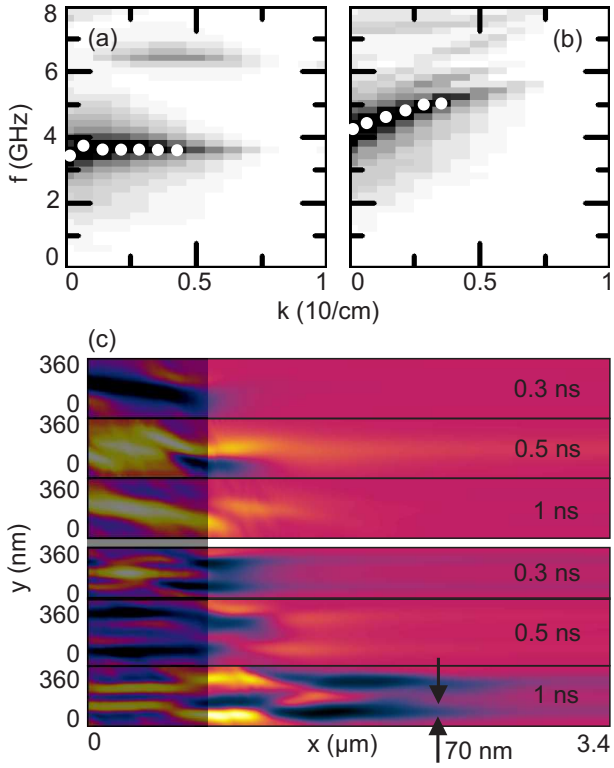

Figure 5.4: Dispersion relations $f(k)$ extracted from micromagnetic simulations for $\eta = 2\,^\circ$ at $\mu_0 H$ of (a) 50 (regime I) and (b) 75 mT (regime II). Dark color indicates a spin-wave resonance. White circles highlight maxima of the resonances. The broken line in (b) corresponds to $v_g = 2.1$ km/s. (c) Temporal evolution of the out-of-plane magnetization between 0.3 and 1 ns in regime I at $\mu_0 H = 50$ mT (three top rows) and in regime II at 75 mT (three bottom rows). Light (dark) color stands for negative (positive) spin-precession amplitude. The graphs have the same color coding. The field pulse h_{exc} excites a 800 nm wide area at the left end of the nanowire (gray area). Copyright (2012) American Physical Society [Due12a].

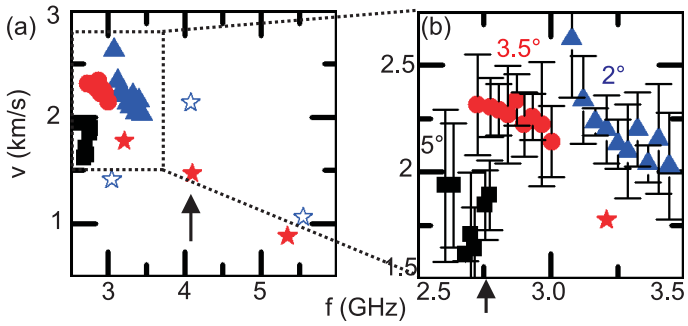

Figure 5.5: (a) and (b) Propagation velocities summarized as a function of frequency f. We intentionally replot the data from Fig. 5.2 (b) as a function of *frequency* f using the same symbols. Simulated data are for $\eta = 2^\circ$ (open star) and $\eta = 3.5^\circ$ (solid star). Arrows indicate where rotation of H varies the velocity v_g at the same f. Copyright (2012) American Physical Society [Due12b].

very narrow nanochannels with confinement of propagation to the interior of the wire are a self-cladding effect for spin waves. In contrast to photonics, we can switch this effect on and off using the magnetic field, i.e. varying between regimes I and II. In Fig. 5.5 (a) we show group velocities obtained in regime II using the $k \neq 0$ simulations and evaluating the slope of the dispersion (stars). Due to the differences in switching fields between experiment and simulation, the covered field regime is different. Simulated v_g are small for high f and, overall, increase with decreasing f. For low f, simulated values of v_g are found to be similar to experimental ones, neglecting differences in H. Experiment as well as simulation show that regime II can support spin-wave propagation at identical f but different v_g upon varying η [see arrows in Fig. 5.5 (a) and (b)].

In conclusion we find that a similar concept to velocity modulating transistors may be implemented using spin waves. Using $\Delta v_g / \Delta \eta$ as a figure-of-merit, we find 0.4 km/(s·deg) and 0.3 km/(s·deg) from the simulations and experiments data, respectively, in Fig. 5.5. The presented spin-wave propagation in the zig-zag state provides new possibilities for nano-optics with spin waves on the sub-100-nm length scale.

6 Magnetization Reversal, Mode Localization and Magnonic Band Gaps in Binary Component Lattices

Periodic binary component lattices (BCLs) are an approach towards magnonic crystals, first proposed by Vasseur et al. [Vas96]. BCLs are characterized by the periodic inclusion of one magnetic material into another. Studies on one-dimensional bicomponent lattices exhibiting allowed magnonic bands and forbidden band gaps have recently been published in Ref. [Wan10]. In our study we have performed a thorough experimental and theoretical investigation on two-dimensional BCLs in that we have evaluated the static and dynamic magnetization using MTXM, micromagnetic simulations, BLS, μBLS, AESWS, and PWM. Before BCLs are presented, it is instructive to review shortly relevant properties of ADLs where a periodic array of holes was etched in the ferromagnetic thin film. Such devices have been investigated for more than a decade [Tor98, Yu03]. The microscopic understanding of the modes has been developed in recent years. A thorough discussion can be found in Ref. [Neu11a].

6.1 Introduction: Permalloy Films with a Periodic Array of Holes

In Fig. 6.1, spin-wave profiles obtained at $\mu_0 H = 20$ mT on a $p = 800$ nm etched-through ADL are reported from [Neu10]. Here a fundamental mode that extends between holes throughout the lattice was found. The images were obtained from micromagnetic simulations. At $\eta = 22°$,

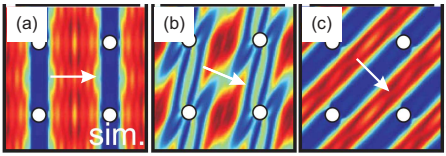

Figure 6.1: Spatial spin-wave mode profiles are obtained at $\mu_0 H = 20$ mT and, in particular, $k = 0$. The eigenfrequencies are (a) 3.8, (b) 4.3, and (c) 3.9 GHz. Red (blue) contrast reflects high (low) spin-precession amplitude. The white arrows indicate the field orientation. The period of holes is $p = 800$ nm. The diameter of holes is $d = 120$ nm. Taken from [Neu10]. Copyright (2012) by the American Physical Society.

i.e. Fig. 6.1 (b), no mode extending throughout the lattice is found, spin precession is strongly localized mainly between holes. We expected this to change in BCLs due to the now continuous nature of the material.

In Fig. 6.2 (a) a dispersion relation obtained on the $p = 800$ nm ADL is compared to an unpatterned film [Neu11b]. In the dispersion as calculated by micromagnetic simulations (gray-scale plot) one dispersive mode (dark color) is seen. Circles represent experimental data. While the mode is modeled well by the long-dashed line, obtained by assuming a reduced saturation magnetization due to the air holes, it is not modeled well by the dash-dotted and dotted lines obtained from a nanowire model with perpendicularly quantized modes. Using the plane wave method it was shown that the fundamental mode undergoes avoided crossings with higher order modes (shown in Fig. 6.2 (b), (c), (d) at $k = 0$) where such modes (dotted) coincide with the frequency of the fundamental mode. Refilling holes with magnetic material is expected to change such characteristics, as well.

The following sections contain previously published work from Refs. [Due11, Tac12b].

6.2 Overview of Studied Binary Component Lattices

We have studied BCLs composed of Co inclusions in a Py matrix and Py inclusions in a CoFeB matrix. BCLs reported here consist of circular in-

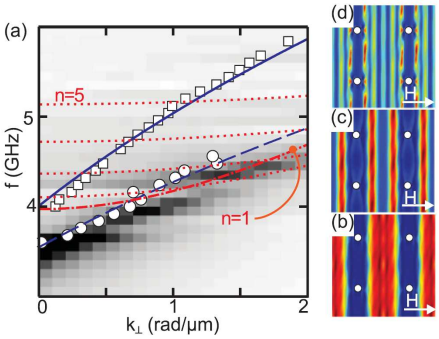

Figure 6.2: (a) Measured and calculated SW dispersions for a plain film and an ADL at $\mu_0 H = 20$ mT and $\eta = 0^\circ$. Open squares mark the magneto-optical Kerr effect (MOKE) data obtained on a plain film, see Ref. [Neu06b] for details on the MOKE technique. The solid line reflects the calculated dispersion assuming $M_{\mathrm{sat}} = 770$ kA/m. Open circles mark the MOKE data measured on the ADL. The long-dashed line is a SW dispersion calculated for a film assuming a reduced saturation magnetization $M^{\star}_{\mathrm{sat}} = 600$ kA/m. This remodels the measured dispersion far better than previously discussed nanowire SW dispersions: the dotted and dashed-dotted lines represent calculated dispersions obtained from a model assuming $M_{\mathrm{sat}} = 770$ kA/m and quantized wave vectors $k_{\|} = n\pi/w_{\mathrm{eff}}$ with $w_{\mathrm{eff}} = 600$ nm. The gray-scale plot is the SW dispersion as obtained from wave-vector-resolved micromagnetic simulations. Dark (bright) corresponds to large (small) SW amplitude. Spatial spin-wave profiles as obtained from micromagnetic simulations at $k = 0$ are shown for (b) $f = 3.7$ GHz ($n = 1$), (c) $f = 4.2$ GHz ($n = 2$), and (d) $f = 4.4$ GHz ($n = 3$). Dark (bright) colors correspond to small (large) spin-precession amplitude. The direction of H is indicated. Taken from [Neu11b] Copyright (2011) by the American Physical Society.

Name	p	d	t_{mesa}	t_{etch}	t_{dep}	Comments
ALS-1	1 µm	370 nm	24 nm	5 nm	15 nm	Py(Co), ox.
ALS-8	1 µm	370 nm*	24 nm	5 nm	15 nm	Py(Co)
ALS-9	1 µm	370 nm	24 nm	5 nm	15 nm	Py(Co)
118-4-2	1 µm	435 nm	26 nm	7 nm	15 nm	Py(Co)
118-6-3	1 µm	435 nm	26 nm	7 nm	N/A	Py(air)
138-B1-1	600 nm	310 nm	24 nm	8 nm	N/A	Py(air)
138-B2-4	N/A	N/A	24 nm	N/A	N/A	Py film
138-B2-4	600 nm	310 nm	24 nm	8 nm	15 nm	Py(Co)
140-3-1	600 nm	310 nm	8 nm	8 nm	9 nm	Py(air)
140-4-6	600 nm	310 nm	8 nm	8 nm	N/A	Py(air)
CoFeB-2-B	600 nm	310 nm	24 nm	8 nm	15 nm	CoFeB(Py)
CoFeB-2-C	N/A	N/A	24 nm	N/A	N/A	CoFeB film

Table 6.1: Overview of studied samples. Ox. in comments section stands for oxidation process of the relevant interface. ALS samples have been prepared on SiN substrates. *Note that ALS-8 has elliptically shaped Co dots. This is further discussed in the text.

clusions of diameter d in a square lattice of period p. The matrix consists of a mesa of thickness t_{mesa}. The etching depth for inclusions is t_{etch} while the thickness of the deposited inclusion is t_{dep} (see chapter 4 for further details). In table 6.1 we list studied samples and their parameters. Samples called ALS have been used for MTXM studies. All other samples have been used for AESWS, BLS, or µBLS studies. Due to the specific experimental conditions, for MTXM separate samples needed to be prepared.

In Fig. 6.3 we show micrographs of $p = 1000$ nm BCLs (a) 118-4-2 on GaAs using SEM imaging, (b) ALS-1, (c) ALS-8, and (d) ALS-9 on SiN membranes using MTXM on the Co edge (see the following section for a discussion of the contrast in MTXM images). In the SEM image in Fig. 6.3 (a) we show a Co dot in Py matrix. The circular Co dot has a diameter of $d = 435$ nm. In 6.3 (b) the circular Co dot of 370 nm diameter is marked by a black dotted circle. The structure extending to the right is a projection of the top of remaining resist tubes after sample processing. These tubes are only seen in samples on SiN membranes. For GaAs samples, the tubes have been removed by ultrasonic excitation. This was not possible with

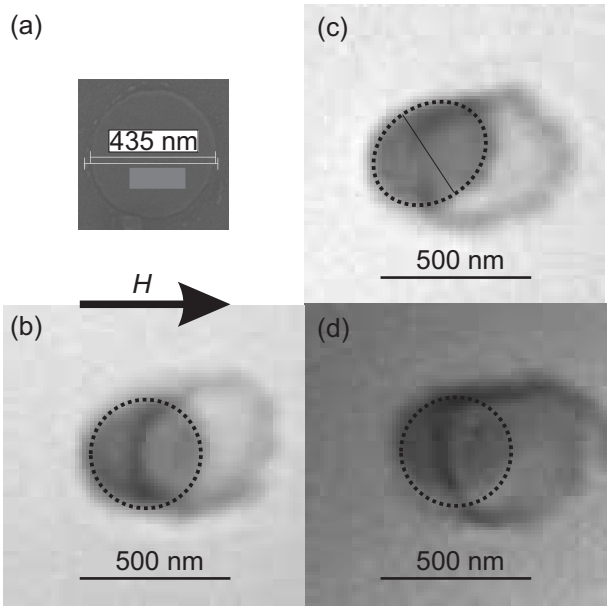

Figure 6.3: Micrographs of $p = 1000$ nm BCLs (a) 118-4-2 on GaAs using SEM imaging, (b) ALS-1, (c) ALS-8, and (d) ALS-9 on SiN membranes using MTXM on the Co edge.

SiN samples due to their fragility. In Fig. 6.3 (c) we show an MTXM image of sample ALS8. The Co dot is elliptical[1]. The long (short) axis is 400 nm (310 nm). The long axis of the dot is rotated to the lattice constant (parallel to the external field indicated by the white arrow) by 15 to 20°. Sample ALS-9 shown in Fig. 6.3 (d) exhibits identical diameter of the Co nanodisk compared to sample ALS-1, i.e. $d = 370$ nm.

[1] In Ref. [Mam12] it was shown that elliptical BCLs present a promising concept for further magnonic crystal studies

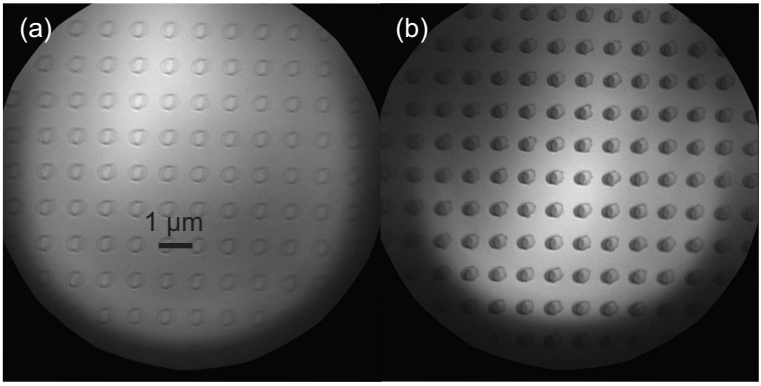

Figure 6.4: Raw CCD image of sample ALS-1 obtained by MTXM. The photon energy was tuned to the (a) Fe, (b) Co absorption edge.

6.3 Magnetic Transmission X-ray Microscopy Study

Static magnetization and magnetization reversal processes of BCLs have been studied using MTXM (see chapter 3). Samples have been prepared especially for MTXM purposes (see chapter 4). In total three samples have been studied, cf. table 6.1. Sample ALS-1 had been left in air for approximately twelve hours after Ar milling of nanothroughs and prior to Co deposition, whereas samples ALS-8 and ALS-9 have been prepared in situ and with nominally identical parameters. As a consequence, the interface between the matrix material and the inclusions was different compared to ALS-1. It was expected that the oxidized interface might suppress possible exchange coupling assumed to be relevant for the in-situ prepared BCLs.

Data obtained by the measurement setup consists of raw CCD information (see chapter 3). Pixel brightness is proportional to the number of photons counted per pixel. Raw data pictures show the total X-ray absorption for the relevant photon energy. In Fig. 6.4 raw CCD images of sample ALS-1 are shown. The photon energy of the X-ray beam was tuned to the absorption edge for (a) Fe and (b) Co. The Fe edge was chosen to study the magnetic behavior of Py. In 6.4 (b) the stronger X-ray absorption by

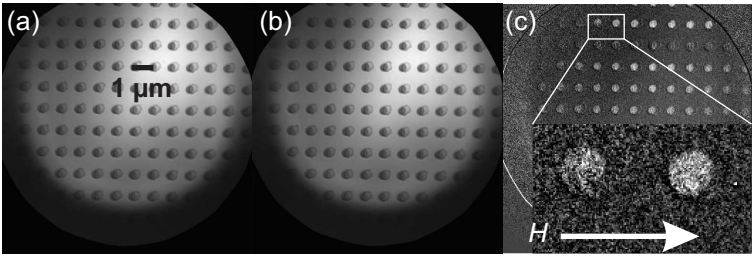

Figure 6.5: Illustration of MTXM image processing. Raw CCD images of sample ALS-1 acquired at an external field of (a) 4.8 mT and (b) 7.2 mT applied from left to right. (c) Picture (b) divided pixel-wise by picture (a). The inset of (c) shows a partially switched Co nanodisk (left). The field direction is indicated.

the embedded Co disks is seen. Disks therefore appear as dark spots. In 6.4 (a) the positions of nanodisks appear as bright areas compared to the surrounding matrix as weaker absorption is active due to the smaller thickness of Py in the etched areas. Furthermore in Fig. 6.4 (b) dark rings are resolved. These rings are projections of the top of remaining resist tubes after sample processing (see chapter 4). Note that these rings are shifted with respect to the disks. This shift is caused by the tilting of the sample with respect to the X-ray beam by 30°. To study the field-dependent change in magnetization, processed data will be shown in the following sections, where images obtained at a given external field H will be divided pixel-wise by images obtained at the preceding field step.

6.3.1 Data Obtained on a BCL with Oxidized Interface

In this subsection data obtained on sample ALS-1 are shown. During the production of this sample, the sample had been left in air between Ar milling and Co deposition. This was done to oxidize the interface. All other production steps and parameters had been identical to the other samples. In Fig. 6.5 we show raw images of sample ALS-1 acquired at (a) $\mu_0 H = 4.8$ mT and (b) 7.2 mT. Prior to the data acquisition, the BCL was saturated at -36 mT. In (c) we show (b) divided pixel-wise by (a), thus the contrast with respect to the background. In such data bright color represents the change in magnetization projected onto the field direction when changing the field from 7.2 mT to 4.8 mT. Due to drift of the sample, im-

ages are aligned in post processing, until the remaining contrast produced by the topography of the sample vanishes. In Fig. 6.5 (c) Co disks that have not yet changed magnetization in this field step show the same dark grey contrast as the background, however due to sub-pixel drift, they can still be recognized by their borders. Co dots that have switched can be recognized by their clear bright contrast. This applies to rows 1, 2, 4, 5, and 6 in the image. Nanodisks in row 3 have switched partially.

Images acquired at the Co and at the Fe edge at the same fields steps are now compared in order to study if magnetization reversal processes of Co and $Ni_{80}Fe_{20}$ are coupled in sample ALS-1. In Fig. 6.6 we show images acquired at a corner of the mesa. The mesa's edge is e.g. seen in Fig. 6.6 (c) as a border parallel to the upper and left edges of the image. The sample has been saturated using a magnetic field of $\mu_0 H = -36$ mT. Then the field was ramped down to 0. Afterwards the field was ramped to $\mu_0 H = +36$ mT in steps of 0.6 mT. For every field step, the data acquired at a given field is divided pixel-wise by the data acquired at the previous field, as described above. This allows imaging the switching processes in the sample field step by field step. Switching corresponds to bright colors. In Fig. 6.6, the left (right) column shows data acquired on the Fe (Co) edge. Note that the data was acquired in two different measurement field sweeps, one for each X-ray photon energy. Images are shown for pixel-wise divided pairs 3.6 mT/3.0 mT in (a) and (b), 4.2 mT/3.6 mT in (c) and (d), 4.8 mT/4.2 mT in (e) and (f), and 5.4 mT/4.8 mT in (g) and (h). The images shown are the only pixel-wise divided field pairs where a change in contrast was resolved. In (a) and (b) contrast changes in a diagonal line at the corner of the mesa in Py indicate a change in magnetization in this material. Co does not change. In (c) and (d), changing the field from 3.6 mT to 4.2 mT large areas of Py switch, notably leaving stripes parallel to H beneath and between Co dots parallel to the field in the remanent position. Co does not show changes in magnetization in (d). In the Fe image (c) the border of the mesa can clearly be seen as the border of dark contrast in the uppermost area of the image. When increasing H from 4.2 mT to 4.8 mT in image (e) only a small Py area of the sample changes magnetization, whereas in image (f) a large number of Co disks switches. Some dots switch only partially with domains extending parallel to the field direction (left-right). These domains switch in the last field step from 4.8 mT to 5.4 mT in images (g) and (h). In image (g) a change in Fe magnetization

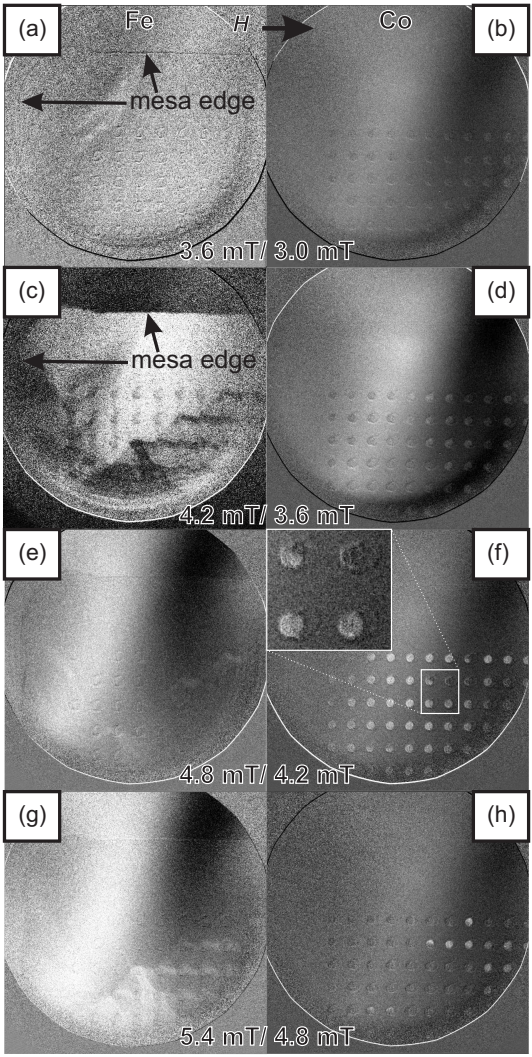

Figure 6.6: Pixel-wise divided MTXM images acquired on sample ALS 1 at the (a), (c), (e), (g) Fe edge and (b), (d), (f), and (h) Co edge for field pairs (a), (b) 3.6 mT/3.0 mT, (c), (d) 4.2 mT/3.6 mT, (e), (f) 4.8 mT/4.2 mT, and (g), (h) 5.4 mT/4.8 mT.

is observed in the middle of the bottom half of the picture, and notably in areas beneath and between Co disks parallel to H, thus in areas that did not switch in (c).
From the presented data set, we conclude that Py undergoes reversal processes from 3.0 mT to 5.4 mT, Co switches between 4.2 mT and 5.4 mT. Py switches in some parts of the studied area of the mesa completely, in other parts at higher fields in stripes parallel to H under and between Co disks. As can be seen in images (e) through (h) the switching processes do not seem to be correlated, as they occur in different sample areas. However it is important to note that data in the two columns of Fig. 6.6 representing Fe and Co have been taken during subsequent field sweeps. Thus Co nanodisks and remaining Py stripes reverse within a field regime of 0.6 mT.

In order to study sample ALS-1 in more detail, we repeat the analysis in 0.6 mT field steps at another position on the same mesa. In Fig. 6.7 we show MTXM data acquired in a position distant from the mesa's border. Data acquired for Py at the Fe edge is shown in Fig. 6.7 (a) through (d). Images are pixel-wise divided and acquired at the field pairs (a) 3 mT/2.4 mT, (b) 3.6 mT/3 mT, (c) 4.2 mT/3.6 mT, and (d) 4.8 mT/4.2 mT. As the beam focus is in the upper right corner of the pictures, magnetic contrast is more difficult to judge compared to the previous set of images due to strong variations in sample illumination throughout the images. Highest illumination and as a consequence highest magnetic contrast occurs in the areas marked by the white dashed circles. Four successive switching processes take place between from 3 mT to 4.8 mT. First the area (i) left of the diagonal line and in the circle marking the area of highest contrast switch (a), marked by bright contrast. The bright contrast is not seen under the Co dots and under Co dots and between Co dots parallel to the external field. Then area (ii) between the two dashed diagonal lines in the circle switches, and remaining parts of area (i) in (b). In Fig. 6.7 (c) areas right to the diagonal line switch. In (d) diagonal stripes throughout the field of view switch, indicated by the diagonal dashed line, as well as the lowermost area (iv). We conclude that in the inner part of the Py mesa between 3 mT to 4.8 mT large domains are nucleated in the reversal process. In Fig. 6.7 (e) and (f), images acquired at the Co edge are shown. The respective fields are 4.2 mT and 3.6 mT. In Fig. 6.7 (e) and (f) we make use of different polarization in order to judge the magnetic behavior throughout the whole field of view. Areas of highest magnetic contrast are marked

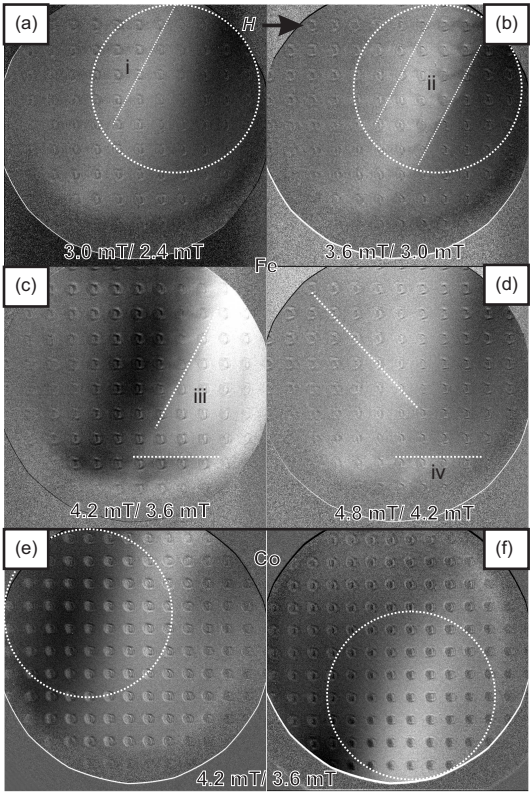

Figure 6.7: Pixel-wise divided MTXM images of sample ALS-1 acquired on the (a), (b), (c), and (d) Fe edge and on the (e), (f) Co edge. Magnetic fields used for image division have been (a) 3 mT/2.4 mT, (b) 3.6 mT/3 mT, (c) 4.2 mT/3.6 mT, (d) 4.8 mT/4.2 mT, (e) and (f) show the difference images for the same fields 4.2 mT/3.6 mT but for different polarizations of the X-ray beam. Images (a) through (e) use polarization by blocking the lower half of the beam, image (f) the upper half.

by dashed circles. The magnetic field values correspond to the Fe image in Fig. 6.7 (c). Considering data in Figs. 6.7 (e) and (f) we conclude that all Co disks switch, denoted by bright [dark] contrast in (e) [(f)]. This is in contrast to switching via several domains as we have observed for Py on the Fe edge. In the inner part of the mesa Co nanodisks are thus found to switch at about 4.2 mT. At the border switching was observed also at a higher field of 5.4 mT. As a consequence, for fields larger than 5.4 mT all Co nanodisks are expected to be reversed.

We now compare findings obtained on both studied areas of the mesa. In both areas we have observed that Py switches via domains. Directly under the Co dots and in areas that link Co dots parallel to the external field, Py switches after an additional field step. Co switches in two steps in the first studied area, but homogeneously in the second studied area. Possibly this due to the mesa edge of the first studied area. Furthermore Co switches between 4.2 mT and 5.4 mT in the first studied area, but between 3.6 mT and 4.2 mT in the second studied area. In the first studied area Co switches in clusters that do not correspond to the Py switching domains. In the second studied area, Co switches at once, whereas Py switches in domains. We do not find a direct correlation between Co and Py in the reversal process.

To operate such BCLs as magnonic crystals in the nearly saturated state it is therefore important to apply $\mu_0 H \geq 5.5$ mT. It is decisive to know the lower field limit as studies on thin-film devices show spin-waves with large group velocities v_g at small fields. Often v_g decreases with increasing H.

6.3.2 Data Obtained on Samples with In Situ Prepared Interfaces

It is now interesting to study the magnetization switching of samples that have been prepared without breaking the vacuum between Ar milling of $Ni_{80}Fe_{20}$ and deposition of Co into etched nanotroughs. We have studied samples ALS-8 and ALS-9. We have performed similar MTXM measurements compared to ALS-1.

In Fig. 6.8 we show data obtained on sample ALS-9. In the left (right) column we show data with lower (upper) half of the beam blocked. As the columns thus differ in their polarization, a change in magnetization

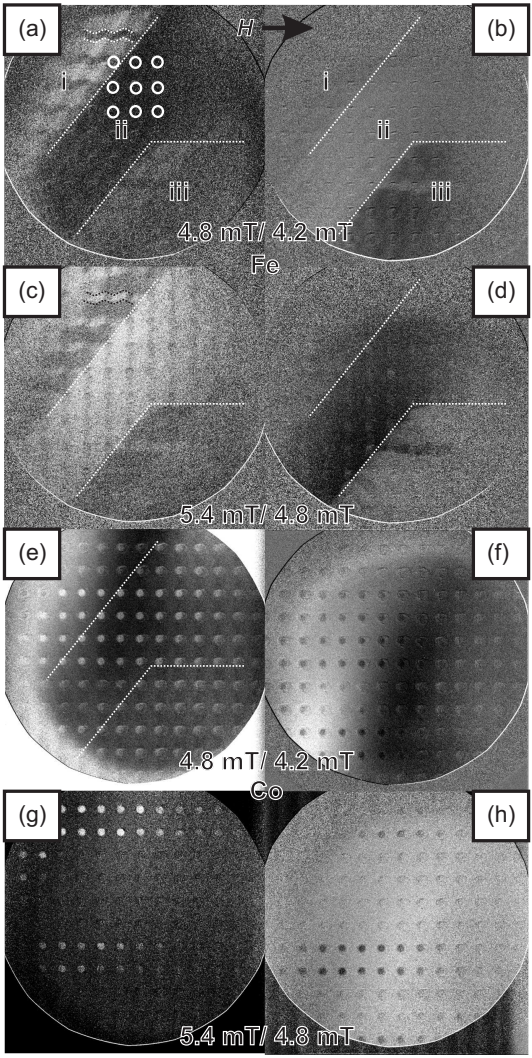

Figure 6.8: Pixel-wise divided MTXM images of sample ALS-9 acquired on the (a), (b), (c), and (d) Fe edge and on the (e), (f), (g), and (h) Co edge. Magnetic fields used for image division have been (a), (b), (e), (f) 4.8 mT/4.2 mT, (c), (d), (g), (h) 5.4 mT/4.8 mT. Images in the left (right) column use different polarization by blocking the lower (upper) half of the beam.

leads to an opposite change in contrast. In the left (right) column change in magnetization is indicated by bright (dark) contrast. Both polarizations provide complementary information and have opposite areas of optimal contrast. Images (a) through (d) [(e) through (h)] show data acquired on the Fe [Co] edge. (a), (b) and (e), (f) have been acquired at 4.8 mT/4.2 mT. Magnetization switching takes place in areas marked (i) and (iii), marked by bright color. Note that under Co dots and between Co dots along lines parallel to the field no bright color is seen (enclosed by the zig-zag shaped lines in the uppermost instance). In (c) and (d) these zig-zag shaped areas, as well as area (ii) switch when increasing the field to 5.4 /4.8 mT. Furthermore top-to-bottom black lines in (c) and corresponding white lines in (d) indicate a smaller change in magnetization in areas under Co dots and in lines perpendicular to the external field. This is different compared to ALS-1. A further change in magnetization is not resolved in higher field steps (data not shown). We now turn our attention to data obtained at the Co edge at the same fields. In images (e) and (f) [(g) and (h)] we likewise show data obtained at 4.8 mT/4.2 mT [5.4 mT/4.8 mT]. We conclude from these images that Co dots switch in two clusters, first in the middle of the visible area, then in the upper and lower part. If compared to Fe, it is notable, that these clusters cover stripe-like regions in parallel to the external field (left-to-right), but not in a diagonal direction. We conclude that in ALS-9, Py and Co switch at identical fields but in separate areas. In Fe a characteristic difference arises between zigzag-shaped areas under and between Co dots along the external field and the remaining material. Material under and between Co switches at larger fields.

Two findings are interesting: Py in ALS-9 reverses at a larger field compared to ALS-1, i.e. 4.8 mT compared to 3.2 mT, respectively. Py is magnetically harder in ALS-9. Still, the BCL has become (nearly) saturated already at 5.4 mT, i.e., at the same field as ALS-1.

It is now interesting to study a further sample, sample ALS-8. Note that the Co dots were found to be elliptical (see above). In Fig. 6.9 we show images of sample ALS-8 acquired on the Fe (Co) edge in the left (right) column. In images (a) and (c), a change of contrast in a diagonal domain in the middle of the picture can be seen when increasing the external field from 4.2 mT to 4.8 mT. Here the magnetization changes in the Py without stripes under and between the etched areas parallel to the external field (marked by zig-zag shaped lines) in the area marked (ii). When increasing the field to 5.4 mT such a reversal takes place in further sample areas (Fig.

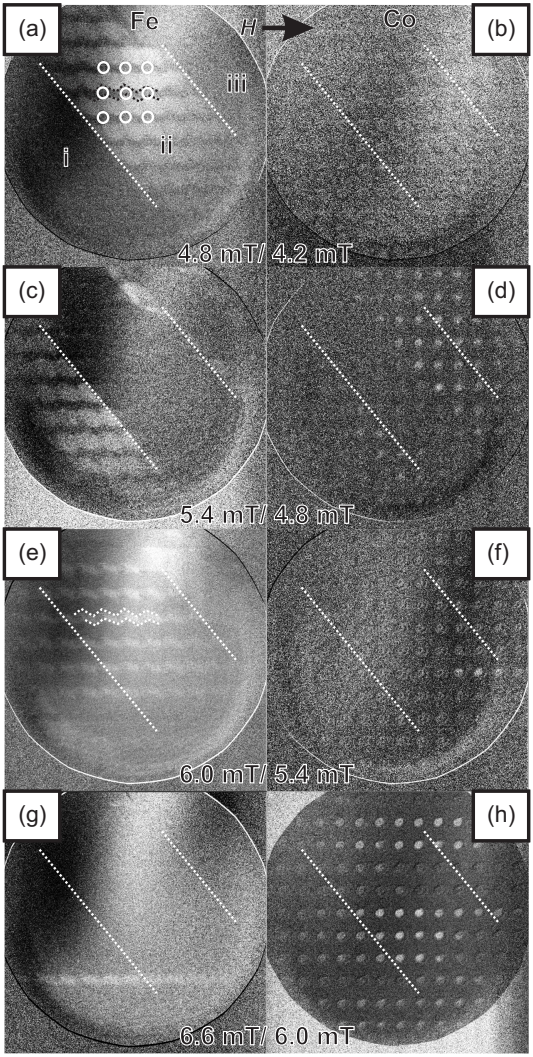

Figure 6.9: Pixel-wise divided MTXM images acquired on sample ALS-8. External field strengths are indicated in the pictures. Circles indicate the lattice of Co dots which have an elliptical shape in this sample. Diagonal dashed lines in all images indicate the border between areas i, ii, and iii defined in (a). Zig-zag-shaped lines in (a) and (e) separate exemplary areas that change magnetization in (a) and (e).

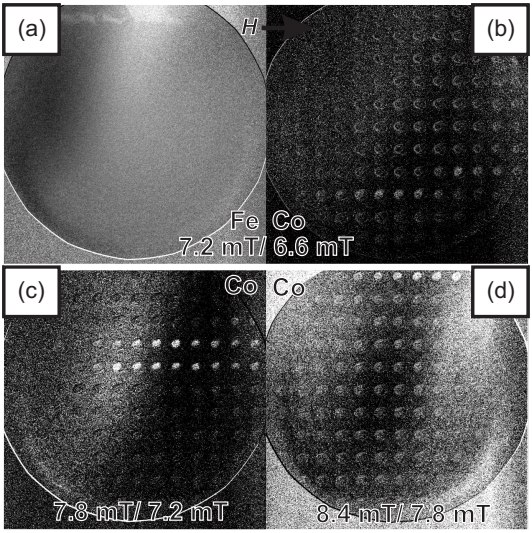

Figure 6.10: Pixel-wise divided MTXM images acquired on sample ALS-8. External field strengths are indicated in the pictures.

6.9 (c)) (i) and (iii). In images (e) and (g) the field is increased to 6.0 mT and 6.6 mT. Here the zig-zag shaped areas that have shown no magnetization reversal processes in in images (a) and (c) switch. Interestingly the zig-zag shaped stripes transcend the boundaries of areas (i), (ii), and (iii), that delimited the switching in images (a) and (c). The magnetic hardening of Py is even more pronounced in ALS-8 compared to ALS-9.

Now we study data acquired on the Co edge. The respective images can be seen in the right column of Fig. 6.9 and in Fig. 6.10 (b), (c), and (d). First we study lower fields in Fig. 6.9. Image (b) is shown for reference reasons for comparison with the Fe edge. No magnetization change takes place. Visible periodic structures are attributed to topography due to sub-pixel shifts between the two images. In image (d), upon increasing the external field to 5.4 mT, two clusters of Co dots change magnetization along borders that correspond to borders in the respective Fe edge image (b). In the next field step in image (f) only three Co dots switch. In image (h), where the field is increased to 6.6 mT, and notably nearly all of the

Py has already switched, dots switch in stripe-like regions with borders parallel to the external field change magnetization. Notably magnetization changes can be observed in Co dots that have previously changed magnetization in the field step in image (b). In 6.10 (b), (c), and (d), further cluster-like switching is observed up to 8.4 mT. For the BCL of ALS-8 therefore $\mu_0 H$ =8.4 mT is needed to obtain the (nearly) saturated state.

Comparing sample ALS-8 and ALS-9, we can note identical field steps (4.2 mT to 4.8 mT to 5.4 mT) for the switching of Py areas without stripes under and between etched areas parallel to the external field. In both samples the stripes switch at larger fields, in sample ALS-8 at larger fields (up to 7.2 mT), if compared to sample ALS-9. The Py matrix is therefore found to be magnetically harder in a BCL with in-situ prepared interface compared to an oxidized interface. Only in ALS-8 we find Co dots that switch at a series of field steps. At the same time, we need a lager field to reverse Py.

6.3.3 Conclusion and Discussion

In the case of the oxidized sample, Co and Py switch at similar and relatively small fields. Co and Py switch in different sample regions. Sample ALS-8, which has been produced separately from ALS-9 and was found to exhibit elliptical Co dots shows a peculiar behavior in that Co dots change magnetization in several steps. We find magnetic hardening of Py in the non-oxidized samples compared to the oxidized sample. Further studies, where e.g. a non-magnetic material is deposited in the interface in a controlled manner, may bring more insight to the coupling between Py and Co in binary component systems.

Furthermore we conclude from the study, that the BCLs presented here made from Py with Co inclusions saturate at a field smaller than 9 mT. This is important for the dynamical studies performed later. Below we study the magnetization reversal based on micromagnetic simulations in order to elucidate the magnetization behavior further.

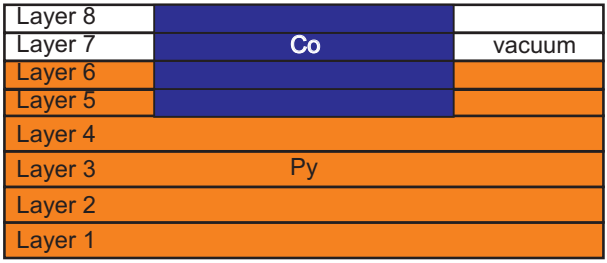

Figure 6.11: Sketch of the cross section of the micromagnetic simulation used for hysteresis simulation.

6.4 Micromagnetic Simulations

In this section we present findings from quasistatic micromagnetic simulations using the MicroMagus simulation software.

6.4.1 Magnetization Hysteresis for a $p = 1000$ nm BCL

We have performed quasistatic micromagnetic simulations of BCLs. We chose the parameters to model the samples studied in chapter 6.3. In order to compare findings we have used identical material parameters as found from dynamical studies of the samples (see chapter 6.5). The simulated unit cell consists of 64 pixels by 64 pixels in the film plane and 8 layers, see Fig. 6.11 for a sketch of the cross section of the simulated unit cell. The lateral size of the total simulated unit cell is 1 μm by 1 μm. 2D periodic boundary conditions are used. The bottom-most 4 layers consist of Py and are each $d = 4.75$ nm thick. Layers 5 and 6 consist of Co inclusions in the Py matrix and are each $d = 3.5$ nm thick. Layers 7 and 8 consist of Co dots in a vacuum matrix and are each $d = 3.5$ nm thick. The in-plane pixel edge length is 15.625 nm. This is larger than the exchange length of the system. Simulations have been performed also with 256 pixels by 256 pixels, resulting in a pixel edge length of 3.9 nm, smaller than the exchange length. Higher resolution simulations have been performed with only 3 layers, as the combination of high in-plane and high out-of-plane resolution was not possible due to restricted computational power. Both simulation sets have been compared and showed no significant differences

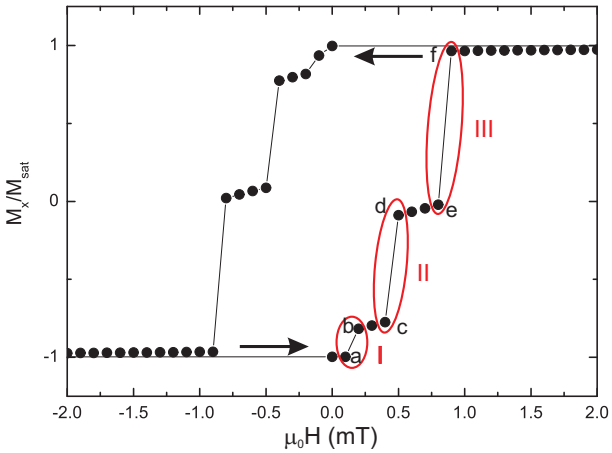

Figure 6.12: Magnetic hysteresis curve obtained from micromagnetic simulations on a $p = 1000$ nm binary component lattice. A side view of the unit cell is sketched in Fig. 6.11.

considering the magnetic hysteresis. For Py a saturation magnetization of $M_{\mathrm{sat,Py}} = 780$ kA/m was used, for Co $M_{\mathrm{sat,Co}} = 1000$ kA/m was chosen. An exchange constant of $A_{\mathrm{Py}} = 13 \times 10^{12}$ J/m was used for Py, $A_{\mathrm{Co}} = 20 \times 10^{12}$ J/m for Co. The damping coefficient was $\alpha = 0.01$. No anisotropy was considered.

In Fig. 6.12 we show the magnetic hysteresis curve obtained from these simulations. Here a saturation field of $\mu_0 H = -100$ mT was applied along the x-axis, parallel to a primitive lattice vector of the square lattice. Subsequently the field was ramped up to $\mu_0 H = -20$ mT and then to $\mu_0 H = 0$ in one step each. Then the field was increased to $\mu_0 H = 2$ mT in steps of 0.1 mT. After that the field was increased in larger steps to $\mu_0 H = 100$ mT. We show $\frac{M_x}{M_{\mathrm{sat}}}(H)$, i.e., the x-component of $\mathbf{M}$ averaged over all cells. The magnetization exhibits three distinct steps. Note the difference between $\mu_0 H = -0.1$ mT for the decreasing field branch compared to the state at $\mu_0 H = +0.1$ mT for the increasing field branch. The variation is attributed to stochastic processes occuring in the micromagnetic simulation. Step heights II and III correspond to $0.8\frac{\Delta M_x}{M_{\mathrm{sat}}}$ and $1\frac{\Delta M_x}{M_{\mathrm{sat}}}$, respectively.

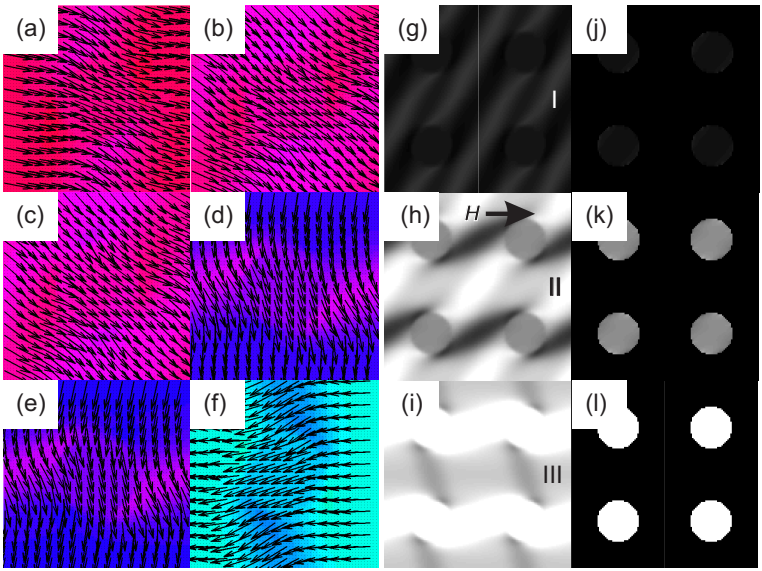

Figure 6.13: In plane component of the magnetization $\mathbf{M}(\mathbf{r})$ obtained from micromagnetic simulations on a $p = 1000$ nm binary component lattice. Arrows indicate the orientation of $\mathbf{M}(\mathbf{r})$ in layer 1. Color code indicates the angle of $\mathbf{M}(\mathbf{r})$. Grey-scale colormaps indicate differential change of $\mathbf{M}_\mathrm{x}(\mathbf{r})$, where the brightest (darkest) color stands for $\Delta\mathbf{M}_\mathrm{x}(\mathbf{r}) = -1$ (0). Studied field pairs are I: (a) 0.1 mT, (b) 0.2 mT., II: (c) 0.4 mT, (d) 0.5 mT, and III: (e) 0.8 mT, (f) 0.9 mT. In (g), (h), and (k) [(j), (k), and (l)] differential change of $\mathbf{M}_\mathrm{x}(\mathbf{r})$ simulated in layer 1 (layer 8) is shown.

We now study the microscopic magnetization changes using the space-dependent output parameter $\mathbf{M}(\mathbf{r})$ of the simulation software. In Fig. 6.13 (a) to (f) we show the magnetization configurations (a) to (f), respectively, the steps labelled by I, II, and III of Fig. 6.12. In Fig. (g) [(j)] the change in magnetization at step I of the bottommost [topmost] pure Py layer 1 [Co dot layer 8] projected onto the x-axis (i.e. parallel to the external field) $\Delta\mathbf{M}_\mathrm{x}(\mathbf{r})$ is shown in a 2 by 2 matrix, where the brightest (darkest) color stands for $\Delta\mathbf{M}_\mathrm{x}(\mathbf{r}) = -1$ (0). The maximum theoretically possible value is $\Delta\mathbf{M}_\mathrm{x}(\mathbf{r}) = -2$ indicating complete reversal. For steps II and

III, images (h), (i), (k), and (l) show the corresponding evaluation. Here we show pixel-wise subtracted data between field steps. [1] In step I, we find stripes in dark gray color in an orientation of 22.5° with respect to a primitive lattice vector. In step II throughout the unit cell we find stripes of bright color between rows of Co dots. The stripes are parallel to $\mathbf{H}$ and exhibit an oscillating contrast in field direction. Under the Co dot and in field direction between Co dots we find a bright-color in step III. For step III magnetization reversal is occurs in zig-zag shaped lines parallel to the field, containing Co dots. In step II, magnetization reversal is observed in the remaining areas, with contributions of up to $\Delta\mathbf{M}_\mathrm{x}(\mathbf{r}) = -1$ in diagonal lines, connecting areas under Co dots. Note that in, both, step II and step III, no pixel with $\Delta\mathbf{M}_\mathrm{x}(\mathbf{r}) = 0$ is found. Further studied layers of Py, Co inclusions in a Py matrix and Co inclusions in vacuum matrix are consistent with the analysis of layers 1 and 8.

We now compare findings from micromagnetic simulations with MTXM data of chapter 6.3. We find in MTXM data obtained on samples ALS-8 and ALS-9 that switching processes occur in a field regime from $\mu_0 H =$ 3 mT to $\mu_0 H = 8$ mT. These are larger compared to $\mu_0 H = 0.1$ mT to $\mu_0 H = 1$ mT extracted from the micromagnetic simulations. This is attributed to imperfections of the real sample concerning geometrical shape, material parameters and the interface between Py and Co with respect to the ideal simulated structure. In simulations, Co and Py do not switch independently as found in some MTXM data. Still, both simulations and experiments show a pattern where magnetization reversal takes place separately in firstly areas between rows of Co dots along the external field, and secondly in remaining areas. This sequence is consistent with experimental observations on ALS-8 and ALS-9 in the case of data taken at the Fe edge (Py). At the Co edge, we have observed that Co dots switch at even higher fields than the underlying Py. This is not found in simulations, where Co switches identically to the Py beneath the Co dots.

[1] This differs from MTXM data, where we showed pixel-wise divided data. Here we chose subtraction of images, as the data scales from -1 to 1, leading to possible division by zero and thus an over-proportional contribution of values divided by very small values, representing magnetization along the y-axis. In MTXM data, values vary by up to 10 % around a nonzero value. For MTXM we divided data pixel-wise in order to obtain maximum contrast.

6.4.2 Internal Fields

We now study the internal fields of BCLs and shallow-etched ADLs using micromagnetic simulations with the simulation package MicroMagus [Ber08]. In this work we have performed studies on BCLs and shallow-etched ADLs of periods $p = 1000$ nm and $p = 600$ nm. Here we discuss simulation data obtained on $p = 600$ nm structures in detail. An the end of this section we compare significant findings to data obtained on simulated $p = 1000$ nm structures in oder to show, that the findings can be generalized for both periods. Only for $p = 600$ nm simulations, due to computational constraints, in all three dimensions, it was possible to reduce the discretization size below the exchange length. Here, we have simulated a square lattice with period $p = 600$ nm of circular inclusions of $d = 310$ nm diameter. The inclusion was Co (vacuum) in a Py matrix for the BCL (shallow-etched ADL). The horizontal resolution was 128 pixels by 128 pixels resulting in a pixel edge length of $l_{\mathrm{pixel}} = 4.6875$ nm, smaller than the exchange length of all magnetic materials in the system. Vertically the simulated structure consisted of 8 (6) layers for the BCL (ADL). The bottom-most four 4-nm-thick layers 1 to 4 consisted of Py. The next two 4 nm thick layers 5 and 6 consisted of the Co or vacuum inclusions in a Py matrix. Layers 7 and 8 are 3.5 nm thick, each, and consisted only of Co dots and have only been simulated for the BCL. For Py a saturation magnetization of $M_{\mathrm{sat,Py}} = 780$ kA/m was used, for Co $M_{\mathrm{sat,Co}} = 1000$ kA/m was chosen. An exchange constant of $A_{\mathrm{Py}} = 13 \times 10^{12}$ J/m was used for Py, $A_{\mathrm{Co}} = 20 \times 10^{12}$ J/m for Co. The damping coefficient was $\alpha = 0.01$. No anisotropy was considered. The simulations have been performed at $\mu_0 H = 20$ mT.

In 6.14 we show in-plane magnetization configurations $\mathbf{M}(\mathbf{r})$ obtained with these simulations. Arrows indicate the direction of $\mathbf{M}(\mathbf{r})$. The color code shows the angle of $\mathbf{M}(\mathbf{r})$ with respect to the external field (pointing from left to right). The left (right) column shows BCL (ADL). We show the bottom-most pure Py layer 1, the uppermost binary layer 6 and the top dot layer 8. Layers in-between show no noticeable difference to their counterparts with identical composition. In each sample, apart from geometrical constraints, layers show identical magnetization. At the border between materials the magnetization points towards (away from) the edge for BCL (shallow-etched ADL).

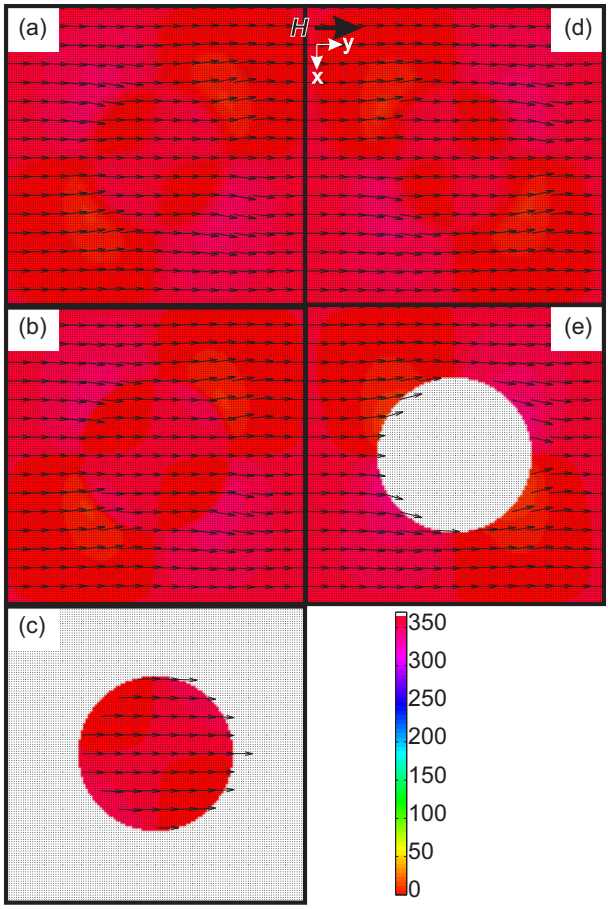

Figure 6.14: Simulated magnetization angle $\angle(\mathbf{M}(\mathbf{r}))$ indicated by arrows and color scale of a $p = 600$ nm (a)-(c) BCL, (d)-(e) ADL. Data acquired on layer (a) 1, (b) 6, (c) 8, (d) 1, (e) 6. Dots indicate simulation cells. Simulation performed at $\mu_0 H = 20$ mT.

In Fig. 6.15, we show the demagnetization field $\mu_0\mathbf{H}_{\mathrm{dem}}(\mathbf{r})$ obtained on the $p = 600$ nm BCL and shallow-etched ADL at $\mu_0 H = 20$ mT. Arrows indicate the direction of $\mu_0\mathbf{H}_{\mathrm{dem}}(\mathbf{r})$. The color code shows the amplitude of $\mu_0 H_{\mathrm{x,dem}}(\mathbf{r})$[1]. The external field is indicated in the image. Contour lines represent isoamplitude lines of constant $\mu_0 H_{\mathrm{x,dem}}$ spaced by 5 mT. The represented samples and layers are identical to Fig. 6.14. All images are scaled identically from $\mu_0 H_{\mathrm{x,dem}} = -60$ mT to $+60$ mT, where dark blue (red) stands for negative (positive) values larger (smaller) than 60 mT (-60 mT). The most notable difference between BCL in 6.15 (a), (c), and (e), if compared to the shallow-etched ADL in 6.15 (b) and (d) is the opposite sign of $\mu_0 H_{\mathrm{x,dem}}(\mathbf{r})\forall\mathbf{r}$. In both samples and in all layers two distinct channels of low $\mu_0 H_{\mathrm{x,dem}}$ perpendicular to the external field are found, labeled A and B in Fig. 6.15 (a). Channels are separated by the $\mu_0 H_{\mathrm{x,dem}} = 0$ contour line. In BCLs in the central (border) channel A (B) $\mu_0 H_{\mathrm{x,dem}}$ is antiparallel (parallel) to the external field $\mu_0 H$, resulting in a reduced (increased) effective field H_{eff} in this area. In the shallow-etched ADLs this situation is shifted by half a unit cell. In these channels the external field varies by values smaller than 2 mT along the central axis. This is in strong contrast to the variation between channels and along the material borders perpendicular to the channels. Further it can be seen that the absolute value of $H_{\mathrm{x,dem}}$ strongly increases at the material borders and changes sign exactly at the edge. The effect increases from the pure Py layer 1 in Fig. 6.15 (a) to the uppermost Co dot layer in 6.15 (e).

In Fig. 6.16 we show the spatial dependence of $H_{\mathrm{x,dem}}$ along a line parallel to the external field in the center of the unit cell (see white dashed line in Fig. 6.15 (a)). Data extracted from the same simulation set as before is represented by continuous lines. Increasing layer number in the set of curves is marked by an arrow, i.e. largest (smallest) amplitude is found in layer 8 (1). In the following, we will show data obtained using micromagnetic simulations using one pure Py layer, one layer with inclusions, and one layer with Co dots for BCLs thus increasing the individual layer thickness up to 16 nm. This is a value larger than the exchange length. For shallow-etched ADLs two layers will be used, respectively.

[1] Similar data for a BCL and a shallow-etched ADL with $p = 1000$ nm have been published in Ref. [Due11]

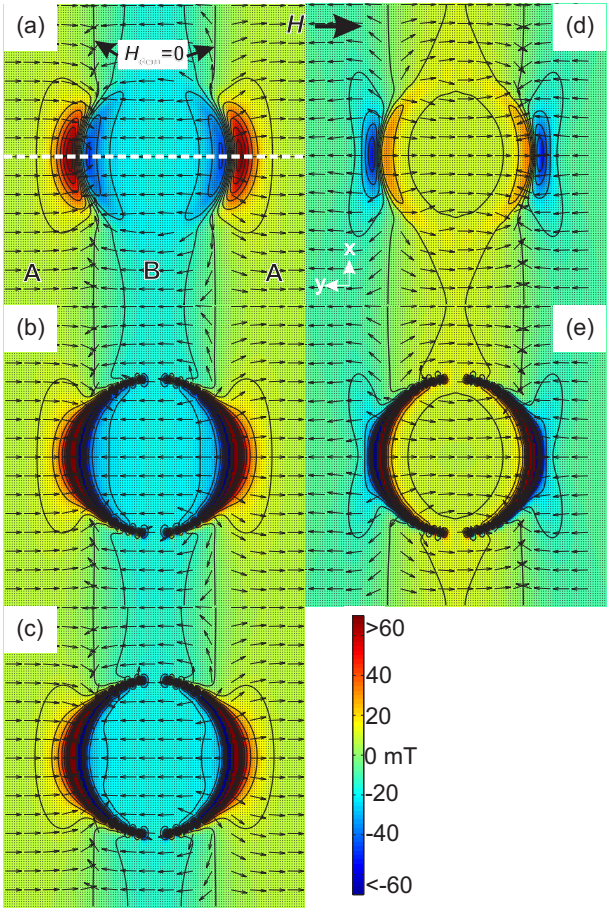

Figure 6.15: Simulated demagnetization field $\mu_0 \mathbf{H}_{\mathrm{dem}}(\mathbf{r})$, local orientation indicated by arrows (angle). Color scale indicates x-axis projection $\mu_0 H_{\mathrm{x,dem}}(\mathbf{r})$. Simulated structure is a $p = 600$ nm (a)-(c) BCL, (d)-(e) ADL. Data acquired on layer (a) 1, (b) 6, (c) 8, (d) 1, (e) 6. Dots indicate simulation cells. Simulation performed at $\mu_0 H = 20$ mT. Note that colors in (a) to (c) are complementary to colors (d) to (e) considering the vertical stripes formed by negative and positive field values.

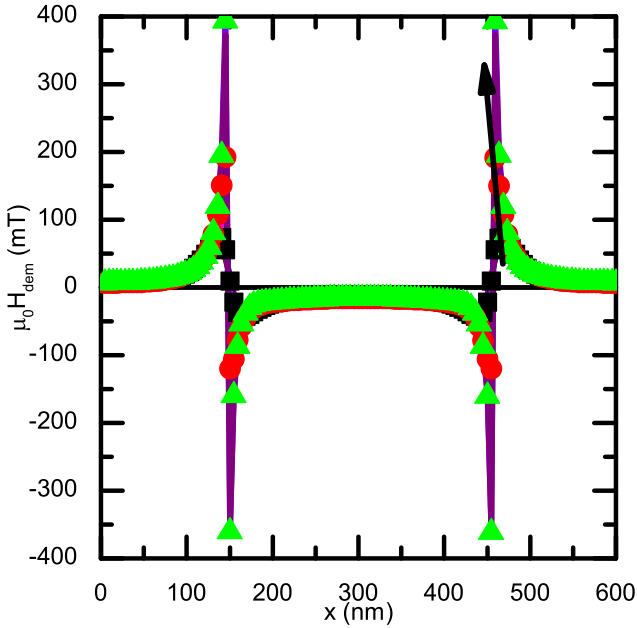

Figure 6.16: Comparison of $H_{\mathrm{x,dem}}$ for $p = 600$ nm BCL. Simulation performed at $\mu_0 H = 20$ mT. Data is evaluated for 8 layer simulations (lines, with layer number increasing along the black arrow) and 3 layer simulations (black square/ red disk/ green triangle stand for layers 1/2/3.

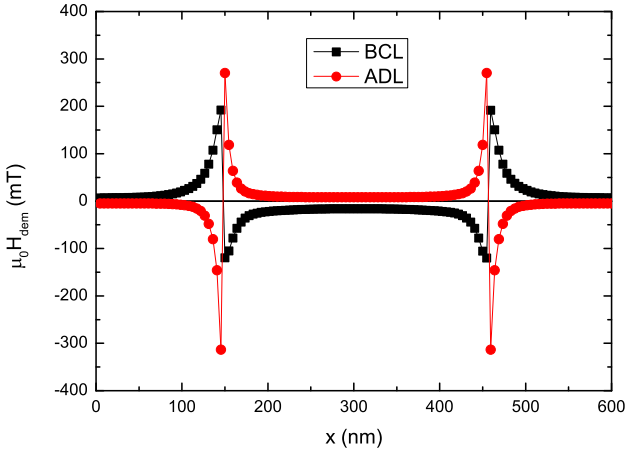

Figure 6.17: Comparison of $H_{\mathrm{x,dem}}$ for $p = 600$ nm BCL and shallow-etched ADL. Data is evaluated in layer 2 for BCL and shallow-etched ADL. Simulation performed at $\mu_0 H = 20$ mT.

The reduced layer numbers helped to speed up the simulations without changing the physics. Discrete symbols in Fig. 6.16 are obtained on a simulated structure with three layers. Apart from the number of layers, in three-layer simulations and eight-layer simulations all parameters were identical. Black squares are obtained on layer 1, red circles on layer 2, and green triangles on layer 3. Here the dependence of $H_{\mathrm{x,dem}}$ on the layer is well represented. We find that strong variations of $H_{\mathrm{x,dem}}$ are localized to the material edge where the sign of $H_{\mathrm{x,dem}}$ changes. The low $H_{\mathrm{x,dem}}$ channels are not influenced in their amplitude by the edge and the number of the layer. Furthermore no quantitative difference between simulations with eight or three layers can be seen, validating the approach using only three (two for shallow-etched ADLs) simulation layers.

Differences between shallow-etched ADLs and BCLs are studied in Fig. 6.17. Here layer 2, i.e. Py with Co inclusions of the three-layer simulation as presented before is compared to the respective two layer simulation

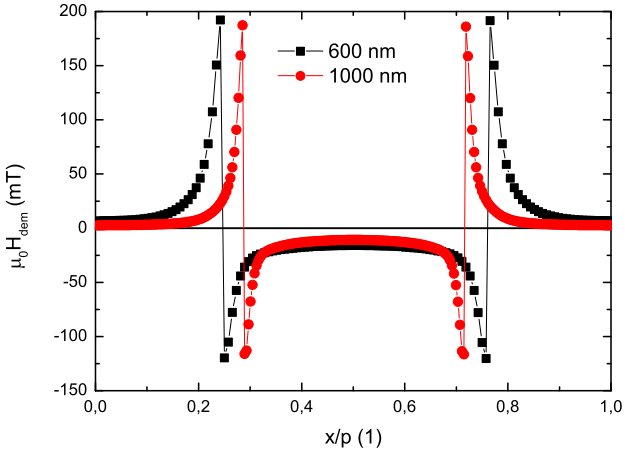

Figure 6.18: Comparison of $H_{\mathrm{x,dem}}$ for $p = 1000$ nm and $p = 600$ nm BCL. Data is evaluated in layer 2 of a 3 layer simulation. Simulation performed at $\mu_0 H = 20$ mT.

of shallow-etched ADL, where layer 2, i.e. Py with vacuum inclusion is used. As already studied, the sign of $H_{\mathrm{x,dem}}$ changes between structures. The maximum amplitude of $H_{\mathrm{x,dem}}$ is higher for the ADL due to the higher contrast in M_{sat}. The difference between the low-$H_{\mathrm{x,dem}}$ channels is smaller. Further we compare differences between structures of different periods p in Fig. 6.18 using a further simulation where $p = 1000$ nm. The spatial coordinate has been normalized to the unit cell length p in order to facilitate comparison. Note that magnetic parameters M_{sat} as well as the filling fraction change between structures, in order to remodel existing real samples. Amplitude differences of $H_{\mathrm{x,dem}}$ at the peaks as well as in the channels thus stem from differences in magnetic parameters. The x/p position of the peaks deviates due to the different filling fraction. Qualitatively no changes occur due to the reduced size. We can summarize our findings by stating that the inclusion of another magnetic material, in this case Co, into a shallow-etched ADL, thus forming a BCL changes the sign of $H_{\mathrm{x,dem}}$ all over the unit cell. In addition, Fig. 6.14 shows for the

$p = 600$ nm BCL, that 20 mT is efficient to align almost all spins in layers 2 and 3. In layer 2 of the shallow-etched ADL, spins at the hole edge still deviate considerably from the field direction.

6.5 Dynamic Magnetization of BCLs on SiN Membrane and GaAs Substrate Compared to Shallow-etched ADLs

6.5.1 Standing Spin Waves

We have employed AESWS measurements in order to study eigenfrequencies of various BCLs, corresponding ADLs, and shallow-etched ADLs. An overview of samples and relevant parameters is given in Table 6.1, at the beginning of this chapter. All lattices are square lattices of circular inclusions. Materials and geometrical parameters vary between samples. It is instructive to study the dependence of eigenfrequencies of all samples depending on external field strength $\mu_0 H$ and field angle η. We study eigenfrequencies using AESWS data $|a_{11}|$, i.e. reflection data after application of the difference technique. We compare micromagnetic simulations and AESWS experimental data with data from micro-BLS measurements performed at CNISM in Perugia, Italy by Dr. M. Madami and Dr. G. Gubbiotti.

In Fig. 6.19 we show field dependent eigenfrequencies $f(H)$ by plotting $|a_{11}|$ data acquired on different samples. Bright (dark) color represents more (less) intense $|a_{11}|$ signal. $|a_{11}|$ has positive values only. Each image is normalized to its maximum value. In all images of Fig. 6.19, a constant line at approximately $f = 10$ GHz can be seen. These lines are attributed to the difference technique used to calculate $|a_{11}|$ (see chapter 3). These excitations correspond an excitation at $\mu_0 H = 100$ mT, $\eta = 90°$ subtracted from all datasets. In Fig. 6.19 (a) data acquired on the BCL 118-4-2 with period $p = 1000$ nm is shown. The CPW had an inner conductor width $w_{\mathrm{IC}} = 4.8$ μm. In Fig. 6.19 (b) we show data acquired on the corresponding shallow-etched ADL 118-6-3 with $p = 1000$ nm with identical w_{IC} of the CPW. In both images, two prominent modes with continuously

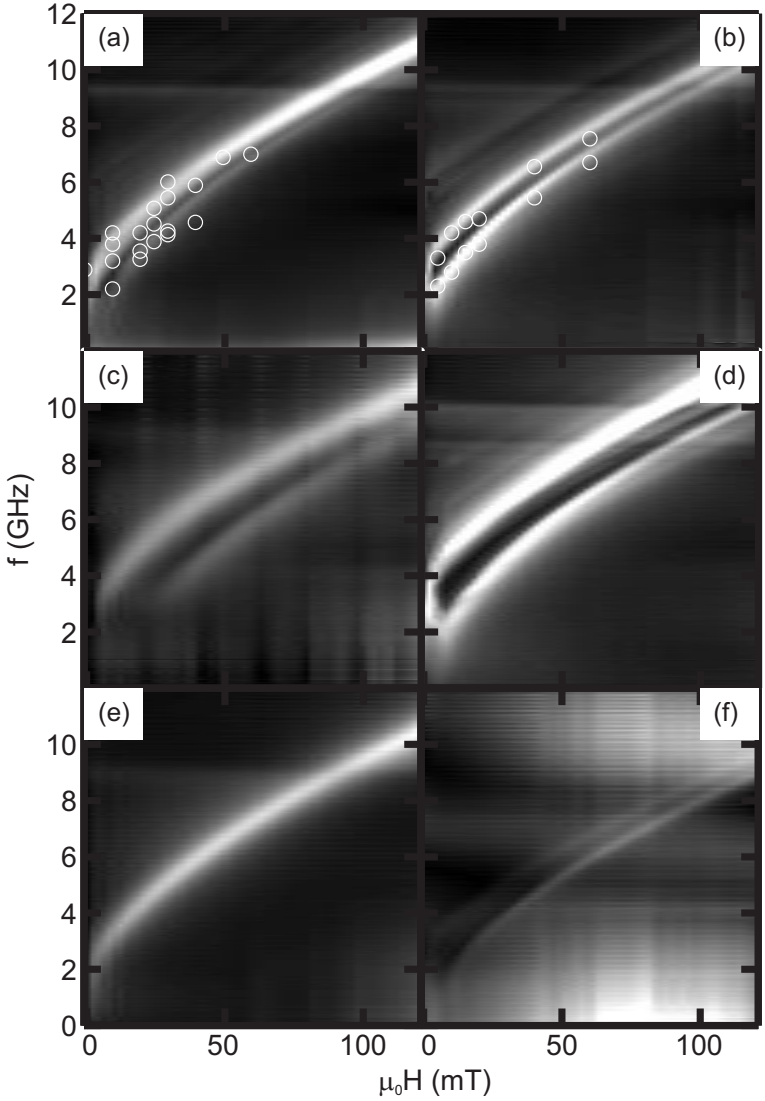

Figure 6.19: AESWS $|a_{11}|$ data obtained on (a) $p = 1000$ nm BCL 118-4-2, (b) $p = 1000$ nm shallow-etched ADL 118-6-2, (c) $p = 600$ nm BCL 138-B2-4, (d) $p = 600$ nm shallow-etched ADL 138-B1-1, (e) plain film 138-B2-1, (f) $p = 600$ nm $t_{mesa} = 8$ nm ADL 140-3-1. White circles indicate μBLS data. Samples have been saturated at $\mu_0 H = 120$ mT before acquiring the data. Reference data is subtracted from each dataset and acquired at $\mu_0 H = 120$ mT and $\eta = 90°$.

increasing frequency depending on the external field $f(H)$ are resolved. Notably in the BCL sample in Fig. 6.19 (a) the higher frequency mode exhibits higher intensity if compared to the lower frequency mode that is no resolved above $\mu_0 H = 100$ mT and below $\mu_0 H = 8$ mT. Further weak modes are found at larger f. In Fig. 6.19 (b) for the shallow-etched ADL sample, two modes are equally strong and visible throughout the whole field regime. Micro-BLS data is overlayed as white circles. Data has been acquired by feeding a microwave signal to the CPW and sweeping the excitation frequency continuously and extracting relevant BLS peaks over the whole frequency range. Micro-BLS data provides good agreement with AESWS data. In Fig. 6.19 (c) and (d) data acquired on $p = 600$ nm BCL (c) and shallow-etched ADL (d) are shown. Here a $w_{\mathrm{IC}} = 2$ μm CPW was used. In Fig. 6.19 (c) two distinct modes can be identified. The lower frequency mode vanishes for fields $\mu_0 H < 20$ mT. In Fig. 6.19 (d) modes exhibit higher signal-to-noise ratio compared to (c). For fields $\mu_0 H < 60$ mT, two modes are visible in (d). Both modes split into two further modes at around $\mu_0 H = 60$ mT. This presents are more complex mode behavior compared to both the BCL and the shallow-etched ADL with large period $p = 1000$ nm. Figure 6.19 (e) shows data acquired on a plain Py film (138-B2-1) for reference. The $w_{\mathrm{ICW}} = 2$ μm CPW was nominally identical to the above mentioned $p = 600$ nm samples in (c) and (d). A further dataset is presented in Fig. 6.19 (f), obtained on ADL sample 140-3-1. With respect to sample 138-B1-1 in Fig. 6.19 (d) the Py mesa's thickness $t_{\mathrm{mesa}} = 8$ nm is drastically reduced and the sample is a fully etched-through antidot lattice. Here two prominent modes can be seen as well. The signal-to-noise ratio is smaller due to lesser amount of magnetic material if compared to samples of higher t_{mesa}. The slope $\partial f / \partial H$ is smaller if compared to all other samples, resulting in a smaller excitation frequency f at $\mu_0 H = 120$ mT.

In Fig. 6.20 we show data obtained on the $p = 1000$ nm BCL ALS-8 prepared on SiN membrane for the MTXM studies presented in Figs. 6.9 and 6.10. Data was obtained using a continuous CPW. The lower signal-to-noise ratio compared to data shown in Fig. 6.19 is attributed to the smaller mesa length (50 instead of 300 µm) and the larger CPW length (5 mm instead of 400 µm). The long CPW allowed us to place the BCL face down onto the CPW while monitoring the position through the transparent 100 nm thin membrane. Note that geometrical parameters of the BCL

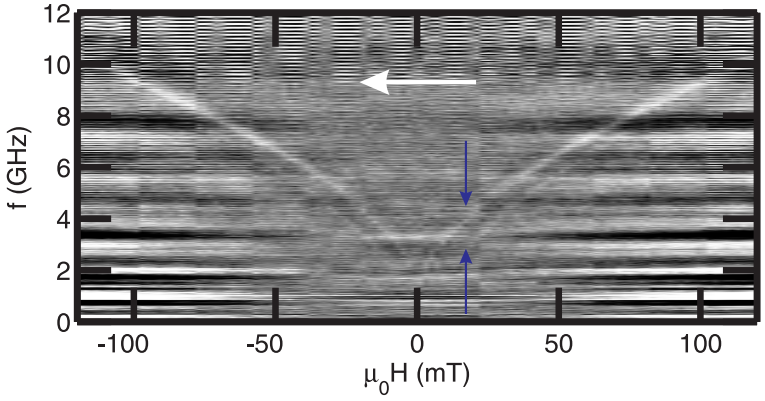

Figure 6.20: VNA-FMR $|a_{12}|$ data obtained on $p = 1000$ nm BCL ALS-8 on SiN membrane. Blue arrows indicate resolved modes. The white arrow indicates the direction of data acquisition: Saturation at $\mu_0 H = 120$ mT and subsequent measurements at decreasing field.

vary only slightly with respect to sample 118-4-2 (see Table 6.1). The two most intense modes for sample ALS-8 (blue arrows) are consistent with Fig. 6.19. Data obtained at positive and negative field values, where the sample was saturated at 120 mT before all measurements, is shown. No hysteretic effects are resolved.

In Fig. 6.21 (a) we show resonance frequencies extracted from data shown in Fig. 6.19 (a) on the $p = 1000$ nm BCL 118-4-2 on GaAs substrate. We compare data obtained at positive and negative values of H when the BCL experienced the identical magnetic history, i.e., it was saturated at $+120$ mT [data obtained at negative values was not shown in Fig. 6.19 (a)]. Here only the resonance frequencies of the two most intense modes are shown. Full black squares (open red circles) are extracted at a positive (negative) field. The blue star indicates the resonance frequency at zero field. The black (red) arrow indicates the field sweep history for positive (negative) values. For the higher frequency mode, no discrepancy between positive and negative H is found. For the lower frequency mode, hysteresis is found for $\mu_0 H = 6$ and 8 mT. Here, data obtained at negative field values after saturation at positive fields exhibits higher frequency

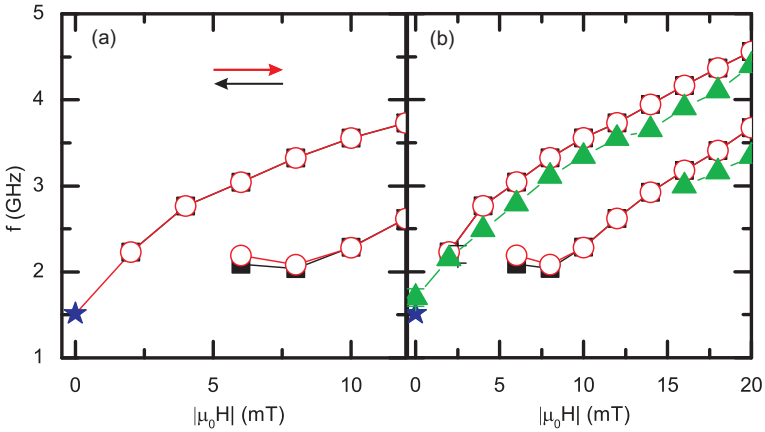

Figure 6.21: AESWS $|a_{22}|$ local maxima obtained on $p = 1000$ nm BCL 118-4-2 on GaAs substrate. Full black squares (open red circles) are extracted at a positive (negative) sign of the field. The blue star indicates the maximum at zero field. Green triangles are extracted maxima from sample ALS-8 on SiN membrane. The first data point of each dataset in (b) contains a representative error bar.

compared to data obtained at positive values. The frequency difference amounts to 0.1 GHz at 6 mT. The simulated hysteresis in 6.13 has not shown hysteretic effects for fields larger than 1 mT. For the experimentally observed hysteresis of sample ALS-9 shown in Fig. 6.8, however, it was found that Co dots switched for fields up to 5.4 mT. We thus attribute the hysteresis found in Fig. 6.21 (a) to the experimentally observed hysteretic behavior of Co nanodiscs in a BCL. Note that the dot diameter d varies between both samples, suggesting slightly different switching fields. Futhermore in Fig. 6.21 (b) we compare extracted resonance frequencies with data of ALS-8 in 6.20 (b) (green triangles). Although ALS-8 varies in shape compared to the BCLs ALS-9 and 118-4-2, we find similar frequencies over a broad field regime, substantiating the consistent quasistatic and dynamic behavior of samples on SiN membranes and GaAs substrates. Note that the field dependence of the low-frequency mode [circles in 6.21 (a)] exhibit a negative (positive) slope for $\mu_0 H \leq(\geq)8$ mT. This will be discussed below.

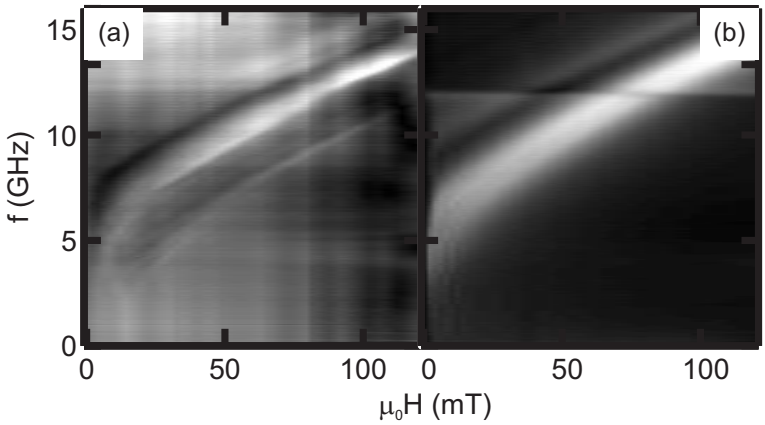

Figure 6.22: AESWS $|a_{11}|$ data obtained on (a) $p = 600$ nm CoFeB(Py) BCL CoFeB-2-B, (b) CoFeB plain film CoFeB-2-C. Samples have been saturated at $\mu_0 H = 120$ mT before acquiring the data. Reference data is subtracted from each dataset and acquired at $\mu_0 H = 120$ mT and $\eta = 90°$.

Before discussing modes in detail, it is instructive to compare BCLs of different materials. In Fig. 6.22 we show data obtained on a $p = 600$ nm CoFeB BCL with Py inclusions CoFeB-2-B (a) and a corresponding plain film CoFeB-2-C. Note that the frequency axis goes up to $f = 16$ GHz in contrast to Fig. 6.19 (c), now covering a larger frequency regime. Eigenfrequencies are higher due to the higher M_{sat} of CoFeB if compared to Py. In Fig. 6.22 (a) the BCL exhibits two modes similar to Py BCLs with Co inclusions in Fig. 6.19 (c). The plain CoFeB film is studied in Fig. 6.22 (b).

In Fig. 6.23 we show AESWS $|a_{11}|$ data and study the angular dependence of the frequency $f(\eta)$ at $\mu_0 H = 20$ mT. Images (a) to (d) and (f) correspond to samples in the respective images in Fig. 6.19. In 6.23 (e) sample 140-4-6 is shown instead of the plain film. Sample 140-4-6 is a BCL without Py underlayer (see Table 6.1). Large white areas in 6.23 (a) - (c) indicate missing data. Spectra are symmetric with respect to $\eta \approx 0°$. The plane of mirror symmetry is not exactly at $\eta = 0°$ because of a misalignment of the sample in the magnet. Comparing BCLs and correspond-

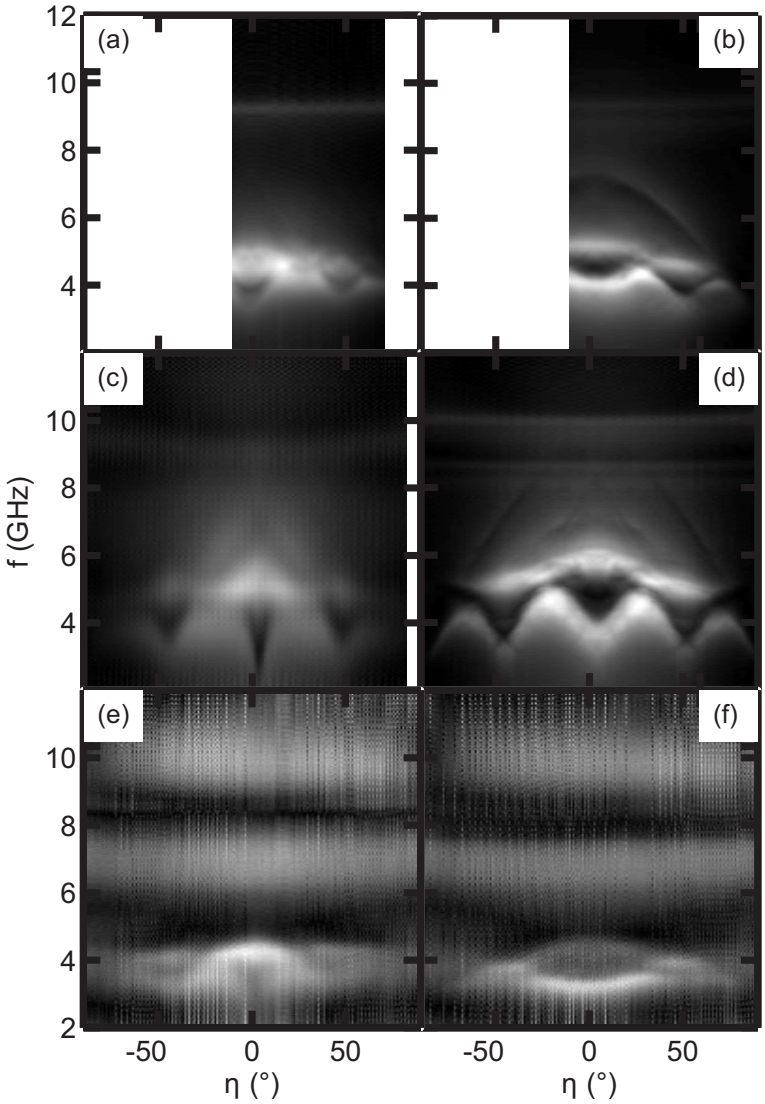

Figure 6.23: AESWS $|a_{11}|$ data obtained at $\mu_0 H = 20$ mT on (a) $p = 1000$ nm BCL 118-4-2, (b) $p = 1000$ nm shallow-etched ADL 118-6-2, (c) $p = 600$ nm BCL 138-B2-4, (d) $p = 600$ nm shallow-etched ADL 138-B1-1, (e) $p = 600$ nm $t_{mesa} = 8$ nm BCL 140-4-6, (f) $p = 600$ nm $t_{mesa} = 8$ nm ADL 140-3-1. White color indicates a resonance.

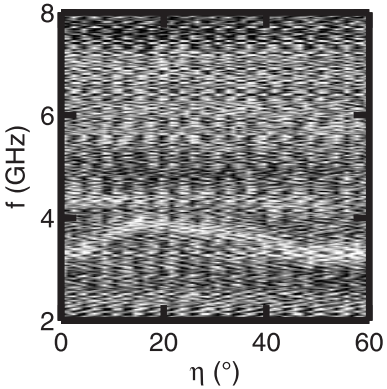

Figure 6.24: VNA-FMR $|a_{12}|(\eta)$ data obtained on $p = 1000$ nm BCL ALS-8 on SiN membrane at $\mu_0 H = 20$ mT.

ing ADLs and shallow-etched ADLs, we find that for BCLs modes are weaker and provide less contrast. The lowest attainable frequency of the low frequency mode around $\eta = 0°$ is nearly 2 GHz smaller for BCLs. A third mode at frequencies higher than $f = 6$ GHz can be seen only in shallow-etched ADLs. Frequencies f and variation of frequencies $f(\eta)$ are notably smaller for the $t_{\mathrm{mesa}} = 8$ nm samples. Again the signal is much weaker due to the reduced amount of magnetic material. We find for all samples similar behavior in that at high-symmetry directions $\eta = 0°$ and $45°$ the two most prominent modes exhibit a large frequency difference, but are nearly degenerate for $\eta \approx 22.5°$. In Fig. 6.24 we show $f(\eta)$ obtained on sample ALS-8 on the SiN membrane (see also Fig. 6.20). At $\eta = 0$ two modes at 3.2 GHz and 4.2 GHz are clearly resolved, similar to the $p = 1000$ nm BCL 188-4-2 (Fig. 6.23 (a)).

We now discuss micromagnetic simulations to explain the characteristic field and angular dependencies. Dynamic micromagnetic simulations were performed using the MicroMagus simulation package [Ber08]. Magnetic parameters are identical to quasistatic simulations of $p = 1000$ nm and $p = 600$ nm BCLs and shallow-etched ADLs in chapter 6.4. Now spin precession is induced by a Gaussian field pulse of 2 mT amplitude applied perpendicular to the in-plane field $\mu_0 H$ pointing $45°$ out-of-plane.

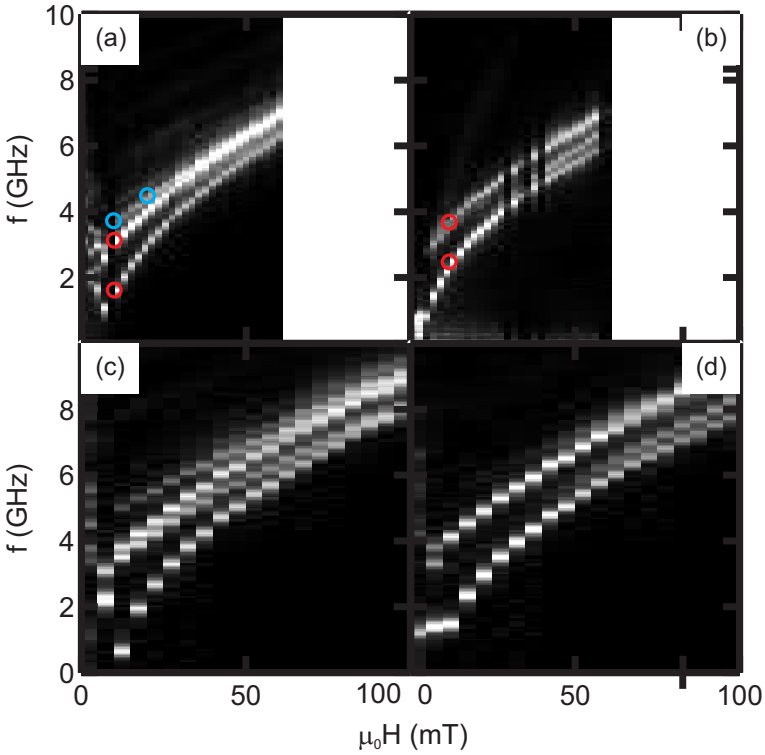

Figure 6.25: Simulated eigenfrequency spectra $f(H)|_{k=0}$ for (a) $p = 1000$ nm BCL, (b) shallow-etched ADL, (c) $p = 600$ nm BCL, and (d) shallow-etched ADL. Red (blue) circles correspond to spatial profiles shown in Fig. 6.26 (Fig. 6.31).

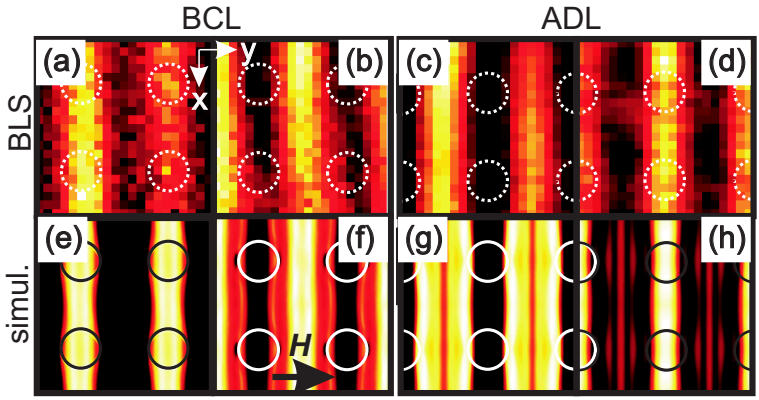

Figure 6.26: Measured spin precession profiles (2×2 μm^2) obtained by μBLS [(a) to (d)] and simulated ones [(e) to (h)]. μ_0H $= 10$ mT is applied along the black arrow. The outer edge of the CPW's ground line is at the top edge of each graph. The respective lower (higher) f mode is marked by images (a), (c), (e), and (g) [(b), (d), (f), and (h)].

We used uniform excitation of the unit cell so only standing spin waves are studied. We show simulated eigenfrequencies in Fig. 6.25. In figs. (a) and (b) [(c) and (d)] $p = 1000$ nm ($p = 600$ nm) BCL and shallow-etched ADLs are shown. For a given external field $\mu_0 H$ time-dependent simulations have been performed. Bright color in Fig. 6.25 represents high spectral power of a given frequency at a given field resulting from frequency-domain transformation of the time-dependent data. We now compare simulated eigenfrequencies with AESWS and micro-BLS data from Fig. 6.19. We find that experimental and simulated data agree well. We attribute remaining discrepancies in eigenfrequency values to sample imperfections as rough edges of the shallow-etched holes and the residual crystalline anisotropy of the polycrystalline Co grown on the etched Py. We did not take these features into account when performing simulations. For all samples the relevant frequency regime is similar. Eigenfrequencies are always between about 2 to 10 GHz.

It is now instructive to study the spatial localization of the most intense eigenmodes of the system using μBLS and micromagnetic simulations.

We will study eigenmodes of the $p = 1000$ nm BCL and shallow-etched ADL at an external field $\mu_0 H = 10$ mT (see Figs. 6.19 (a) and (b) and 6.25 (a) and (b)). At this field the micro-BLS signal was most intense. Studied excitations are marked in Figs. 6.19 and 6.25 with red circles. Using micro-BLS, we measure a 2D spatial map of the amplitude of an eigenresonance at a given frequency over an array of 2×2 μm^2 by exciting the system with a constant microwave frequency through the CPW. Micro-BLS maps of normalized intensities are shown in Fig. 6.26 (a) to (d). Here the CPW was located parallel to the top edge of each image. In all images large micro-BLS signals (in bright color) corresponding to large spin precession amplitudes can be seen in parallel, vertical stripes, perpendicular to the coplanar waveguide and the external field $\mu_0 H$. For BCLs (shallow-etched ADLs) Co dots (etched areas) were resolved by the built-in microscope and are indicated by dashed circles. Exciting the low frequency resonance, at $f = 1.8$ GHz, in the BCL in Fig. 6.26 (a) leads to large spin precession in channels through the Co dots. The amplitude does not noticeably vary between Py and Co areas. When we excite at the higher frequency resonance, i.e. at $f = 3.2$ GHz, we find in Fig. 6.26 (b) that the excitations shift along the external field by half a lattice constant, i.e. by 500 nm. Now excitations take place in Py, only. We now compare these findings with shallow-etched ADLs in Fig. 6.26 (c) and (d) for excitations at $f = 2.8$ GHz (c) and 4.2 GHz (d). Here the lower frequency excitations are found in the non-etched areas while the higher frequency excitation are found between and below the etched areas. This means higher and lower frequency excitations change place, i.e. shift by half a lattice period in the shallow-etched ADL compared to the BCL.

We can substantiate these findings by studying spatial FFT maps for the given frequencies as exctracted from time-resolved dynamic micromagnetic simulations. Studied frequencies are marked in Fig. 6.25 (a) and (b) by red circles. We show these spatial FFT maps in Fig. 6.26 (e) to (d). Here, edges between materials are indicated by white circles. All spatial FFT maps show excitations that extend throughout channels perpendicular to the external field, spaced by the lattice period $p = 1000$ nm. The stripe-like extended modes correspond in their localization pattern to the respective micro-BLS maps.

The difference in localization between BCL and shallow-etched ADL

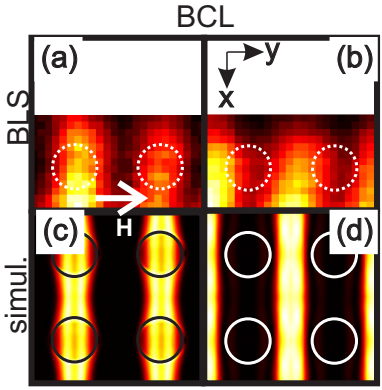

Figure 6.27: Measured spin precession profiles obtained by μBLS (upper row) and simulated ones (lower row) on the $p = 600$ nm BCL 138-B2-4. μ_0H $= 35$ mT is applied along the white arrow. The outer edge of the CPW's ground line is at the top edge of each graph. The respective lower (higher) f mode is marked by i (ii).

is elucidated by considering the demagnetization field H_{dem} as studied in chapter 6.4.2. The eigenfrequency of a given mode depends on the local effective field. High (low) effective fields cause high (low) resonance frequencies disregarding confinement effects at this point. In chapter 6.4.2 we found low (high) effective field for BCLs in stripes perpendicular to the external field and through the (between rows of) Co dots. As a consequence, this is where we find the low (high) frequency mode i (ii). For the shallow-etched material the situation is consistent with Fig. 6.15, because of the inversed sign of H_{dem} compared to the BCL. The direction of H_{dem} is governed by the material of highest M_{sat} and thus counteracts M_{Co} in BCLs and M_{Py} in shallow-etched ADLs. This causes the spatial mode shifting observed in experiment and simulation. In Fig. 6.27 we show equally acquired images for the $p = 600$ nm BCL at $\mu_0 H = 35$ mT. Here we find the identical situation as for the $p = 1000$ nm sample. This is expected from findings in chapter 6.4.2 where no significant difference in H_{dem} was found for samples of different period p.

We further discuss findings in Fig. 6.21 (a), where frequency maxima of the $p = 1000$ nm BCL 118-4-2 are shown. We note that the lower-

frequency mode's increase in frequency with decreasing field is found in experiment and simulation: In 6.25 (a), i.e. the simulation, the minimum is found at 6 mT, in Fig. 6.21, i.e. the experimental data (a) it is found at 8 mT. The spatial profile of the lower frequency mode, is shown in 6.26 (e) for 10 mT. For frequencies down to 4 mT the shape is nearly identical (not shown). We attribute the minimum of this mode, extending through and under the Co dots, to the anisotropy field introduced by the Co dots. As the lower frequency mode extends through the Co dots, it is susceptible to the influence of the anisotropy field, in contrast to the higher frequency mode, extending only in Py. The resulting hard-axis behavior is comparable to the frequency minimum in field dispersions of nanowires, in Fig. 5.1 (b).

We also used micromagnetic simulations to analyze $f(\eta)$ in further detail. In Fig. 6.28 we show data obtained from dynamic micromagnetic simulations performed at $k = 0$. In contrast to the simulations shown above, now $\mu_0 H = 20$ mT was kept constant and η was swept from 0 to $60°$. In Fig. 6.28 we show simulation data for (a) a $p = 1000$ nm BCL and (b) a $p = 600$ nm ADL. The corresponding experimental $|a_{11}|$ data is shown in Fig. 6.23 (a) and (c). We study the two lowest frequency modes marked (i) and (ii). At $\eta = 0$, 22, and $45°$ we show spin-precession profiles extracted from micromagnetic simulations at (f, η) values marked by green circles. The lower (upper) row shows profiles of mode i (ii). Modes extracted at $\eta = 0$ correspond to the modes discussed above and are replotted. At $\eta = 22°$ and $\eta = 45°$ mode (i) has highest amplitude under the Co dots and in channels in between, perpendicular to the applied field. This is identical to the $\eta = 0$ case. Mode (ii) shows are more complicated shape: At $\eta = 22°$, excitations are most pronounced at edges between Py and Co. No continuous channels of high excitation exist throughout the lattice. Interestingly, at $\eta = 45°$, the $p = 1000$ nm sample in Fig. 6.28 (a) shows a pattern similar to $\eta = 0$ rotated by $\eta = 45°$. The $p = 600$ nm sample in Fig. 6.28 (b) exhibits higher quantization with two maxima in each channel between Co dots. This quantization arises with decreasing period p. The frequency difference between modes (i) and (ii) increases for $\eta = 0$ and $\eta = 45°$ where the impact of the periodic variation of the demagnetization field is strongest due to high symmetry. Decreasing the lattice period from 1000 nm to 600 nm increases both, this influence, and the frequency difference between mode (i) and (ii) whereas for less symmetric field directions frequencies remain similar. Note that the mode shapes differ significantly from previously found modes in etched-through

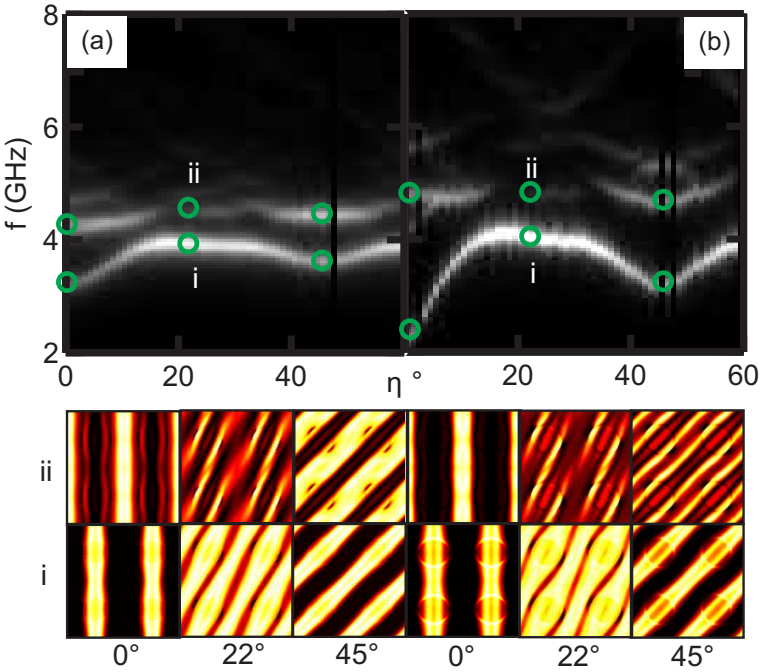

Figure 6.28: Simulated eigenfrequency spectra $f(\eta)|_{k=0,\mu_0 H=20\ \mathrm{mT}}$ for (a) $p =$ 1000 nm BCL and (b) $p =$ 600 nm BCL. Simulated spin-precession profiles are shown beneath the respective gray-scale plot. Profiles are extracted at (f, η) values marked by green circles.

ADLs as shown at the beginning of this chapter in Fig. 6.1. It is now interesting whether the BCL design allows for improved spin-wave propagation characteristics compared to etched-through ADLs.

6.5.2 Propagation

We now study propagation of spin waves using AESWS, BLS and the PWM.

In Fig. 6.29 we show AESWS $\Re(a_{12})$ data obtained on (a) $p = 1000$ nm

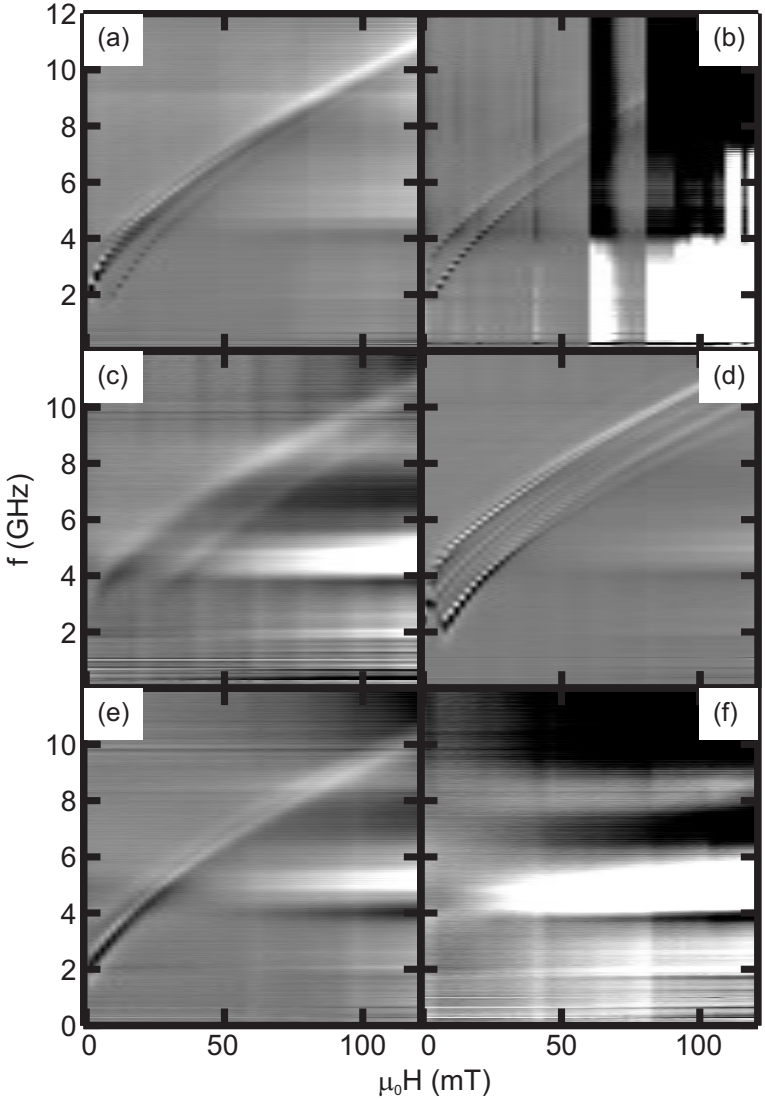

Figure 6.29: AESWS $\Re(a_{12})$ data obtained on (a) $p = 1000$ nm BCL 118-4-2, (b) $p = 1000$ nm shallow-etched ADL 118-6-2, (c) $p = 600$ nm BCL 138-B2-4, (d) $p = 600$ nm shallow-etched ADL 138-B1-1, (e) plain film 138-B2-1, (f) $p = 600$ nm $t_{mesa} = 8$ nm ADL 140-3-1.

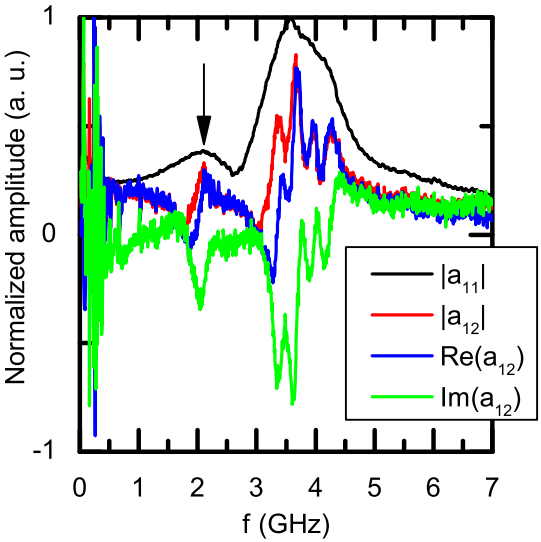

Figure 6.30: AESWS data obtained at $\mu_0 H$ =10 mT on a p = 1000 nm BCL sample.

BCL 118-4-2, (b) p = 1000 nm shallow-etched ADL 118-6-2, (c) p = 600 nm BCL 138-B2-4, (d) p = 600 nm shallow-etched ADL 138-B1-1, (e) plain film 138-B2-1, (f) p = 600 nm t_{mesa} = 8 nm ADL 140-3-1. All data was obtained at $\eta = 0°$. Here the real part of transmission data $\Re(a_{12})$ is shown. In such data, black-white-black oscillating contrast is attributed to spin-wave propagation, see chapter 3.

$p = 1000$ **nm samples**

We will first consider p = 1000 nm samples. In Fig. 6.30 we show a spectrum obtained on the p = 1000 nm BCL sample in order to study the oscillating contrast in detail. Lineplots for $\mu_0 H$ = 10 mT show reflected and transmitted amplitude $|a_{11}|$ and $|a_{12}|$, respectively, as well as real and imaginary parts of a_{12}. The data have been normalized to their respective

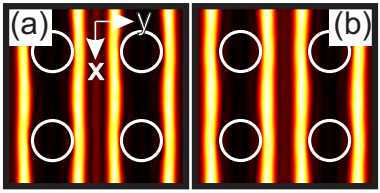

Figure 6.31: Simulated spin-precession profiles at (a) $\mu_0 H = 10$ mT (b) $\mu_0 H = 20$ mT for the $p = 1000$ nm BCL. Eigenfrequencies are marked in Fig. 6.25 by blue circles.

maximum. $|a_{11}|$ shows two resonances at about 2 and 3.5 GHz. Considering the lower frequency mode, $|a_{12}|$, $\Re(a_{12})$, and $\Im(a_{12})$ show the signature of a resonant excitation. The higher frequency mode exhibits a more complex pattern. In Fig. 6.30, i.e. for $\mu_0 H = 10$ mT, oscillations in $\Re(a_{12})$ and $\Im(a_{12})$ are resolved around a strongly varying baseline. $|a_{12}|$ shows an oscillating pattern as well. This shape is in contrast to propagating spin waves in plain films. In Fig. 6.30 the data a_{12} is distorted, allowing no quantitative estimates on the group velocities. We find a splitting of the high-frequency mode into several modes not resolved in $|a_{11}|$ AESWS data, but in a_{12} data.

Further studies reveal, that in Fig. 6.29 (b) oscillating contrast in the shallow-etched ADL is attributed to eigenresonances. No propagation is resolved, thus v_g cannot be extracted from the available data. Note that the transmission distance d amounted $d = 19.2$ µm following the CPW design. The absence of a clear propagation signal for the $p = 1000$ nm devices suggest that $d = 19.2$ µm was beyond the decay length of the relevant spin-wave modes. The distinct dispersive properties of the modes will be elucidated further in the following paragraph based on micromagnetic simulations.

Finite-width CPWs excite in a specific regime of wave-vectors (see Fig. 3.4). The CPWs integrated to $p = 1000$ nm samples had a maximum excitation strength of $k = 0.36$ µm^{-1}. We now discuss the spin-wave dispersion relation in this wave vector regime. For this, we have performed micromagnetic simulations, to calculate the dispersion relation $f(k)$at $\mu_0 H = 20$ mT. To reproduce the sample composition, we simu-

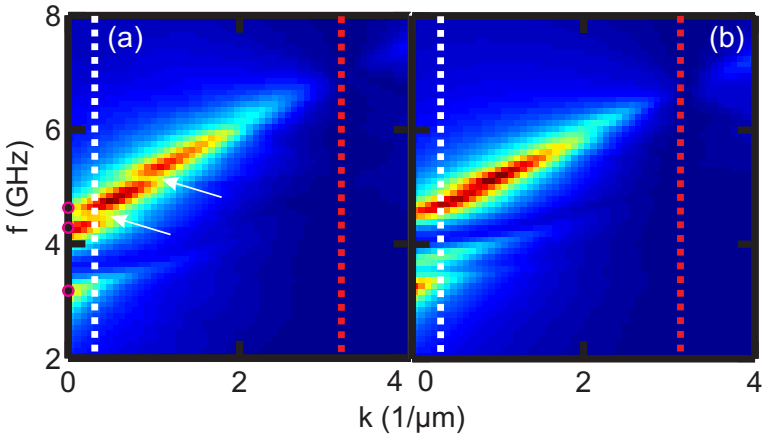

Figure 6.32: Simulated dispersion relation $f(k)$ for $p = 1000$ nm (a) BCL and (b) shallow-etched ADL at $\mu_0 H = 20$ mT. White lines indicate k_{CPW}, red lines indicate the first BZ boundary.

lated a structure composed by three (two) different layers using 2D boundary conditions: a 16 nm thick bottom layer consisting only of Py, a 8 nm thick middle layer consisting of Co dots fully embedded in Py (holes in Py for the shallow-etched ADLs), and a 7 nm thick top layer consisting only of Co dots (this layer was left out for shallow-etched ADLs). The lattice constant and the radius of Co dots have been set to the values of the real sample. The saturation magnetizations and the exchange constants have been fixed to the values used for $k = 0$ simulations. In Fig. 6.32, we show the resulting $f(k)$ for (a) $p = 1000$ nm BCL, (b) shallow-etched ADL obtained from these simulations. The first Brillouin zone (BZ) boundary is marked by the red dashed line. We now compare $f(k \to 0)$ with the respective simulation at $\mu_0 H = 20$ mT in Fig. 6.25 (a). The excitations found in $k = 0$ simulations are marked by magenta circles at $k = 0$ in Fig. 6.32. The lowest frequency excitation at $k = 0$ is attributed to the mode extending throughout Co and Py. Its branch does not extend though the first BZ. The two higher-frequency excitations, the Py mode and the higher order Py mode (shown in 6.31 and referenced by a blue circle in Fig. 6.25) undergo an avoided crossing inside the first BZ. The crossing is at $k = 0.36$ μm^{-1} (left white arrow). This value coincides with the

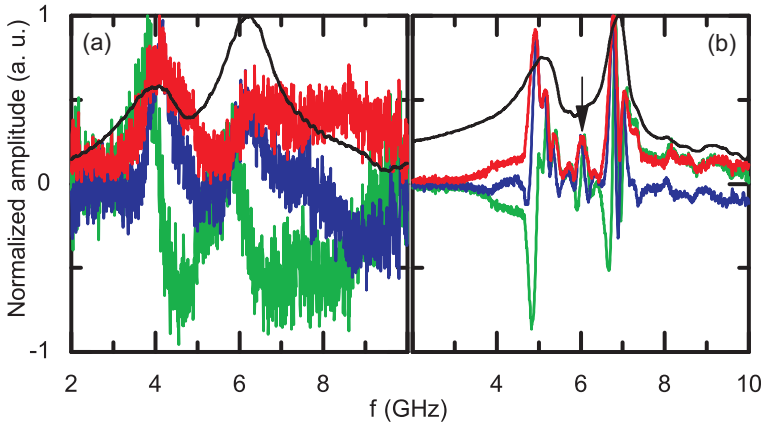

Figure 6.33: AESWS data obtained at $\mu_0 H$ =35 mT on (a) the $p = 600$ nm BCL sample, (b) the $p = 600$ nm shallow-etched ADL sample. The black arrow highlights the lower frequency mode excited by the second wavevector of the CPW.

wavevector best excited by the CPW, marked by the white dashed line. One further avoided crossing is visible (right arrow), however the mode to be crossed vanishes for k_{CPW} and $k = 0$ so it is neither resolved in AESWS data nor in $k = 0$ simulations. For the $p = 1000$ nm shallow-etched ADL in Fig. 6.32 (b), modes do not undergo avoided crossing, in compliance with clear single modes in AESWS data and $k = 0$ simulations. In both datasets the modes do not exhibit large excitation strength at the BZ boundary. Note that the avoided crossing of modes of higher order was also described in etched-through ADLs as shown in the introduction to this chapter and in Fig. 6.2. Such avoided crossings seem to be generic features of 2D artificial crystals. These crossings introduce further forbidden frequency gaps, in addition to gaps later on discussed for BZ boundaries (see also Ref. [Tac12b]).

$p = 600$ nm samples

We now discuss data obtained on a set of three samples: $p = 600$ nm BCL, shallow-etched ADL, and a plain film. The Py mesas of all sam-

ples have been prepared in one step, to allow direct comparison. For all three samples $w_{\mathrm{IC}} = 2$ µm CPWs were used with a propagation distance of $d = 12$ µm. In Fig. 6.29 (c) and (d) we show $\Re(a_{12})$ AESWS data acquired on the $p = 600$ nm BCL and shallow-etched ADL. While data obtained on the BCL (Fig. 6.29 (c)) shows no black-white-black contrast, such a contrast is clearly seen in data obtained on the shallow-etched ADL (Fig. 6.29 (d)). This is further illustrated in Fig. 6.33, where we show a_{11} and a_{12} normalized spectra obtained on (a) the BCL and (b) the shallow-etched ADL at a field of $\mu_0 H = 34$ mT, corresponding to µBLS data shown in Fig. 6.27 acquired at 35 mT. The black line is $|a_{11}|$ data and clearly shows two modes for both samples. Red, blue, and green lines are $|a_{12}|$, $\Re(a_{12})$, and $Im(a_{12})$ data, respectively. a_{12} data has a significantly higher signal-to-noise ratio for the BCL sample compared to the shallow-etched ADL. $|a_{12}|$ data acquired on the BCL (Fig. 6.33 (a)) shows the envelope of both resonances. The second resonance is distorted by noise of high frequency-period. $\Re(a_{12})$ and $Im(a_{12})$ data acquired on the BCL show the characteristic curve of a resonance, but no oscillations due to phase-shifts from propagating spin waves. In Fig. 6.33 (b) we show data obtained on the shallow-etched ADL. Here, three modes of high intensity are resolved, the center mode is marked by a black arrow. A further mode is resolved near 8 GHz. We attribute the center mode and the 8 GHz mode to excitations by the second transmitted wavevector $k_{\mathrm{CPW},2}$. These mode are resolved, as well, in Fig. 6.29. We will substantiate this hypothesis in the following when we study $f(k)$ dispersions. In Fig. 6.33 (b) we further find oscillation signals for the three modes of highest intensity. Although $|a_{12}|$ is distorted due to the varying baseline of $\Re(a_{12})$ and $Im(a_{12})$ data as in Fig. 6.30, we can separate oscillations of all three modes and thus extract v_g for each mode. This will be studied in the following, when discussing the dispersion $f(k)$.

We note that oscillations that provide information on v_g as well as modes from the second excited wavevector $k_{\mathrm{CPW},2}$ are resolved in data obtained on the shallow-etched ADL, but **not** the BCL. We further find that $\frac{|a_{21}|}{|a_{11}|}$ is 0.1 for the shallow-etched ADL compared to 0.02 for the BCL. We attribute this to higher damping in the BCL compared to the shallow-etched ADL. We substantiate this by studying linewidths Δf, obtained from $|a_{11}|$ data, as higher damping leads to broader linewidths. In Fig. 6.34 we show

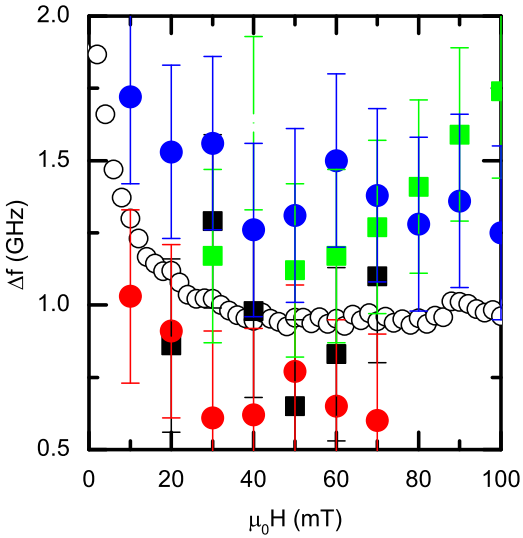

Figure 6.34: Linewidths Δf extracted from $|a_{11}|$ AESWS data. All data acquired using $w_{\mathrm{IC}} = 2$ µm CPWs at $\eta = 0°$. Open circles indicate plain film data. Full squares indicate lower frequency (i), full dots higher frequency (ii) mode data of the $p = 600$ nm shallow-etched ADL (black and red color) and BCL (green and blue color).

linewidths Δf obtained from the FWHM of Lorentz functions fitted to the $|a_{11}|$ AESWS data of the lower and higher mode of the $p = 600$ nm BCL and shallow-etched ADL. Filled squares (circles) stand for the lower (higher) mode, blue and green (black and red) for the BCL (shallow-etched ADL). An error of ± 0.3 GHz is taken into account due to mixing between modes and phase distortions as described in Chapter 3. Both effects lead to distortions of the Lorentz function shape. The respective plain film data obtained from nominally identical Py and CPWs is shown for reference (open circles). Δf of the BCL modes (green squares and blue circles) is consistently higher by several 100 MHz compared to the shallow-etched ADL. Following [Cou04], the damping factor α is connected with the fre-

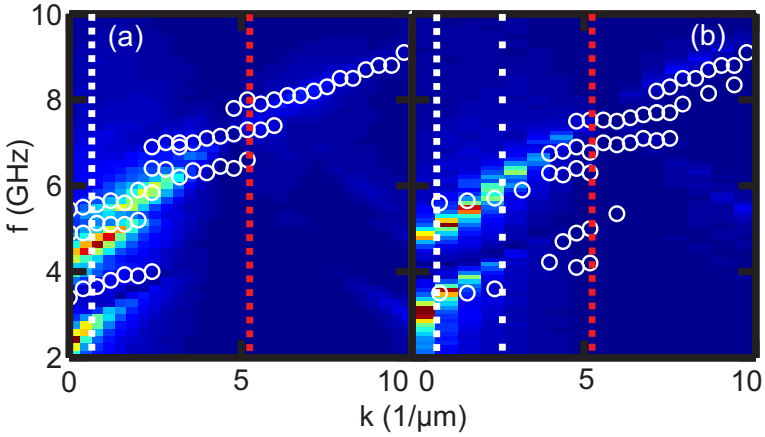

Figure 6.35: Simulated dispersion relation $f(k)$ for $p = 600$ nm (a) BCL and (b) shallow-etched ADL at $\mu_0 H = 20$ mT. White circles indicate experimental BLS data.

quency linewidth Δf by

$$\Delta f \approx 2\pi\alpha\gamma\mu_0 M_{\mathrm{sat}}. \tag{6.1}$$

An increased damping constant α usually found for Co (see Refs. [Ina06, Vla10, San99, Neu11a] cannot explain the observed increased linewidth Δf of the high-frequency BCL mode that shows highest spin-precession amplitudes only in Py.

In the following we rule out inhomogeneous line broadening as a contributing factor to the increased linewidth. Following [Cou04], the frequency linewidth is influenced as follows:

$$\Delta f = v_g \Delta k, \tag{6.2}$$

where Δk is the spectral width of the wave vector. In Fig. 6.35 we show simulated and measured wavevector dispersions $f(k)$ for the $p = 600$ nm (a) BCL and (b) shallow-etched ADL. The color image represents micromagnetic simulations. White circles show conventional BLS data acquired at CNISM in Perugia, Italy by Dr. Madami and Dr. Gubbiotti. Simula-

Sample	Method	v_g lower mode	v_g higher mode
BCL	MicroMagus	3.2 km/s ± 0.5 km/s	3.2 km/s ± 0.5 km/s
ADL	MicroMagus	2.9 km/s ± 0.5 km/s	3.9 km/s ± 0.5 km/s
ADL	AESWS	3.1 km/s	4.4 km/s

Table 6.2: Group velocities v_g extracted from micromagnetic simulations at k_{CPW}.

tion and experimental data show good agreement for both samples. Red dotted lines indicate the 1. BZ boundary and white closely dotted lines indicate the first CPW wavevector $k_{\mathrm{CPW},1}$, the sparsely dotted line indicates the second wavevector $k_{\mathrm{CPW},2}$, motivating the center frequency mode, as introduced above (only resolved in the shallow-etched ADL). From these data we extract v_g by estimating the dispersion's slope $\frac{\partial f(k)}{\partial k} = \frac{v_g}{2\pi}$ at $k = k_{\mathrm{CPW}}$. We take into account an error of ± 0.5 km/s due to the limited resolution of the simulated dispersion.

In Table 6.2 we show the extracted values and compare to experimental data obtained from $\Re(a_{12})$ AESWS data on the $p = 600$ nm shallow-etched ADL 138-A1-1. We find that experimental and simulated data agree well within the error. We find no increased v_g in micromagnetic simulations for the BCL and we rule out inhomogeneous line broadening given by 6.2.

Magnonic band gaps in $p = 600$ nm BCL

We further study the dispersion relation of the BCL shown in Fig. 6.35 (a). As was already shown in Fig. 6.32, the higher frequency mode undergoes avoided crossings. In order to shed light onto these avoided crossings, PWM method calculations have been performed by Dr. J. Kłos and Dr. M. Krawczyk at AMU in Poznan, see chapter 2.4.2. Here the system was modeled with a uniform thickness, consisting of a $t_{\mathrm{eff}} = 20$ nm thick sample of circular Co inclusions in Py. $t_{\mathrm{eff}} = 20$ nm was found to provide best agreement with BLS data using the same material parameters as in micromagnetic simulations. We justify the use of uniform thickness by the low dependence of H_{dem} on the lateral coordinate as described in chapter 6.4.2.

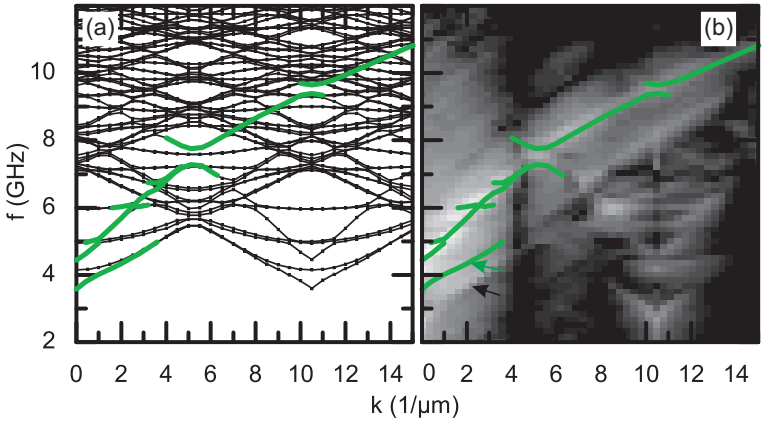

Figure 6.36: (a) Spin-wave dispersion $f(k)$ of a $p = 600$ nm BCL. Black dots indicate results from PWM calculations. Green lines indicate most intense modes. (b) Micromagnetic simulations obtained by MicroMagus simulations are indicated by the grey scale plot. Resonances are white.

In Fig. 6.36, we compare PWM calculation results with micromagnetic simulations already shown in Fig. 6.35 (a). In Fig. 6.36 (a) we find a high number of modes, shown as connected black dots. Thick green lines mark modes with highest cross-section, expected to be modes of highest intensity in BLS measurements. As can be seen in Fig. 6.36 (b) these modes of highest cross-section agree well with the micromagnetic simulation, shown here as gray-scale plot where bright color indicates resonances. We find a frequency difference of up to 1 GHz between PWM (green arrow) and micromagnetic simulations (black arrow) for the low-frequency mode, that we attribute to the assumptions in PWM: sample with homogeneous thickness and without underlayer, and only H_{dem} parallel to H is considered. We find the low-frequency mode extending across the BZ boundary in micromagnetic simulations. In PWM the mode does not contribute with high cross-section and is not resolved in BLS across the BZ boundary (see Fig. 6.35).

In Fig. 6.37 we show the first BZ calculated by the PWM in more detail.

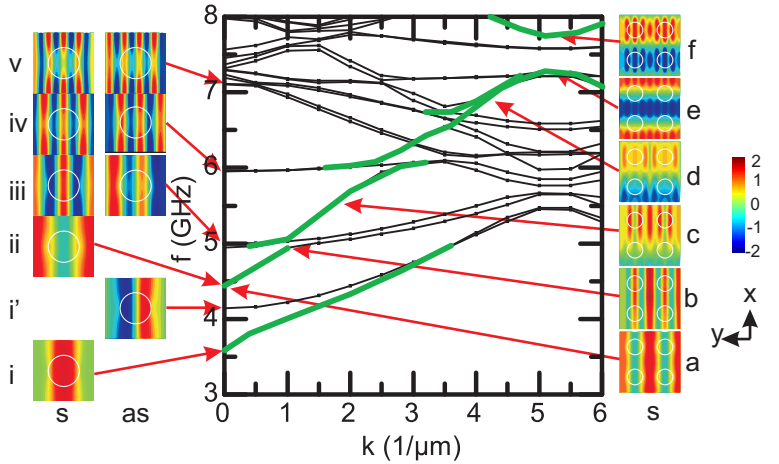

Figure 6.37: Spin-wave dispersion $f(k)$ of a $p = 600$ nm BCL. Black dots indicate results from PWM calculations, green lines indicate most intense modes. Color plots show phase resolved spatial spin-wave profiles extracted at the (f, k) values, where red arrows end. Symmetric (s) and antisymmetric (as) modes are shown.

Further we include mode profiles at specific points. On the left we show spin wave profiles extracted from PWM at $k = 0$. The left (right) column shows symmetric (antisymmetric) modes. Modes i, ii and iii correspond to modes resolved with micromagnetic simulations. Mode i', i.e. the antisymmetric version of mode i is not excited by micromagnetic simulations due to its antisymmetric profile. Modes iii, iv, and v exist in pairs of antisymmetric and symmetric modes. Modes iv and v are not resolved by the micromagnetic simulation and have small amplitude at $k = 0$. While modes i, i', and ii are localized in the channels defined by H_{dem} (see chapter 6.4.2), modes iii to v have significant amplitude throughout the unit cell. Modes with highest cross-section are again marked by a thick green line. We now follow mode ii throughout the first BZ along points a to f, each illustrated by spin precession profiles on the right. Now we show two by two unit cells per picture. Point a is at $k = 0$ and corresponds to ii in the left column. At point b an avoided crossing with the symmetric mode iii takes place, resulting in a hybridization of modes: at point b one more

node arises. The mode crosses with the antisymmetric mode iii. Further avoided crossings take place with symmetric modes iv and v, visible in points c to e. As k increases, the wavelength λ is reduced. At point e, at the first BZ boundary, the wavelength equals the period of the system $\lambda = 2p$. Interestingly PWM predicts a band gap. This is due to Bragg reflection. Maxima of profiles e and f, i.e., at the BZ boundary in the lower and the upper branch of the gap, respectively, are shifted by $p/2$. Mode e is localized mainly in Py for the lower frequency branch and mode f has a significant amplitude in Co for the upper frequency branch. The variation of mode localization between the different materials is expected to govern the width of the band gap, as the resonance frequency f depends on the local internal field H_{int} and M_{sat}. In further PWM calculations it is found that the band gap width is influenced mainly by the Co filling fraction and the difference between saturation magnetizations of the involved materials. This allows tailoring the band gap using different materials than Co and Py in further studies. It is important to note that in $p = 800$ nm ADLs [Ziv12], band gaps were found to be governed only by the demagnetization field caused by the air holes along the propagation path. In our study, H_{dem} does not play a crucial role as the variation is only 20 Oe (as determined from micromagnetic simulations).

In [Neu11c] it was found in experiment, simulation and PWM calculation that in ADLs magnonic minibands exist due to coupling of so-called edge modes. ADLs have been prepared with 120 nm diameter etched-through nanoholes in a quadratic lattice. Surprisingly large spin-wave velocities have been found for the periodicities $p \leq 400$ nm, notably smaller that in our BCL study. Here not the fundamental mode between holes, similar to mode (ii) in Fig. 6.37 was found to propagate, but coupled edge modes, that have highest spin-precession amplitudes at the hole edges. Coherent coupling allowed the formation of a miniband. The band gap was between the edge mode, and the fundamental mode. The miniband width increased for small periods p so that edge modes couple efficiently between holes and the edge mode forms coherently throughout the lattice. The band gap we have found in BCLs, does not depend on such a process and is consequently also found at larger periods $p > 400$ nm.

7 Summary and Outlook

In this thesis we have studied spin waves in 360 nm wide nanowires and bicomponent square lattices with periods of 1 μm and 600 nm fabricated from $Ni_{80}Fe_{20}$ and Co thin films using electron beam lithography. Nanowires and bicomponent lattices have been studied using all-eletrical spin wave spectroscopy (AESWS) and micromagnetic simulations, while bicomponent lattices have also been studied using Brillouin light scattering (BLS) and plane wave method calculations. Quasistatic properties of bicomponent lattices (BCLs) have ben studied by magnetic X-ray transmission microscopy (MTXM).

In nanowires we have found enhanced spin-wave transmission in the so-called zigzag-magnetization configuration. The spin waves are confined to the interior of the nanowires, away from the edges due to a self-cladding effect induced by the inhomogeneous magnetization. Cladding is known from fiber-optics. In our case the effect is field-controlled and reversible. The group velocity is modulated by 25% by a small angle variation of 1.5°. It opens up new possibilities for spin-wave busses and spin-wave nano-optics on the nanometer scale. Future work might improve upon the presented results and provide higher group velocities and higher modulation depths.

For BCLs we have found that local magnetic switching, as observed in magnetic X-ray transmission microscopy, is in part modeled by micromagnetic simulations. Switching occurs in two distinct steps, each exhibiting a unique activity pattern of magnetization change. We have further performed a dynamic study of BCLs in comparison to reference samples, where the second magnetic material has been left out. In a combined AESWS, micro-focused BLS, and micromagnetic simulation study, we have found two stripe-like excitations of spin-waves perpendicular to the external field in both samples. Leaving out the second magnetic materials shifts both excitations by half a spatial period. Frequencies are almost the same in both samples. Nanopatterned samples using filled and empty

samples allow spatial shifting of excitations at a given frequencies. Further work might improve upon the similarity of frequencies and further reduced lattice periods. We have further studied spin wave propagation in BCLs by BLS, micromagnetic simulations, and plane wave method (PWM) calculations. In experiment and calculation, a band gap of 0.6 GHz at the boundary of the first BZ has been found. The width has been explained by Bragg diffraction using PWM as stemming from the material contrast between $Ni_{80}Fe_{20}$ and Co. This is in contrast to earlier magnonic crystals, where the band gap depended on the internal field in the sample. Here we reported on a band structure that might be tuned in a wide regime by the period of the sample and the used materials, allowing unprecedented control over spin waves in magnonic crystals. Future work on BCLs may further use external fields applied in out-of-plane direction to reduce the impact of in-plane demagnetization fields in the sample. In [Sch12] it was possible to create complete stop bands in nano-structured anidot lattices. Out-of-plane fields may also be applied for further studies on BCLs.

List of Figures

Bibliography

[Bai01] M. Bailleul, D. Olligs, C. Fermon and S. O. Demokritov: *Spin waves propagation and confinement in conducting films at the micrometer scale*, Europhys. Lett. **56**, 741 (2001).

[Bai03] M. Bailleul, D. Olligs and C. Fermon: *Micromagnetic Phase Transitions and Spin Wave Excitations in a Ferromagnetic Stripe*, Phys. Rev. Lett. **91**, 137204 (2003).

[Bao08] M. Bao, K. Wong, A. Khitun, J. Lee, Z. Hao, K. L. Wang, D. W. Lee and S. X. Wang: *Determining wave vector and material property from the phase-shift of spin-wave propagation*, Europhys. Lett. **84**, 27009 (2008).

[Bay04] C. Bayer, J. P. Park, H. Wang, M. Yan, C. E. Campbell and P. A. Crowell: *Spin waves in an inhomogeneously magnetized stripe*, Phys. Rev. B **69**, 134401 (2004).

[Bay05] C. Bayer, J. Jorzick, B. Hillebrands, S. O. Demokritov, R. Kouba, R. Bozinoski, A. N. Slavin, K. Y. Guslienko, D. V. Berkov, N. L. Gorn and M. P. Kostylev: *Spin-wave excitations in finite rectangular elements of $Ni_{80}Fe_{20}$*, Phys. Rev. B **72**, 064427 (2005).

[Ber08] D. V. Berkov and N. L. Gorn: *Micromagus - software for micromagnetic simulations*, http://www.micromagus.de (2008).

[Bil07a] C. Bilzer: *Microwave susceptibility of thin ferromagnetic films: metrology and insight into magnetization dynamics*, Ph.D. thesis, Faculté des sciences d'Orsay (2007).

[Bil07b] C. Bilzer, T. Devolder, P. Crozat, C. Chappert, S. Cardoso and P. P. Freitas: *Vector network analyzer ferromagnetic resonance of thin films on coplanar waveguides: Comparison of different evaluation methods*, J. Appl. Phys. **101**, 074505 (2007).

[Blo30] F. Bloch: *Zur Theorie des Ferromagnetismus*, Zeitschrift für Physik **61**, 206 (1930).

[Blu01] S. Blundell: *Magnetism in Condensed Matter*, Oxford University Press, Oxford, 2001.

[Boo09] C. T. Boone, J. A. Katine, J. R. Childress, V. Tiberkevich, A. Slavin, J. Zhu, X. Cheng and I. N. Krivorotov: *Resonant Nonlinear Damping of Quantized Spin Waves in Ferromagnetic Nanowires: A Spin Torque Ferromagnetic Resonance Study*, Phys. Rev. Lett. **103**, 167601 (2009).

[Cho06] S. Choi, K.-S. Lee and S.-K. Kim: *Spin-wave interference*, Appl. Phys. Lett. **89**, 062501 (2006).

[Cho07] S. Choi, K.-S. Lee, K. Y. Guslienko and S.-K. Kim: *Strong Radiation of Spin Waves by Core Reversal of a Magnetic Vortex and Their Wave Behaviors in Magnetic Nanowire Waveguides*, Phys. Rev. Lett. **98**, 087205 (2007).

[Cou04] G. Counil, J.-V. Kim, T. Devolder, C. Chappert, K. Shigeto and Y. Otani: *Spin wave contributions to the high-frequency magnetic response of thin films obtained with inductive methods*, J. Appl. Phys. **95**, 5646 (2004).

[Cov02] M. Covington, T. M. Crawford and G. J. Parker: *Time-Resolved Measurement of Propagating Spin Waves in Ferromagnetic Thin Films*, Phys. Rev. Lett. **89**, 237202 (2002).

[Dam61] R. Damon and J. Eshbach: *Magnetostatic modes of a ferrite slab*, J. Phys. Chem. Solids **19**, 308 (1961).

[Dem01] S. O. Demokritov, B. Hillebrands and A. N. Slavin: *Brillouin light scattering studies of confined spin waves: linear and nonlinear confinement*, Physics Reports **348**, 441 (2001).

[Dem04] S. O. Demokritov, A. A. Serga, A. Andr, V. E. Demidov, M. P. Kostylev, B. Hillebrands and A. N. Slavin: *Tunneling of Dipolar Spin Waves through a Region of Inhomogeneous Magnetic Field*, Phys. Rev. Lett. **93**, 047201 (2004).

[Dem06] S. O. Demokritov, V. E. Demidov, O. Dzyapko, G. A. Melkov, A. A. Serga, B. Hillebrands and A. N. Slavin: *Bose-Einstein condensation of quasi-equilibrium magnons at room temperature under pumping*, Nature **443**, 430 (2006).

[Dem08] V. E. Demidov, S. O. Demokritov, K. Rott, P. Krzysteczko and G. Reiss: *Nano-optics with spin waves at microwave frequencies*, Appl. Phys. Lett. **92**, 232503 (2008).

[Dem10] V. E. Demidov, M. Buchmeier, K. Rott, P. Krzysteczko, J. Münchenberger, G. Reiss and S. O. Demokritov: *Nonlinear Hybridization of the Fundamental Eigenmodes of Microscopic Ferromagnetic Ellipses*, Phys. Rev. Lett. **104**, 217203 (2010).

[Due11] G. Duerr, M. Madami, S. Neusser, S. Tacchi, G. Gubbiotti, G. Carlotti and D. Grundler: *Spatial control of spin-wave modes in $Ni_{80}Fe_{20}$ antidot lattices by embedded Co nanodisks*, Appl. Phys. Lett. **99**, 202502 (2011).

[Due12a] G. Duerr, R. Huber and D. Grundler: *Enhanced functionality in magnonics by domain walls and inhomogeneous spin configurations*, J. Phys. Cond. Mat. **24**, 024218 (2012).

[Due12b] G. Duerr, K. Thurner, J. Topp, R. Huber and D. Grundler: *Enhanced Transmission through Squeezed Modes in a Self-Cladding Magnonic Waveguide*, Phys. Rev. Lett. **108**, 227202 (2012).

[Erc97] A. Ercole, A. O. Adeyeye, C. Daboo, J. A. C. Bland and D. G. Hasko: *Finite size effects in the static and dynamic magnetic properties of FeNi wire array structures*, J. Appl. Phys. **81**, 5452 (1997).

[Fis96] P. Fischer, G. Schütz, G. Schmahl, P. Guttmann and D. Raasch: *Imaging of magnetic domains with the X-ray microscope at BESSY using X-ray magnetic circular dichroism*, Zeitschrift für Physik B Condensed Matter **101**, 313 (1996).

[Fis98] P. Fischer, T. Eimüller, G. Schütz, P. Guttmann, G. Schmahl, K. Pruegl and G. Bayreuther: *Imaging of magnetic domains by transmission x-ray microscopy*, Journal of Physics D: Applied Physics **31**, 649 (1998).

[Fis07] P. Fischer, D.-H. Kim, B. Mesler, W. Chao and E. Anderson: *Magnetic soft X-ray microscopy: Imaging spin dynamics at the nanoscale*, J. Mag. Mag. Mat. **310**, 2689 (2007).

[Gie05a] F. Giesen: *Magnetization dynamics of nanostructured ferromagnetic rings and rectangular elements*, Ph.D. thesis, Universität Hamburg, Fachbereich Physik (2005).

[Gie05b] F. Giesen, J. Podbielski, T. Korn, M. Steiner, A. van Staa and D. Grundler: *Hysteresis and control of ferromagnetic resonances in rings*, Appl. Phys. Lett. **86**, 112510 (2005).

[Gil55] T. Gilbert: *A Lagrangian Formulation of the Gyromagnetic Equation of the Magnetization Field*, Phys. Rev. **100**, 1243 (1955).

[Gub02] G. Gubbiotti, G. Carlotti, F. Nizzoli, R. Zivieri, T. Okuno and T. Shinjo: *Magnetic properties of submicron circular permalloy dots*, IEEE Trans. Mag. **38**, 2532 (2002).

[Gub09] G. Gubbiotti, G. Carlotti, M. Madami, S. Tacchi, P. Vavassori and G. Socino: *Setup of a new Brillouin light scattering apparatus with submicrometric lateral resolution and its application to the study of spin modes in nanomagnets*, J. Appl. Phys. **105**, 07D521 (2009).

[Gur96] A. Gurevich and G. Melkov: *Magnetization oscillations and waves*, CRC Press, Boca Raton, 1996.

[Gus02] K. Y. Guslienko, S. O. Demokritov, B. Hillebrands and A. N. Slavin: *Effective dipolar boundary conditions for dynamic magnetization in thin magnetic stripes*, Phys. Rev. B **66**, 132402 (2002).

[Her04] R. Hertel, W. Wulfhekel and J. Kirschner: *Domain-Wall Induced Phase Shifts in Spin Waves*, Phys. Rev. Lett. **93**, 257202 (2004).

[Hey07] L. Heyderman, S. Czekaj, F. Nolting, D.-H. Kim and P. Fischer: *Cobalt antidot arrays on membranes: Fabrication and investigation with transmission X-ray microscopy*, J. Mag. Mag. Mat. **316**, 99 (2007).

[Hil02] B. Hillebrands and K. Ounadjela: *Spin Dynamics in Confined Magnetic Structures*, Springer, Berlin, 2002.

[Im03] M.-Y. Im, P. Fischer, T. Eimuller, G. Denbeaux and S.-C. Shin: *Magnetization reversal study of CoCrPt alloy thin films on a nanogranular-length scale using magnetic transmission soft x-ray microscopy*, Appl. Phys. Lett. **83**, 4589 (2003).

[Ina06] N. Inaba, H. Asanuma, S. Igarashi, S. Mori, F. Kirino, K. Koike and H. Morita: *Damping Constants of Ni-Fe and Ni-Co Alloy Thin Films*, Magnetics, IEEE Transactions on **42**, 2372 (2006).

[Joa97] J. Joannopoulos, P. Villeneuve and S. Fan: *Photonic Crystals*, Sol. Stat. Comm. **102**, 165 (1997).

[Jor99] J. Jorzick, S. O. Demokritov, C. Mathieu, B. Hillebrands, B. Bartenlian, C. Chappert, F. Rousseaux and A. N. Slavin: *Brillouin light scattering from quantized spin waves in micron-size magnetic wires*, Phys. Rev. B **60**, 15194 (1999).

[Jor02] J. Jorzick, S. O. Demokritov, B. Hillebrands, M. Bailleul, C. Fermon, K. Y. Guslienko, A. N. Slavin, D. V. Berkov and N. L. Gorn: *Spin Wave Wells in Nonellipsoidal Micrometer Size Magnetic Elements*, Phys. Rev. Lett. **88**, 047204 (2002).

[Kac74] J. Kaczer and L. Murtinova: *On the demagnetizing energy of periodic magnetic distributions*, phys. stat. sol. (a) **23**, 79 (1974).

[Kal86] B. Kalinikos and A. Slavin: *Theory of dipole-exchange spin wave spectrum for ferromagnetic films with mixed exchange boundary conditions*, J. Phys. C **19**, 7013 (1986).

[Kal06] S. S. Kalarickal, P. Krivosik, M. Wu, C. E. Patton, M. L. Schneider, P. Kabos, T. J. Silva and J. P. Nibarger: *Ferromagnetic resonance linewidth in metallic thin films: Comparison of measurement methods*, J. Appl. Phys. **99**, 093909 (2006).

[Kam75] V. Kambersky and C. E. Patton: *Spin-wave relaxation and phenomenological damping in ferromagnetic resonance*, Phys. Rev. B **11**, 2668 (1975).

[Kao09] Kao: *SAND FROM CENTURIES PAST: SEND FUTURE VOICES FAST*, Nobel Prize Lecture (2009).

[Kas08] S. Kasai, P. Fischer, M.-Y. Im, K. Yamada, Y. Nakatani, K. Kobayashi, H. Kohno and T. Ono: *Probing the Spin Polarization of Current by Soft X-Ray Imaging of Current-Induced Magnetic Vortex Dynamics*, Phys. Rev. Lett. **101**, 237203 (2008).

[Ken07] K. J. Kennewell, M. Kostylev and R. L. Stamps: *Calculation of spin wave mode response induced by a coplanar microwave line*, J. Appl. Phys. **101**, 09D107 (2007).

[Khi02] A. G. Khitun, R. Ostroumov and K. L. Wang: *Feasibility study of the spin wave quantum network*, Proc. SPIE **5023**, 449 (2002).

[Khi07] A. Khitun, D. E. Nikonov, M. Bao, K. Galatsis and K. L. Wang: *Feasibility study of logic circuits with a spin wave bus*, Nanotech. **18**, 465202 (2007).

[Khi08a] A. Khitun, M. Bao, J. Lee, K. Wang, D. Lee, S. Wang and I. Roshchin: *Inductively Coupled Circuits with Spin Wave Bus for Information Processing*, J. Nanoelectr. Optoelctr. **3**, 24 (2008).

[Khi08b] A. Khitun, M. Bao, Y. Wu, J.-Y. Kim, A. Hong, A. Jacob, K. Galatsis and K. L. Wang: *Spin Wave Logic Circuit on Silicon Platform*, IEEE Comp. Soc. , 1107 (2008).

[Khi10] A. Khitun, M. Bao and K. L. Wang: *Magnonic logic circuits*, J. Phys. D **43**, 264005 (2010).

[Kim06] D.-H. Kim, P. Fischer, W. Chao, E. Anderson, M.-Y. Im, S.-C. Shin and S.-B. Choe: *Magnetic soft x-ray microscopy at 15 nm resolution probing nanoscale local magnetic hysteresis (invited)*, J. Appl. Phys. **99**, 08H303 (2006).

[Kit68] C. Kittel: *Einfhrung in die Festkörperphysik*, R. Oldenburg, 1968.

[Klo12] J. W. Klos, M. L. Sokolovskyy, S. Mamica and M. Krawczyk: *The impact of the lattice symmetry and the inclusion shape on the spectrum of 2D magnonic crystals*, J. Appl. Phys. **111**, 123910 (2012).

[Kos07] M. P. Kostylev, G. Gubbiotti, J.-G. Hu, G. Carlotti, T. Ono and R. L. Stamps: *Dipole-exchange propagating spin-wave modes in metallic ferromagnetic stripes*, Phys. Rev. B **76**, 054422 (2007).

[Koz09] A. Kozhanov, D. Ouellette, Z. Griffith, M. Rodwell, A. P. Jacob, D. W. Lee, S. X. Wang and S. J. Allen: *Dispersion in magnetostatic CoTaZr spin waveguides*, Appl. Phys. Lett. **94**, 012505 (2009).

[Kra08] M. Krawczyk and H. Puszkarski: *Plane-wave theory of three-dimensional magnonic crystals*, Phys. Rev. B **77**, 054437 (2008).

[Kru06] V. Kruglyak and R. Hicken: *Magnonics: Experiment to prove the concept*, J. Mag. Mag. Mat. **306**, 191 (2006).

[Kru10] V. V. Kruglyak, S. O. Demokritov and D. Grundler: *Magnonics*, J. Phys. D **43**, 264001 (2010).

[Kua05] B. Kuanr, R. E. Camley and Z. Celinski: *Narrowing of the frequency-linewidth in structured magnetic strips: Experiment and theory*, Appl. Phys. Lett. **87**, 012502 (2005).

[Lan35] L. D. Landau and E. M. Lifshitz: *Theory of the dispersion of magnetic permeability in ferromagnetic bodies*, Phys. Z. Sowjetunion **8**, 153 (1935).

[LB11] R. Lassalle-Balier and C. Fermon: *Spin wave propagation in ferromagnetic wires with an arbitrary field direction*, Journal of Physics: Conference Series **303**, 012008 (2011).

[Lee08] K.-S. Lee and S.-K. Kim: *Conceptual design of spin wave logic gates based on a Mach–Zehnder-type spin wave interferometer for universal logic functions*, J. Appl. Phys. **104**, 053909 (2008).

[Len11] B. Lenk, H. Ulrichs, F. Garbs and M. Münzenberg: *The building blocks of magnonics*, Physics Reports **507**, 107 (2011).

[Liu07] Y. Liu, S. Gliga, R. Hertel and C. M. Schneider: *Current-induced magnetic vortex core switching in a Permalloy nanodisk*, Appl. Phys. Lett. **91**, 112501 (2007).

[Ma11] F. S. Ma, H. S. Lim, Z. K. Wang, S. N. Piramanayagam, S. C. Ng and M. H. Kuok: *Micromagnetic study of spin wave propagation in bicomponent magnonic crystal waveguides*, Appl. Phys. Lett. **98**, 153107 (2011).

[Mad11] M. Madami, S. Bonetti, G. Consolo, S. Tacchi, G. Carlotti, G. Gubbiotti, F. B. Mancoff, M. A. Yar and J. kerman: *Direct observation of a propagating spin wave induced by spin-transfer torque*, Nature Nanotechnology **6**, 635638 (2011).

[Mal87] J. Mallinson: *On damped gyromagnetic precession*, Magnetics, IEEE Transactions on **23**, 2003 (1987).

[Mam12] S. Mamica, M. Krawczyk and J. Klos: *Spin-Wave Band Structure in 2D Magnonic Crystals with Elliptically Shaped Scattering Centres*, Adv. Cond. Matt. Phys. **2012**, 163187 (2012).

[Mei07] G. Meier, M. Bolte, R. Eiselt, B. Krüger, D.-H. Kim and P. Fischer: *Direct Imaging of Stochastic Domain-Wall Motion Driven by Nanosecond Current Pulses*, Phys. Rev. Lett. **98**, 187202 (2007).

[Mel01] G. A. Melkov, Y. V. Kobljanskyj, A. A. Serga, V. S. Tiberkevich and A. N. Slavin: *Reversal of Momentum Relaxation*, Phys. Rev. Lett. **86**, 4918 (2001).

[Neu06a] I. Neudecker, M. Kläui, K. Perzlmaier, D. Backes, L. J. Heyderman, C. A. F. Vaz, J. A. C. Bland, U. Rüdiger and C. H. Back: *Spatially Resolved Dynamic Eigenmode Spectrum of Co Rings*, Phys. Rev. Lett. **96**, 057207 (2006).

[Neu06b] I. Neudecker, K. Perzlmaier, F. Hoffmann, G. Woltersdorf, M. Buess, D. Weiss and C. H. Back: *Modal spectrum of permalloy disks excited by in-plane magnetic fields*, Phys. Rev. B **73**, 134426 (2006).

[Neu08] S. Neusser, B. Botters and D. Grundler: *Spin wave modes in antidot lattices: Localization, confinement, and field-controlled propagation*, Phys. Rev. B **78**, 087825 (2008).

[Neu09] S. Neusser and D. Grundler: *Magnonics: Spin Waves on the Nanoscale*, Adv. Mat. **21**, 2927 (2009).

[Neu10] S. Neusser, G. Duerr, H. G. Bauer, S. Tacchi, M. Madami, G. Woltersdorf, G. Gubbiotti, C. H. Back and D. Grundler: *Anisotropic Propagation and Damping of Spin Waves in a Nanopatterned Antidot Lattice*, Phys. Rev. Lett. **105**, 067208 (2010).

[Neu11a] S. Neusser: *Spin Waves in Antidot Lattices: From Quantization to Magnonic Crystals*, Ph.D. thesis, Technische Universität München (2011).

[Neu11b] S. Neusser, H. G. Bauer, G. Duerr, R. Huber, S. Mamica, G. Woltersdorf, M. Krawczyk, C. H. Back and D. Grundler: *Tunable metamaterial response of a $Ni_{80}Fe_{20}$ antidot lattice for spin waves*, Phys. Rev. B **84**, 184411 (2011).

[Neu11c] S. Neusser, G. Duerr, S. Tacchi, M. Madami, M. L. Sokolovskyy, G. Gubbiotti, M. Krawczyk and D. Grundler: *Magnonic minibands in antidot lattices with large spin-wave propagation velocities*, Phys. Rev. B **84**, 094454 (2011).

[Ngu11] H. T. Nguyen, A. Akbari-Sharbaf and M. G. Cottam: *Spin-wave damping in ferromagnetic stripes with inhomogeneous magnetization*, Phys. Rev. B **83**, 214423 (2011).

[Pir11] P. Pirro, T. Brächer, K. Vogt, B. Obry, H. Schultheiss, B. Leven and B. Hillebrands: *Interference of coherent spin waves in micron-sized ferromagnetic waveguides*, physica status solidi (b) **248**, 2404 (2011).

[Pon97] G. E. Ponchak, E. M. Tentzeris and L. P. B. Katehi: *Characterization of finite ground coplanar waveguide with narrow ground planes*, International Journal of Microcircuits and Electronic Packaging **20**, 167 (1997).

[Pon98] G. E. Ponchak, E. M. Tentzeris and L. P. B. Katehi: *Finite ground coplanar (FGC) waveguide: It's characteristics and advantages for use in RF and wireless communication circuits*, 3rd International Wireless Communications Conference (WCC 98) , 75 (1998).

[Roy10] P. E. Roy, T. Trypiniotis and C. H. W. Barnes: *Micromagnetic simulations of spin-wave normal modes and the resonant field-driven magnetization dynamics of a* 360° *domain wall in a soft magnetic stripe*, Phys. Rev. B **82**, 134411 (2010).

[Sak82] H. Sakaki: *Velocity-Modulation Transistor (VMT) —A New Field-Effect Transistor Concept*, Japanese J. Appl. Phys. **21**, L381 (1982).

[San99] G. M. Sandler, H. N. Bertram, T. J. Silva and T. M. Crawford: *Determination of the magnetic damping constant in NiFe films*, J. Appl. Phys. **85**, 5080 (1999).

[Sch87] G. Schuetz, W. Wagner, W. Wilhelm, P. Kienle, R. Zeller, R. Frahm and G. Materlik: *Absorption of circularly polarized x rays in iron*, Phys. Rev. Lett. **58**, 737 (1987).

[Sch12] T. Schwarze, R. Huber, G. Duerr and D. Grundler: *Complete band gaps for magnetostatic forward volume waves in a two-dimensional magnonic crystal*, Phys. Rev. B **85**, 134448 (2012).

[Sek10] K. Sekiguchi, K. Yamada, S. M. Seo, K. J. Lee, D. Chiba, K. Kobayashi and T. Ono: *Nonreciprocal emission of spin-wave packet in FeNi film*, Appl. Phys. Lett. **97**, 022508 (2010).

[Sil99] T. J. Silva, C. S. Lee, T. M. Crawford and C. T. Rogers: *Inductive measurement of ultrafast magnetization dynamics in thin-film Permalloy*, J. Appl. Phys. **85**, 7849 (1999).

[Sko08] R. Skomski: *Simple Models of Magnetism*, Oxford University Press, Oxford, 2008.

[Tac10a] S. Tacchi, M. Madami, G. Gubbiotti, G. Carlotti, A. Adeyeye, S. Neusser, B. Botters and D. Grundler: *Magnetic Normal Modes in Squared Antidot Array With Circular Holes: A Combined Brillouin Light Scattering and Broadband Ferromagnetic Resonance Study*, IEEE Trans. Mag. **46**, 172 (2010).

[Tac10b] S. Tacchi, M. Madami, G. Gubbiotti, G. Carlotti, A. O. Adeyeye, S. Neusser, B. Botters and D. Grundler: *Angular Dependence of Magnetic Normal Modes in NiFe Antidot Lattices With Different Lattice Symmetry*, IEEE Trans. Mag. **46**, 1440 (2010).

[Tac12a] S. Tacchi, B. Botters, M. Madami, J. W. Kłos, M. L. Sokolovskyy, M. Krawczyk, G. Gubbiotti, G. Carlotti, A. O. Adeyeye, S. Neusser and D. Grundler: *Mode conversion from quantized to propagating spin waves in a rhombic antidot lattice supporting spin wave nanochannels*, Phys. Rev. B **86**, 014417 (2012).

[Tac12b] S. Tacchi, G. Duerr, J. Klos, M. Madami, S. Neusser, G. Gubbiotti, G. Carlotti, M. Krawczyk, and D. Grundler: *Forbidden band gaps in the spin-wave spectrum of a two-dimensional bicomponent magnonic crystal*, submitted (2012).

[Top08] J. Topp, J. Podbielski, D. Heitmann and D. Grundler: *Internal spin-wave confinement in magnetic nanowires due to zig-zag shaped magnetization*, Phys. Rev. B **78**, 024431 (2008).

[Top09] J. Topp, D. Heitmann and D. Grundler: *Interaction effects on microwave-assisted switching of $Ni_{80}Fe_{20}$ nanowires in densely packed arrays*, Phys. Rev. B **80**, 174421 (2009).

[Tor98] L. Torres, L. Lopez-Diaz and J. I. niguez: *Micromagnetic tailoring of periodic antidot permalloy arrays for high density storage*, Appl. Phys. Lett. **73**, 3766 (1998).

[Tse09] D. H. Y. Tse, S. J. Steinmuller, T. Trypiniotis, D. Anderson, G. A. C. Jones, J. A. C. Bland and C. H. W. Barnes: *Static and dynamic magnetic properties of $Ni_{80}Fe_{20}$ square antidot arrays*, Phys. Rev. B **79**, 054426 (2009).

[Ulr10] H. Ulrichs, B. Lenk and M. Munzenberg: *Magnonic spin-wave modes in CoFeB antidot lattices*, Appl. Phys. Lett. **97**, 092506 (2010).

[Vas96] J. O. Vasseur, L. Dobrzynski, B. Djafari-Rouhani and H. Puszkarski: *Magnon band structure of periodic composites*, Phys. Rev. B **54**, 1043 (1996).

[Vla08] V. Vlaminck and M. Bailleul: *Current-Induced Spin-Wave Doppler Shift*, Science **322**, 410 (2008).

[Vla10] V. Vlaminck and M. Bailleul: *Spin-wave transduction at the submicrometer scale: Experiment and modeling*, Phys. Rev. B **81**, 014425 (2010).

[Vog09] K. Vogt, H. Schultheiss, S. J. Hermsdoerfer, P. Pirro, A. A. Serga and B. Hillebrands: *All-optical detection of phase fronts of propagating spin waves in a $Ni_{81}Fe_{19}$ microstripe*, Appl. Phys. Lett. **95**, 182508 (2009).

[Vys05] S. L. Vysotski, S. A. Nikitov and Y. A. Filimonov: *Magnetostatic Spin Waves in Two-Dimensional Periodic Structures (Magnetophoton Crystals)*, J. Exp. Theor. Phys. **101**, 547 (2005).

[Wan02] Z. K. Wang, M. H. Kuok, S. C. Ng, D. J. Lockwood, M. G. Cottam, K. Nielsch, R. B. Wehrspohn and U. Gsele: *Spin-Wave Quantization in Ferromagnetic Nickel Nanowires*, Phys. Rev. Lett. **89**, 027201 (2002).

[Wan10] Z. K. Wang, V. L. Zhang, H. S. Lim, S. C. Ng, M. H. Kuok, S. Jain and A. O. Adeyeye: *Nanostructured Magnonic Crystals with Size-Tunable Bandgaps*, ACS Nano **4**, 643 (2010).

[Wen69] C. Wen: *Coplanar Waveguide: A Surface Strip Transmission Line Suitable for Nonreciprocal Gyromagnetic Device Applications*, IEEE Trans. Microw. Theo. Techn. **17**, 1087 (1969).

[Yu03] C. Yu, M. J. Pechan and G. J. Mankey: *Dipolar induced, spatially localized resonance in magnetic antidot arrays*, Appl. Phys. Lett. **83**, 3948 (2003).

[Yu04] C. Yu, M. J. Pechan, W. A. Burgei and G. J. Mankey: *Lateral standing spin waves in permalloy antidot arrays*, J. Appl. Phys. **95**, 6648 (2004).

[Zha11] V. L. Zhang, H. S. Lim, C. S. Lin, Z. K. Wang, S. C. Ng, M. H. Kuok, S. Jain, A. O. Adeyeye and M. G. Cottam: *Ferromagnetic and antiferromagnetic spin-wave dispersions in a dipole-exchange coupled bicomponent magnonic crystal*, Appl. Phys. Lett. **99**, 143118 (2011).

[Ziv12] R. Zivieri, S. Tacchi, F. Montoncello, L. Giovannini, F. Nizzoli, M. Madami, G. Gubbiotti, G. Carlotti, S. Neusser, G. Duerr and D. Grundler: *Bragg diffraction of spin waves from a two-dimensional antidot lattice*, Phys. Rev. B **85**, 012403 (2012).

Publications

- S. Neusser, G. Duerr, H.G. Bauer, S. Tacchi, M. Madami, G. Woltersdorf, G. Gubbiotti, C.H. Back, and D. Grundler: Anisotropic propagation and damping of spin waves in a nanopatterned antidot lattice, Phys. Rev. Lett. 105, 067208 (2010)
- S. Neusser, G. Duerr, S. Tacchi, M. Madami, M.L. Sokolovskyy, G. Gubbiotti, M. Krawczyk, and D. Grundler: Magnonic minibands in antidot lattices with large spin-wave propagation velocities, Phys. Rev. B. 84, 094454 (2011)
- T. Schwarze, R. Huber, G. Duerr, F. Brandl, S. Neusser, K. Thurner, and D. Grundler: Microwave Antennas for Broadband Spectroscopy on Magnonic Metamaterials, in: Metamaterials '2011: The Fifth International Congress on Advanced Electromagnetic Materials in Microwaves and Optics, Metamorphose-VI, ISBN 978-952-67611-0-7, p. 576 (2011)
- G. Duerr, M. Madami, S. Neusser, S. Tacchi, G. Gubbiotti, G. Carlotti, and D. Grundler: Spatial control of spin-wave modes in Ni80Fe20 antidot lattices by embedded Co nanodisks, Appl. Phys. Lett. 99, 202502 (2011)
- S. Neusser, H.G. Bauer, G. Duerr, R. Huber, S. Mamica, G. Woltersdorf, M. Krawczyk, C.H. Back, and D. Grundler: Tunable metamaterial response of a Ni80Fe20 antidot lattice for spin waves, Phys. Rev. B 84, 184411 (2011)
- R. Zivieri, S. Tacchi, F. Montoncello, L. Giovannini, F. Nizzoli, M. Madami, G. Gubbiotti, G. Carlotti, S. Neusser, G. Duerr, and D. Grundler: Bragg diffraction of spin waves from a two-dimensional antidot lattice, Phys. Rev. B 85, 012403 (2012)
- T. Schwarze, R. Huber, G. Duerr, and D. Grundler: Complete band gaps for magnetostatic forward volume waves in a two-dimensional magnonic crystal, Phys. Rev. B 85, 134448 (2012)
- G. Duerr, K. Thurner, J. Topp, R. Huber, and D. Grundler: Enhanced transmission through squeezed modes in a self-cladding magnonic waveguide, Phys. Rev. Lett. 108, 227202 (2012)
- H. Yu, R. Huber, T. Schwarze, F. Brandl, T. Rapp, P. Berberich, G. Duerr, and D. Grundler: High propagating velocity of spin waves and temperature

dependent damping in a CoFeB thin film, Appl. Phys. Lett. 100, 262412 (2012)

- S. Tacchi, G. Duerr, J.W. Klos, M. Madami, S. Neusser, G. Gubbiotti, G. Carlotti, M. Krawczyk, and D. Grundler: Forbidden band gaps in the spin-wave spectrum of a two-dimensional bicomponent magnonic crystal, Phys. Rev. Lett. (accepted)
- L. Fallarino, M. Madami, G. Duerr, D. Grundler, G. Gubbiotti, S. Tacchi, and G. Carlotti: Spatial profile of propagating spin waves excited by a finite-ground coplanar waveguide, (submitted)
- E.K. Semenova, F. Montoncello, S. Tacchi, G. Duerr, E. Sirotkin, E. Ahmad, M. Madami, G. Gubbiotti, S. Neusser, D. Grundler, F.Y. Ogrin, R.J. Hicken, V.V. Kruglyak, D.V. Berkov, and N.L. Gorn: Magneto-dynamical response of close packed arrays of circular dots fabricated by nano-sphere lithography, Phys. Rev. B. (submitted)

Review Papers

- S. Neusser, G. Duerr, F. Brandl, R. Huber, T. Schwarze, and D. Grundler: Transmission of GHz spin waves through periodically nanopatterned ferromagnets, in: Metamaterials '2011: The Fifth International Congress on Advanced Electromagnetic Materials in Microwaves and Optics, Metamorphose-VI, ISBN 978-952-67611-0-7, p. 922 (2011)
- J. Topp, G. Duerr, K. Thurner, and D. Grundler: Reprogrammable magnonic crystals formed by interacting ferromagnetic nanowires, Pure Appl. Chem. 83, 1989 (2011)
- G. Duerr, R. Huber, and D. Grundler: Enhanced functionality in magnonics by domain walls and inhomogeneous spin configurations, J. Phys.: Cond. Matter 24, 024218 (2012)
- S. Neusser, G. Duerr, R. Huber, and D. Grundler: Artificial crystals and metamaterials for spin waves from nanopatterned Ni80Fe20 antidot lattices, Chapter 14 (pp. 191 - 203) in Topics in Applied Physics: Magnonics, S.O. Demokritov, A.N. Slavin (Eds), Springer (2013)

Acknowledgements

I would like to express gratitude to all people who contributed to this work. In particular:

- Prof. Dr. Martin Zacharias for supervision of the PhD examination, Prof. Dr. Dirk Grundler for being the first examiner, Prof. Dr. Alexander Holleitner for being the second examiner.
- Prof. Dr. Dirk Grundler for supervision of my thesis, in-depth discussions of all aspects of it, inspiration, and for providing opportunities that far surpassed my expectations.
- Klaus Thurner for fabrication of nanowires and measurements.
- Dr. Jesco Topp for the very fruitful collaboration on nanowires.
- Thomas Schwarze for joint preparation on membranes and joint measurements at the XM-1, ALD deposition, and CoFeB deposition.
- Bernhard Botters and Sebastian Neusser for the ground-breaking work on spin dynamics and lithography at E10. Florian Brandl, Florian Heimbach, Rupert Huber, Thomas Schwarze, Klaus Thurner, and Haiming Yu for the very fruitful collaboration at E10.
- Dr. Gianluca Gubbiotti, Dr. Silvia Tacchi, and Dr. Marco Madami at CNISM Perugia for BLS measurements and frequent discussion.
- Dr. Maciej Krawczyk, Dr. Jarosław Kłos, and Michał Mruczkiewicz at AMU Poznań for PWM calculation and frequent discussion.
- Dr. Volodymyr Kruglyak, Dr. Yat-Yin Au, and Toby Davison at the University of Exeter for TRSKM measurements.
- Mykola Dvornik, now at the University of Ghent for providing his ALS image processing software.
- Dr. Roberto Zivieri for performing dynamical matrix method calculations.
- Dr. Dmitri Berkov at Innovent for support on MicroMagus.
- Prof. Dr. Sergei Nikitov, Dr. Yuri Filimonov, Dr. Yuri Khivintsev, Dr. Sergei Vysotsky, Dr. Aleksandr Kozhevnikov, and Valentin Sakharov at the Kotel'nikov Institute of Radio Engineering and Electronics of RAS in Moscow and Saratov for scientific collaboration and tremendous support in Russia.

- Prof. Alexander Holleitner and Peter Weiser at the Walter Schottky Institut, Center for Nanotechnology and Nanomaterials for providing access to nanolithography facilities and respective support and maintenance. Claudia Paulus for operating the laser writer.
- Dr. Peter Fischer and Dr. Mi-Young Im at the Advanced Light Source at the Lawrence Berkeley National Laboratory for access to and support at the XM-1.
- Prof. Dr. Christian Back, Dr. Georg Woltersdorf, and Hans Günther Bauer at the University of Regensburg for scientific exchange and MOKE measurements.
- Igor Barsukov at the University Duisburg-Essen for providing Fe_3Si samples.
- Dr. Markus Becherer at the Chair of Technical Electronics for frequent discussions and providing samples.
- Thomas Rapp, Paul Berberich, and Thomas Neukel for frequent and immediate technical support.
- Roswitha Hoppen and Claudine Voelcker for organizational support.
- All coworkers at E10 for collaboration and an enjoyable atmosphere: Stephan Albert, Matthias Brasse, Stefanos Chalkidis, Ayman Ibrahim, Stephan Lichtenauer, Amadeus Mlynarski, Benedikt Rupprecht, Johannes Seitz, Marc Wilde, and Tjark Windisch.
- Needless to say, friends and familiy have contributed to the existence of this work by having provided emotional support.

The research leading to these results has received funding from the European Community's Seventh Framework Programme (FP7/2007-2013) under Grant No. 228673 (MAGNONICS), Grant No. 247556 (NoWaPhen), and the German Excellence Cluster Nanosystems Initiative Munich (NIM) and was supported by the Director, Office of Science, Office of Basic Energy Sciences, Materials Sciences and Engineering Division of the U.S. Department of Energy. The support is gratefully acknowledged.